

Structure and dynamics of Yukawa balls

Dissertation
zur Erlangung des Doktorgrades
der Mathematisch-Naturwissenschaftlichen Fakultät
der Christian-Albrechts-Universität zu Kiel

vorgelegt von
Henning Baumgartner

Kiel
Juni 2009

Referent: Prof. Dr. M. Bonitz

Koreferent:

Tag der mündlichen Prüfung:

Zum Druck genehmigt: Kiel, den

Der Dekan

For my beloved family and friends

Contents

Abstract	1
1. Motivation	3
1.1. Strongly coupled plasmas	4
1.2. Outline of this thesis	6
2. Introduction	7
2.1. Experiment	7
2.2. Simulation techniques	12
2.2.1. Molecular dynamics	12
2.2.2. Monte Carlo	13
3. Yukawa balls	21
3.1. Model	21
3.2. Structural properties	24
3.2.1. Ground states	25
3.2.2. Comparison with experiments	28
3.2.3. Ground states of strongly screened mesoscopic Yukawa balls	32
3.2.4. Improved models	45
3.2.5. Potential barriers	50
3.3. Thermodynamic properties	55
3.3.1. Melting parameter	56
3.3.2. Phase diagram	66
3.4. Results in relation to experiments and theory	70
3.4.1. Structural transitions	70
3.4.2. Probability of occurrence of stationary states	71
4. Yukawa tubes	75
4.1. Ewald summation	75
4.2. Structural properties	79
4.2.1. Unit cell definition	81
4.2.2. Ground states	82
4.3. Other anisotropic systems	99
5. Discussion	101
5.1. Summary	101
5.2. Outlook	103

Appendix A. Ground states of Yukawa balls	I
A.1. Structural transition points and anomalies of the first kind . . .	I
A.2. Anomalies of the second kind	III
A.3. Anomalies of the third kind	IV
Appendix B. Phase transition points of Yukawa balls	V
B.1. Melting temperatures I	V
B.2. Melting temperatures II	VII
Appendix C. Ground states of Yukawa tubes	XI
C.1. Structural transitions	XI
Contributions	XV
Bibliography	XIX
Acknowledgment	XXIX
Affidavit	XXXI
Curriculum Vitae	XXXIII

Abstract

In this thesis an overview of structural and thermodynamic properties of finite spherical complex plasma crystals - so-called Yukawa balls - is given. These novel kinds of Wigner crystals can be directly analyzed experimentally with digital video cameras. The experiments clearly reveal a shell structure and allow to determine the shell populations, to observe metastable states and transitions between configurations as well as phase transitions. The experimental observations of the static properties are well explained by a rather simple theoretical model which treats the dust particles as being confined by a parabolic potential and interacting via an isotropic Yukawa pair potential. Within this model, extensive molecular dynamics and Monte Carlo simulations were performed in order to investigate the configurations of the ground state and excited states as well as the melting behavior.

The ground state configurations of the Yukawa balls are known to be sensitive to the screening strength; with increased screening it is observed that the shell populations of the inner shells increase. Here, the focus lies on small Yukawa balls, $N \leq 60$, which not only show this general trend, but also three types of anomalous behavior with the increase of screening at fixed N or for an increase of N at fixed screening. It will be shown, that this exceptional behavior is connected to the special symmetry of the according configurations. These small size effects affect also the behavior of the phase transition from liquid-like to solid-like. The according melting temperatures for mesoscopic systems are being determined by different melting parameter and compared against each other. The results show that finite temperature effects in general do not influence the stability of mesoscopic Yukawa balls in the experiment, although for some given particle numbers radial transitions can even be expected in the experiment.

As a second possible arrangement of the dust particles in the plasma a system is investigated, that confines the particles only radially by a parabolic potential, while the particles are able to move freely along the z direction. Ground state configurations for varying length densities and screenings are analyzed and the structural transitions are studied as well.

Kurzfassung

Diese Dissertation gibt einen Überblick über die strukturellen und thermodynamischen Eigenschaften von finiten sphärischen komplexen Plasmakristallen - so genannten Yukawa balls. Diese neuartige Art von Wigner-Kristallen können direkt mit digitalen Videokameras analysiert werden. Die Experimente offenbaren deutlich eine Schalenstruktur und erlauben die Schalenbesetzungszahlen zu bestimmen, metastabile Zustände und Übergänge zwischen Konfigurationen, sowie Phasenübergänge, zu beobachten. Die experimentellen Beobachtungen der statischen Eigenschaften lassen sich gut durch ein vergleichsweise einfaches theoretisches Modell, dass die Staubteilchen durch ein parabolisches Potential eingefangen und mit einem isotropen Yukawa Potential wechselwirkend betrachtet, beschreiben. Innerhalb dieses Modells wurden umfangreiche Molekulardynamik- und Monte Carlo Simulationen durchgeführt, um sowohl die Konfigurationen des Grundzustandes und der angeregten Zustände, als auch das Schmelzverhalten zu untersuchen.

Die Grundzustandskonfigurationen der Yukawa balls hängen von der Stärke der Abschirmung ab; mit stärkerer Abschirmung wird eine Zunahme der Besetzung auf den inneren Schalen beobachtet. Hier werden insbesondere kleine Yukawa balls, $N \leq 60$, untersucht, die nicht nur diesen generellen Trend zeigen, sondern auch drei Arten von anomalem Verhalten bei Zunahme der Abschirmungsstärke und fixiertem N oder bei Erhöhung von N bei fixierter Abschirmung zeigen. Es wird gezeigt, dass dieses aussergewöhnliche Verhalten mit der speziellen Symmetrie der entsprechenden Konfigurationen zusammenhängt. Diese Effekte bei kleinen Teilchenzahlen beeinflussen auch das Verhalten beim Phasenübergang von flüssig-ähnlichem zu fest-ähnlichem Zustand. Die entsprechenden Schmelztemperaturen können auch für die mesoskopischen Systeme anhand von verschiedenen Schmelzkriterien bestimmt und verglichen werden. Die Ergebnisse zeigen, dass die Temperatureffekte die Stabilität der kleinen Yukawa balls im Experiment generell nicht beeinflussen, wobei Teilchenzahlen angegeben werden, wo radiale Übergänge auch im Experiment stattfinden könnten.

Als zweite Möglichkeit einer Anordnung von Staubpartikeln im Plasma wird ein System betrachtet, dass die Teilchen nur radial durch ein parabolisches Potential einfängt, während sich die Teilchen entlang der z Richtung frei bewegen können. Es werden Grundzustandskonfigurationen für unterschiedliche Längendichten und Abschirmungen betrachtet und die strukturellen Übergänge untersucht.

1. Motivation

Plasma is one of the less familiar states of matter. In our every day life we are used to neutral matter like solids and liquids; electrons are tightly bound to atoms and it takes a lot of energy to release them. Therefore, high temperatures are involved in the creation of a plasma at atmospheric pressures, temperatures that are not experienced often on earth. Still, more than 98% of the visible universe is estimated to be in the plasma state [1]. Stars and planets are continuously born from huge, but very cold plasmas called molecular clouds [2]. These, in a way, are enormous recycling factories in which the remnants of stars which have since long ceased to exist, are again used to form new stars.

Complex or dusty plasmas are gas plasmas consisting of electrons, ions, and

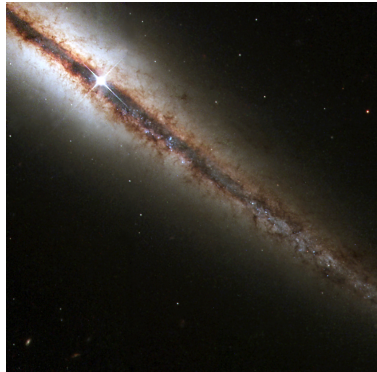


Figure 1.1.: Detailed view of huge dust clouds extending along, as well as far above, the galaxy's main disk. Dark clouds of interstellar dust stand out in the picture because they absorb the light of background stars. Most of the clouds lie in the plane of the galaxy, forming the dark band, about 500 light-years thick, that appears to cut the galaxy in two from upper right to lower left. The image of the galaxy NGC 4013 is courtesy of NASA and taken by the Hubble Space Telescope.

neutral atoms that additionally contain microscopic particles with sizes ranging from $10nm$ to some $10\mu m$. This state of matter is also ubiquitous in space, e.g. in the interplanetary medium, in interstellar clouds[3] (as seen in figure 1.1), in comet tails [4], and in the ring systems of the giant planets as well as in meso-

1. Motivation

spheric noctilucent clouds [5, 6]. At the same time, in microchip manufacturing, avoiding particle contamination during the many production steps that involve plasmas is a technological challenge [7, 8]. On the other hand, the growth, transport, and deposition of nanoparticles is the central goal of many plasma deposition techniques, e.g. in the manufacturing of amorphous solar cells [9–12]. Since the early 1990s, research in complex plasmas is rapidly evolving. The original name dusty plasmas is nowadays often replaced by “complex plasmas” – in analogy to complex fluids, in order to emphasize many fundamentally different properties of this medium that distinguish it from ordinary gas plasmas. The field of complex plasmas is now maturing and the interested reader can find timely monographs, e.g. on dusty plasmas in space [13], technological applications [14], or on waves in dusty space plasmas [15]. In any case, the microparticles in complex plasmas are electrically charged by collection of plasma electrons and ions as well as by photoemission or secondary electron emission [5, 6]. In laboratory plasmas usually the collection processes dominate and the particles attain a high negative charge of a few thousand elementary charges for a micrometer sized dust particle. This means that in laboratory plasmas, dust is confined inside plasma discharges by the electric field, since the outer parts of discharges also become negatively charged with respect to the bulk of the plasma. To some extent, complex plasmas behave like negative ion plasmas. In both cases a heavy, negatively charged species substitutes part of the electrons and thus affects the mobility and the contribution to shielding by negative charges.

1.1. Strongly coupled plasmas

Most ordinary plasmas in space and laboratory are weakly coupled, which means that the interaction energy of nearest neighbours is much smaller than their thermal energy. This situation is completely different in complex plasmas with micrometer sized particles in which the particles may become strongly coupled [16]: the negative charge can be so large that the interaction energy of nearest neighbour dust particles exceeds their thermal energy by several orders of magnitude. A consequence of strong coupling is the formation of liquid or solid phases. In 1934, a liquid to solid phase transition had been predicted by Eugene Wigner for the three-dimensional (3D) electron gas in metals at low temperature and low density due to strong Coulomb repulsion [17]. This phase transition became known as Wigner crystallization, and the solid phase as Wigner or Coulomb crystals. This kind of crystallization has been stud-

ied for decades in a variety of systems ranging from electrons trapped on top of liquid helium [18, 19], electrons trapped in semiconductor quantum wells [20] and quantum dots [21], radiofrequency discharges of dusty plasmas [22], hole crystallization in semiconductors [23] to laser-cooled trapped ions in Paul- and Penning traps [24–26], as seen in figure 1.2. It is remarkable that these

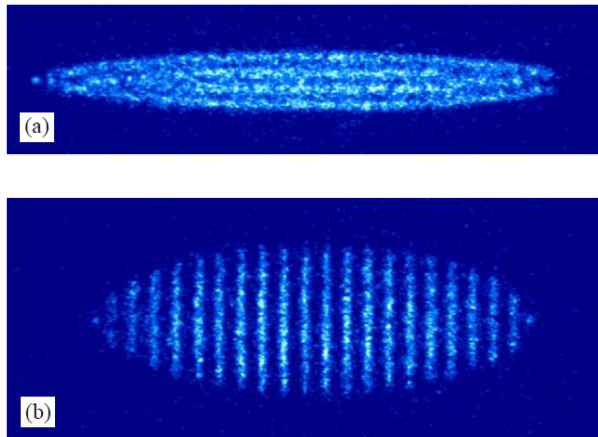


Figure 1.2.: Two images of the same ion crystal observed in the absence (a) and in the presence (b) of parametric resonances between the RF trap field and ion plasma modes, respectively. Images are taken from ref. [26].

physically completely different systems exhibit very similar collective behavior which is due to the governing role of the long-range Coulomb interaction. What makes the dust systems particularly attractive is that here collective phenomena, such as crystallization, occur at a comparatively large length scale of several millimeters and at room temperature which makes detailed experimental investigations rather simple. The formation of ordered solid phases in dusty plasmas was predicted by Ikezi [27] and first observed as plasma crystals in the early 1990s [28–30]. Since then crystalline structures and dynamical processes have been observed in a variety of confinement geometries ranging from $1d$ to $3d$, see e.g. reference [31] for an overview and additional references. This thesis will focus on the 3-dimensional spherical dust crystals recently observed by Arp et al. [32]. Their crystalline structure was found to be very similar to those observed before in ion crystals in Paul traps and the crystals which have been predicted to exist in expanding neutral plasmas [36, 37]. Compared to the latter, the advantage of these so called Yukawa balls is that the individual particle positions and trajectories can be directly visually observed and traced and recorded with video cameras. As a result, very detailed comparisons to theory and computer simulations can be performed which go far beyond comparisons

1. Motivation

in more traditional plasmas. In particular, the comparison is not limited to average quantities such as distribution functions on long time scales, but also covers correlation effects, fluctuations, and even short-time effects become accessible. Thus, complex plasmas are an excellent object to study in great detail static and dynamic phenomena in finite systems such as ground and metastable states, transitions between configurations and phase transitions. These properties have, in the past few years, been studied in a very close connection between experiment, theory and computer simulation.

1.2. Outline of this thesis

The focus of this thesis is the modeling of the dust component of a complex plasma on the example of Yukawa balls and Yukawa tubes by means of Monte Carlo simulations. The interest lies mainly in the structural and thermodynamic properties of these systems to get more insight in the stability of these systems. The findings are then compared to experimental observations.

Chapter 2 gives an introduction to the specific experimental setup and observable parameters of Yukawa balls, as well as an introduction to the simulation techniques used, concentrating on the Monte Carlo simulation method.

Chapter 3 presents the structural and thermodynamic properties of Yukawa balls as determined by the different simulations and compares those with experimental findings.

Chapter 4 deals with the simulation of Yukawa tubes, a type of complex plasma where the particles are confined only in two of the three spatial dimensions. The found ground states are analyzed and compared with those found in $2 - d$ dust layers.

A general summary and the conclusions of this thesis are then presented in **Chapter 5**, as well as recommendations for future research.

2. Introduction

2.1. Experiment

To realize and investigate spherical $3d$ dust clouds two ingredients are indispensable: an isotropic confinement to prevent Coulomb explosion of the alike charged particles and powerful $3d$ diagnostics to get the particles positions and velocities. The diagnostics are required to simultaneously measure all particle coordinates. Different approaches have been presented, ranging from the color-gradient method [38] via stereoscopic methods [39, 40] to digital inline holography [41]. The differences in time and space resolution are given in table 2.1, although further developments may enhance this. A detailed report on the progress in the field of $3d$ diagnostic tools is given in [42].

To produce $3d$ plasma crystals, a number of experiments have been performed under microgravity conditions. Although these experiments have provided many interesting observations of, e.g. localized crystalline structures [43], complex plasma boundaries [44, 45], coalescence of complex plasma fluids [46], transport properties [47, 48], low-frequency waves and instabilities [49–52], and most striking of the formation of a dust-free zone (void) in the center of the discharge [43, 53], $3d$ plasma crystals have not been found in the first experiments. The most exciting challenge was to close the void. Arp and coworkers [32] have modified the usual setup of an asymmetric capacitively coupled rf-discharge as seen in figure 2.1(a). The rf-electrode was heated to $T = (60 - 80)^\circ C$ to

	space resolution	time resolution
color-gradient	$3\mu m$ (x,y)	$40ms$
	$21\mu m$ (z)	
inline holography	$25\mu m$ (x,z)	$100\mu s$
	$30\mu m$ (y)	
stereoscopy	$15\mu m$ (x,y,z)	$20ms$

Table 2.1.: Time and space resolution for the different methods that provide the coordinates of all particles of Yukawa balls. Taken from references [38–41]

2. Introduction

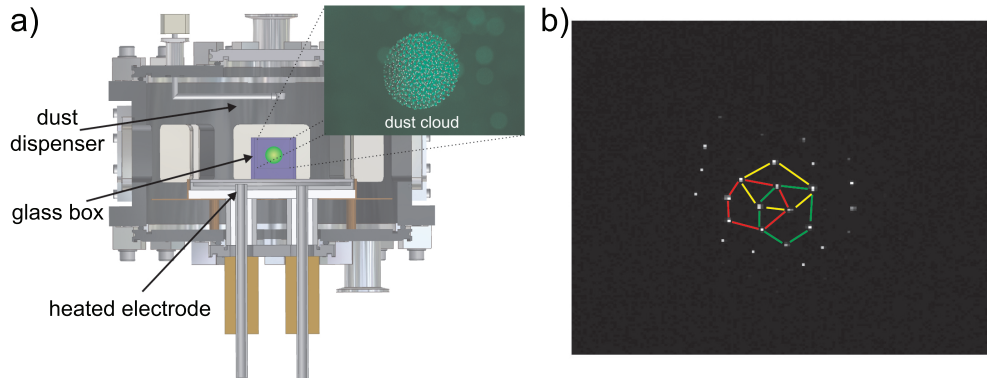


Figure 2.1.: (a) Side view of the discharge arrangement for Yukawa balls. The lower electrode is heated ($T < 90^\circ\text{C}$). The vacuum vessel is grounded and kept at room temperature. The dust cloud is confined inside a glass cube where the upper and lower side are left open. The inset shows an image of a large dust cloud with 1 cm in diameter. (b) A thin slice at the front side of the cloud is illuminated. The particles basically arrange in a hexagonal lattice. From reference [32].

establish a vertical temperature gradient. The grounded vacuum vessel was kept at room temperature. The resulting thermophoretic force should balance gravity for particles with a diameter $d < 6\mu\text{m}$ and allows dust levitation into the bulk plasma. In addition to the experimental setup used by Rothermel [54], Arp et al. proposed to place a glass box with square cross section on the electrode that was left open at the top and at the bottom. For low discharge power ($P < 10\text{W}$), they discovered that dust, which was dropped into the glass box, formed spherical void-free clouds [32]. A picture of a laser illuminated dust cloud (Yukawa ball) consisting of roughly 10000 dust particles is shown in the inset of figure 2.1(a). Already if only the front of such a dust cloud was illuminated with a laser sheet, interesting structural properties were observed as seen in figure 2.1(b). The particle arrangement was static and particles on the surface of Yukawa balls seemed to have preferably 5 or 6 nearest neighbors. Moreover, the particles did not form vertical chains. This was the first evidence found, that the Yukawa balls were in a solid or even crystalline state.

The question remained how the dust confinement is realized and what shape the confinement potential has, since it is a central input parameter for theory and simulation. In contrast to the well known external parabolic confinement of ion crystals in Paul or Penning traps [24, 25], the confinement of homogeneous spherical dust clouds involves various forces from the plasma environment. The

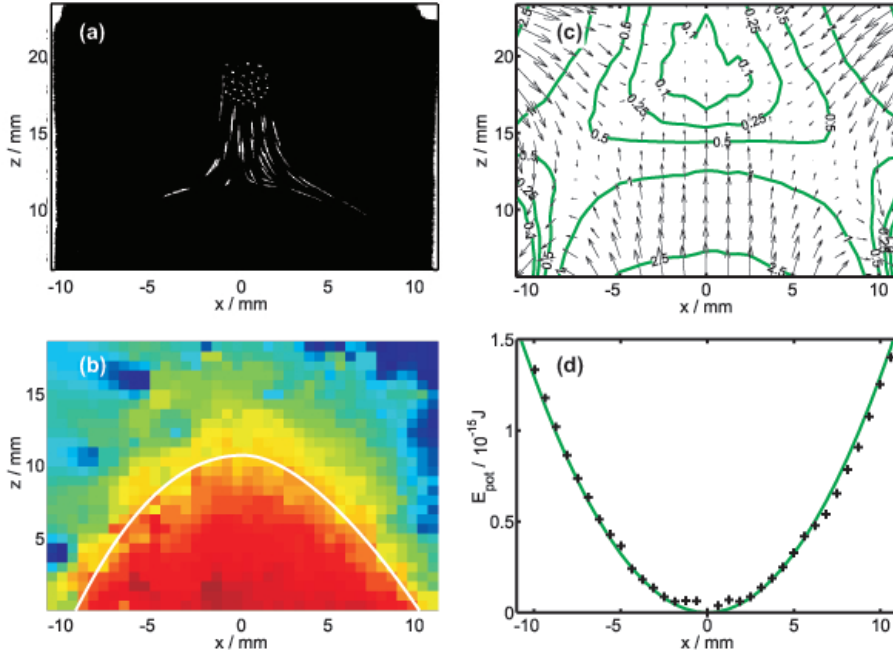


Figure 2.2.: Experiments on the confinement of Yukawa balls: (a) Superposition of multiple video frames. As soon as the discharge is switched off, the trapped particles fall down. Their motion is only affected by gravity and the thermophoretic force. (b) Vertical component of the experimentally determined thermophoretic force field. In 'red' regions the thermophoretic force exceeds gravity, in 'blue' regions gravity is dominant. The solid line shows where both forces balance. (c) Trap potential obtained from PIV measurements and fluid simulations. (d) A horizontal section through the trap center reveals an almost parabolic confinement. From reference [57].

contributions of the individual forces to confinement are not immediately evident.

Obviously the dust particles are influenced by *gravity*

$$\vec{F}_g = g_E m_d, \quad (2.1)$$

where g_E is the gravitational acceleration on Earth and depends only on the mass $m_d = 4/3\pi(d/2)^3$ of the dust particles.

The *neutral friction force* is given by [55]

$$\vec{F}_{fr} = -m_d \beta_{fr} \vec{v}_d, \quad (2.2)$$

2. Introduction

with dust particle velocity \vec{v}_d and the Epstein friction coefficient β_{fr} , which is given by

$$\beta_{fr} = \delta \frac{8}{\pi} \frac{2p_{gas}}{\rho dv_n}, \quad (2.3)$$

using $v_n = \sqrt{8k_B T_n / \pi m_n}$ for the thermal velocity of the neutral gas with temperature T_n , k_B the Boltzmann constant and the mass m_n of Argon (40 amu). The Milikan coefficient δ is determined from experiments with free-falling particles to be $\delta = 1.3$, consistent with theoretical values [55] and other experiments [56].

According to [54] the *thermophoretic force* is given by

$$\vec{F}_{th} = -4.67nk_B\lambda \left(\frac{d}{2}\right)^2 \vec{\nabla}T, \quad (2.4)$$

depending on the particle diameter d for a fixed temperature gradient $\vec{\nabla}T$ of the neutral gas. Typical values in the experiment [32] are the mean free path for atom-atom collisions $\lambda = 1.26 \cdot 10^{-4}m$ at $50Pa$ in Argon gas, the number density $n \approx 0.1mm^{-3}$ and the diameter of the dust particles $d = 9.55\mu m$. It was found that thermophoresis alone was not sufficient to explain the confinement (figure 2.2(a)). By means of particle imaging velocimetry (PIV) experiments the thermophoretic force field could be measured (figure 2.2(b)). It was found that thermophoresis gave about 70% contribution to the vertical confinement. The remaining 30% and the radial confinement were provided by plasma induced forces, namely electrostatic fields due to surface charges on the glass [57]

$$\vec{F}_E = q_d \vec{E}. \quad (2.5)$$

In order to determine the influence of the plasma on the trapped dust particles, the electric field force and the ion-drag force are derived from fluid simulations with the SIGLO-2D code [58, 59]. The electric field force \vec{F}_E depends on the electric field \vec{E} , which is obtained from the simulation and the dust charge $q_d \approx 1100e$. The dust charge is lower than in the orbital-motion-limit (OML) model [60] since the particles are densely packed [61].

Further, the fluid simulations showed that the Yukawa balls were confined in a region where the plasma production was negligible. Due to the low plasma density, $n \approx 10^{13}m^{-3}$, and the weak electric fields the ion drifts were significantly below the ion sound speed. The resulting *ion-drag force* \vec{F}_{ion} has been derived [57] from simulating the model of Khrapak [62]. In comparison with \vec{F}_E , the topology of the field is inverted. In the whole region of the trap, the ion-drag force is smaller than the electric field force by two orders of magnitude. Thus,

the ion-drag force does not contribute to the topology of the trap.

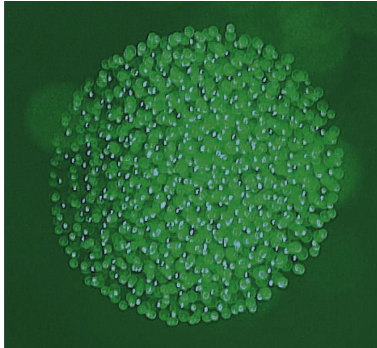


Figure 2.3.: Photograph of a typical Yukawa ball with several hundred particles. The ball has a diameter of about 7mm , the individual particles have a size of $3.5\mu\text{m}$. The spherical shape of the dust cluster is clearly visible. The image is taken from reference [66].

The summary of these forces as determined in the experiment [32] is given in figure 2.2. The confinement provided by the combination of gravity, thermophoresis and electric fields is plotted in figure 2.2(c) and is in very good agreement with the experimental observations in figure 2.2(a). The green contour lines indicate the potential energy of a sample particle ($q_d = 2000e$) in units of $10^{-15}J$. The energy varies from $0 \cdot 10^{-15}J$ ($x = 0\text{mm}$, $z = 19\text{mm}$) at the point where the Yukawa ball is located to $2.5 \cdot 10^{-15}J$. It yields the correct levitation height, its depth is sufficient to trap particles with a few hundred elementary charges and even its asymmetry was observable for huge clouds in the experiment [57]. A quantitative description of the dust confinement could be achieved and the horizontal section through the trap center in figure 2.2(d) reveals an almost parabolic confinement $U_{conf}(r) = \alpha/2r^2$, which is used in the model Hamiltonian (3.1). Furthermore, for the trapping process an interaction of dust and plasma, as proposed by Totsuji [63, 64], is not required. This conclusion is based on the measurements of the confinement potential which fully agreed with the observed position and shape of the dust cloud without taking into account any dust-plasma interaction [57]. The reason is that in these experiments only a small amount of dust ($n_d \ll n$) is involved. Thus, the particle trap is provided by external forces only, so despite the differences the trap geometry is closely related to those of Penning and Paul traps [65]. This allows for a direct comparison of the structural properties of Yukawa balls and e.g. trapped laser-cooled ions. Figure 2.3 shows a typical Yukawa ball with several hundred particles in a similar setup [66]. The ball has a diame-

2. Introduction

ter of about $7mm$, the individual particles have a size of $3.5\mu m$. For further structural analysis and especially for comparison with simulations as well as with other strongly coupled systems, it is important to note that the trapping potential is essentially isotropic and parabolic for dust clouds with a radius of less than $2mm$, i.e. $N < 1000$ particles; clusters with more particles sometimes have deviations from spherical symmetry, because the confinement is often not isotropic for clusters of this size, cf. figure 2.2(c).

2.2. Simulation techniques

Since the time evolution of the dust particles is on a much larger time scale than that of the surrounding ions and electrons, the system can be treated classically. The effect of the surrounding plasma on the dust can be condensed in a parameter and therefore exact simulation methods for classical systems can be used which include molecular dynamics (MD), Langevin dynamics (LMD) and Metropolis Monte Carlo (MC). The current work focuses on the structural properties of the ground and first metastable states as well as the thermodynamic properties of these Yukawa balls and on the methods of molecular dynamics and Monte Carlo. For dust particles in cylindrical geometry due to a different confinement, the so called Yukawa tubes, a different method is used, the Ewald summation. This will be described in detail in section 4.1.

2.2.1. Molecular dynamics

For the presented results on structural properties mainly a molecular dynamics simulation has been used. The results were also partly achieved and confirmed by a self implemented Monte Carlo simulation. Molecular dynamics solves Newton's equations corresponding to the Hamiltonian (3.1)

$$\dot{\mathbf{p}}_i(t) = -\alpha\mathbf{r}_i + \sum_{j \neq i} \frac{q^2}{4\pi\epsilon r_{ij}^3} (1 + \kappa r_{ij}) \mathbf{r}_{ij} \cdot e^{-\kappa r_{ij}}, \quad i = 1, \dots, N, \quad (2.6)$$

with the initial conditions

$$\mathbf{r}_i(0) = \mathbf{r}_i^0, \quad \mathbf{p}_i(0) = \mathbf{p}_i^0. \quad (2.7)$$

The parameters α , ϵ and κ are explained in section 3.1. The coupled system (2.6) of ordinary differential equations is efficiently solved for up to several thousand particles by standard techniques such as Runge-Kutta methods. The

present version gives a solution in the microcanonical ensemble where the total energy H is conserved. In order to obtain the ground states the initial conditions have been chosen randomly and in each time step the velocities have been reduced by less than 0.1% until all forces on the particles are zero. For each parameter set (κ, N) this procedure has been repeated several hundred times to distinguish metastable states from the exact ground state. The state with the lowest energy is assumed to be the ground state, although this can only be said with high probability, since there might be states with lower energy that weren't found in the simulations.

2.2.2. Monte Carlo

The method of choice to study thermodynamic equilibrium properties are Monte Carlo simulations. This first principle method has been used in this work, while the results were in some test cases verified by LMD simulations, which is based on MD with the inclusion of friction and a random process which simulates a thermostat. Since the implementation of a Monte Carlo simulation was part of this work, a more detailed description is given.

Monte Carlo simulation methods are especially useful in studying systems with a large number of coupled degrees of freedom, such as fluids [67], disordered materials [68], strongly coupled solids, and cellular structures [69]. The name ‘‘Monte Carlo’’ was popularized by physics researchers Stanislaw Ulam, Enrico Fermi, John von Neumann, and Nicholas Metropolis, among others working on nuclear weapon projects in the Los Alamos National Laboratory [70]. The name is a reference to the Monte Carlo Casino in Monaco where Ulam’s uncle borrowed money to gamble [71]. The use of randomness in the simulations and the repetitive nature of the process are analogous to the activities conducted at a casino.

Equilibrium statistical mechanics is based upon the idea of a partition function which contains all of the essential information about the system under consideration. The general form for the partition function for a classical canonical (N, V, T) ensemble is

$$Z = \int_{\Omega} \rho(\vec{x}) d^3 \vec{x}^N = \int_{\Omega} e^{-\beta H(\vec{x})} d^3 \vec{x}^N, \quad (2.8)$$

where Ω is the phase space, $x = (\vec{r}_1, \dots, \vec{r}_N, \vec{p}_1, \dots, \vec{p}_N)$ a state in the phase space, $\beta = 1/k_B T$ with the temperature T and the Boltzmann constant k_B , and H is the Hamiltonian of the system. The integral is over all possible

2. Introduction

states in phase space and thus depends on the system size and the number of degrees of freedom of each particle. Only for systems which either consist only of a few particles or where the interaction is very simple, the evaluation of the partition function in closed form is possible. With help of the partition function, thermodynamic expectation values can be calculated as

$$\langle f \rangle = \frac{\int_{\Omega} f(\vec{x}) \rho(\vec{x}) d^3 \vec{x}^N}{\int_{\Omega} \rho(\vec{x}) d^3 \vec{x}^N}, \quad (2.9)$$

where f is the observable of interest, for example the potential energy. Splitting the Hamiltonian in (2.8) into kinetic energy T and potential energy V leads to the expectation value

$$\langle f \rangle = \frac{\int \int_{V^N} f(\vec{r}) e^{-\beta(T(\vec{p})+V(\vec{r}))} d^3 \vec{p}^N d^3 \vec{r}^N}{\int \int_{V^N} e^{-\beta(T(\vec{p})+V(\vec{r}))} d^3 \vec{p}^N d^3 \vec{r}^N}. \quad (2.10)$$

Then, the integrals over the momenta $d^3 \vec{p}^N$ can be canceled out and only

$$\langle f \rangle = \frac{\int_{V^N} f(\vec{r}) e^{-\beta V(\vec{r})} d^3 \vec{r}^N}{\int_{V^N} e^{-\beta V(\vec{r})} d^3 \vec{r}^N} \quad (2.11)$$

remains. The central limit theorem now says, that the arithmetic average over the random values $f(x_i)$ is in the limit of large samples N a normal distribution with average $\langle f \rangle$

$$\langle f \rangle = \lim_{N \rightarrow \infty} \frac{1}{N} \sum_{i=1}^N f(x_i) \pm \sqrt{\frac{\langle f(x)^2 \rangle - \langle f(x) \rangle^2}{N}}. \quad (2.12)$$

This is the central idea of a Monte Carlo simulation [72–74]. The only question that remains, is how to choose the random states $f(x_i)$. The simplest way would be to choose evenly distributed states, the *simple sampling*. This method fails or becomes costly in computer time when the real distribution of the states $f(x_i)$ is far away from an equipartition. Therefore, the best way to choose these random states would be Boltzmann distributed states, which is done by *importance sampling*. In order to generate such a chain of states, a *Markov chain*, the states x_i are chosen by simulating a Markov process with the transition probability $P(x \rightarrow y)$

$$\sum_{y=1}^N P(x \rightarrow y) = 1, \quad \forall x, \quad (2.13)$$

where

$$0 \leq P(x \rightarrow y) \leq 1. \quad (2.14)$$

2.2. Simulation techniques

This transition probability is time independent, therefore not relying on other states, which is the necessary condition for the Markov process. Also, the distribution of states p_x should result in the Boltzmann distribution. And furthermore, it should be possible to reach all possible states x with a finite number of steps. This is a requirement, so that the algorithm is quasi ergodic; the statistical average of the states equals the time average. In that case the detailed balance condition [75]

$$p_x P(x \rightarrow y) = p_y P(y \rightarrow x), \quad (2.15)$$

is sufficient to guarantee that the states are distributed according to the Boltzmann distribution. It is obvious from (2.15), that

$$e^{-\beta(E_y - E_x)} = \frac{p_y}{p_x} = \frac{P(x \rightarrow y)}{P(y \rightarrow x)}. \quad (2.16)$$

Every transition probability $P(x \rightarrow y)$ that meets that demand, meets also the more general requirement for the equilibrium, that the sum over all transitions from a state x to all other states has to be equal the sum of the transitions from all other states to the state x . Also, it is clear that for any initial distribution $p_0 = (x_0^1, \dots, x_0^N)$ the system evolves to the stationary distribution $p_x = \frac{e^{-\beta E_x}}{Z}$. For more details on Monte Carlo simulations see [72–74] and references therein.

Metropolis algorithm and its implementation

The Metropolis algorithm [76] is one possible choice to meet these demands and is as follows. The first configuration p_0 is randomly generated. At each point in the construction of the chain of configurations a move is attempted to a new configuration.

If the difference between the energy of the new configuration and the energy of the old configuration, $\Delta E = E_y - E_x$, is negative (i.e. the energy of the new configuration is lower than the old one), then the move is accepted and the new configuration becomes a state in the Markov chain. If ΔE is positive, however, a random number r between 0 and 1 is generated and the resulting configuration is only accepted if $e^{-\beta \Delta E} > r$ and otherwise refused. This is the so called Metropolis criterion

$$P(x \rightarrow y) = \begin{cases} e^{-\beta(E_y - E_x)} & \text{for } (E_y - E_x) > 0 \\ 1 & \text{otherwise} \end{cases}. \quad (2.17)$$

2. Introduction

The sequence of successive random steps is called a random walk through the phase space.

With help of the Metropolis algorithm and the generated Markov chain of states all observables can be calculated by equation (2.12). To compute the Markov chain the system has to be in thermodynamic equilibrium, which is achieved by simulating a few thousand ($\approx 10^4$) Monte Carlo steps without taking them into account for the Markov chain. In that time the system can pass from a randomly initialized state to thermodynamic equilibrium. Also note that these states have to be independent to fulfill the error estimate. Therefore, tests have to be conducted on the implemented algorithm.

Statistical tests of the Markov process

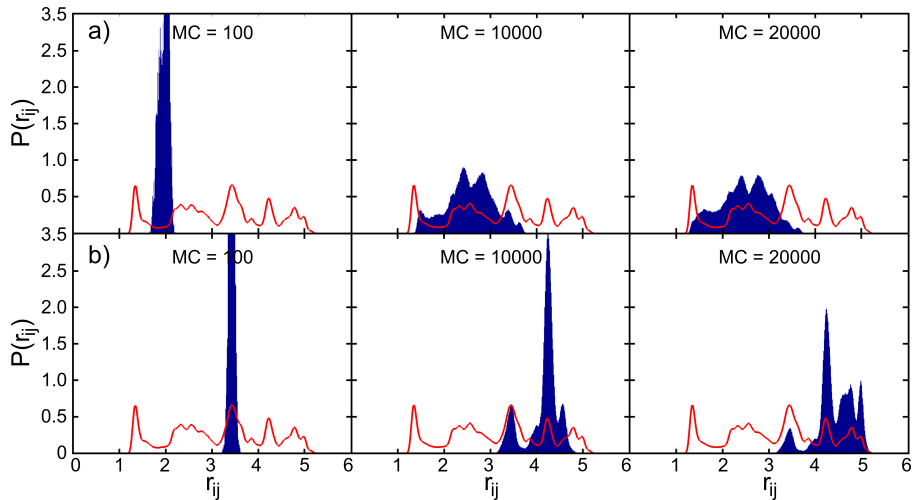


Figure 2.4.: The red lines, which have the same shape in all pictures, show the probability $P(r_{ij})$ to find any pair with the distance r_{ij} averaged over all pairs and 10^7 Monte Carlo steps of a simulation of a Yukawa ball with $N = 31$ particles at very low temperature ($\Gamma_C = 1000$). For computation r_{ij} is an interval $r_{ij} \pm \delta$, where the pair distances within that interval are counted. The blue histograms show the same probability for (a) the pair with the indices 1 and 3 and (b) 4 and 8, averaged only over 100, 10000 and 20000 Monte Carlo steps. With increasing number of Monte Carlo steps the pair distance distribution of a single pair (blue) begins to produce the same kinks as the overall distribution (red).

The assumption of *ergodicity* means that the random samples r_1, \dots, r_N of a finite time series will converge towards the moments of the population for

2.2. Simulation techniques

$N \rightarrow \infty$. The Markov chain has to be average and variance ergodic but these properties cannot be proved empirically. For this, it would have to be shown that all possible states of the system can be reached by a finite number of Monte Carlo moves. In this case the abundance of possible states is not known beforehand. What is possible, is to follow the trajectories of individual particles during the simulation and see if they are able to “travel” through the cluster. In figure 2.4 the probability to find a pair with the distance r_{ij} is shown for two different pairs of a cluster with $N = 31$ particles at a very low temperature, $\Gamma_C = 1000$. The definition of the Coulomb coupling constant Γ_C can be found in section 3.2.2, equation (3.12). The red line shows the probability to find a pair with that distance of the same cluster, where the probability of the pair distances of all pairs are recorded over a simulation with 10^7 Monte Carlo steps. This should be the thermodynamic average of the probability to find a pair with a distance r_{ij} . The blue histograms show the probability for (a) the pair with the particles 1 and 3 and (b) the pair with the particles 4 and 8 during the Monte Carlo simulation. After 100 Monte Carlo steps in both cases (a) and (b) the particles have only been moved in their local potential, the pair distance is almost Gaussian distributed around the mean value. After 10000 and 20000 Monte Carlo steps the pairs, or at least one particle of the pair, have moved throughout the cluster. The probability distribution begins to show peaks at the same positions as the probability distribution averaged over all pairs and the complete simulation of 10^7 Monte Carlo steps. The time or number of steps until the probability distribution of a single pair has converged against the overall probability distribution depends, of course, on the temperature which influences the step size of the replacement. Although this is not a strict proof, it is at least a good indicator that the Markov chain is ergodic, especially when considering that the given example is for a very low temperature.

In order to generate the Markov chain, a sequence of random numbers has to be generated for each Monte Carlo step. A *Monte Carlo step* is defined as a sequential sweep over all particles, where for each particle a move in the sense of equation (2.17) will be performed. Real random numbers, such as thermal noise in Zener diodes, are normally not useful in computer programs, instead pseudo-random number generators (RNG) are used. Here, the Mersenne Twister generator [77] which has a period of $2^{19937} - 1 \approx 4.3 \cdot 10^{6001}$ was used after it passed the *frequency test* and *block test* [72, 73]. The frequency test checks if it generates uniformly distributed numbers, where the block test checks if blocks

2. Introduction

of numbers for all possible lengths are uniformly distributed.

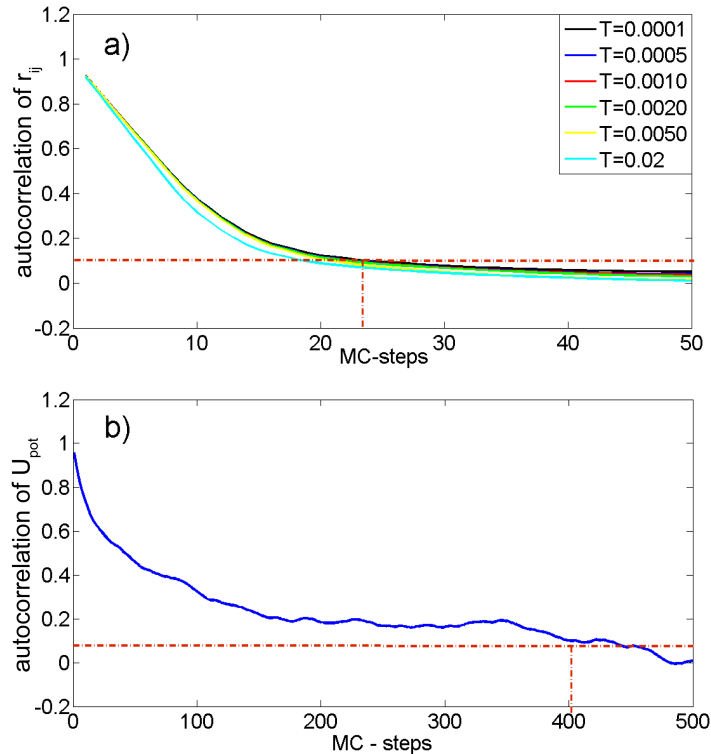


Figure 2.5.: Autocorrelations of (a) the total potential energy of a Yukawa ball with $N = 31$ particles and (b) the pair distance r_{13} of particles with index 1 and 3 of the same cluster versus the number of Monte Carlo steps. In (a) the autocorrelation is shown for different temperatures, but the autocorrelation time of $k \approx 23$ Monte Carlo steps does not change much. The autocorrelation time for the pair distance of $k \approx 400$ Monte Carlo steps is much larger. Therefore, it is mandatory to calculate the autocorrelation time for each observable before computing the average of this observable.

Last but not least, in order to compute statistical averages according to equation (2.12) the states have to be independent. For a discrete process of length N $X_1, X_2, \dots, \dots, X_N$ with known mean μ and variance σ , an estimate of the *autocorrelation* may be obtained as

$$\hat{R}(k) = \frac{1}{(N-k)\sigma^2} \sum_{t=1}^{N-k} [X_t - \mu][X_{t+k} - \mu] \quad (2.18)$$

for any positive integer $k < N$. When the true mean μ and variance σ are not known then it is possible to replace both by the sample mean and sample

2.2. Simulation techniques

variance, it is then a *biased estimate*. For randomness, autocorrelations should be near zero, a significance level should be defined, here it will be 0.1 for all observables. If the autocorrelation $\hat{R}(k)$ is lower (higher) than this upper (lower) bound, it is assumed that there is no autocorrelation at and beyond this lag k , the *autocorrelation time*. In figure 2.5(a) the autocorrelation for the potential energy of a Yukawa ball with $N = 31$ particles is shown. The autocorrelation of the total potential energy, the sum of interaction and confinement potential, has been computed for different temperatures, ranging from $T = 0.0001E_0$ to $T = 0.02E_0$. There cannot be seen much of a difference in the autocorrelation time. After about 23 Monte Carlo steps the autocorrelationfunction has decayed to below 0.1, and the potential energy can be assumed to be uncorrelated. This value can change dramatically for other observables, as seen in figure 2.5(b). Here, the autocorrelation of the pair distance r_{13} between the particles with index 1 and 3 of the same system with $N = 31$ particles has been computed and in this case the autocorrelation time is much larger, $k \approx 400$ MC-steps. So, the autocorrelation time has to be computed for every observable of interest, before the average (2.12) is calculated. Only states of the Markov chain are used that are separated by the number of Monte Carlo steps given by the autocorrelation time.

3. Yukawa balls

3.1. Model

A standard model to describe the Yukawa balls and their dynamics is based on the Hamiltonian ¹

$$H(\mathbf{r}_1 \dots \mathbf{r}_N, \mathbf{p}_1 \dots \mathbf{p}_N) = \sum_{i=1}^N \frac{\mathbf{p}_i^2}{2m} + \sum_{i=1}^N \frac{\alpha}{2} \mathbf{r}_i^2 + \frac{1}{2} \sum_{i \neq j}^N \frac{q^2}{4\pi\epsilon r_{ij}} \cdot e^{-\kappa r_{ij}}, \quad (3.1)$$

containing kinetic energy, a confinement and the interaction energy. The isotropic and parabolic confinement is based on the experimental results [57], cf. chapter 2.1. q is the particle charge and α the confinement strength. Finally, ϵ is the background dielectric constant and r_{ij} is the distance between particles i and j . The effect of the surrounding plasma on the dust is condensed in the static screening parameter κ which will be treated as a parameter below. All particles are considered to have identical mass and charge, which is a good approximation of the experimental conditions, since the diameter of commercially available dust particles fluctuates by less than one percent and the remaining charge variations were shown to have a negligible effect on the structure of Yukawa balls [78]. Then, the equation (3.1) can be split into relative and center of mass motion. For two particles the coordinates are converted

$$\{r_1, r_2\} \rightarrow \begin{cases} r = r_1 - r_2 \\ R = \frac{r_1 + r_2}{2} \end{cases}, \quad (3.2)$$

so that, with $r_1^2 + r_2^2 = (2R)^2 + r^2$, the Hamiltonian reads

$$\begin{aligned} H &= \alpha R^2 + \frac{\alpha}{2} r^2 + \frac{q^2}{4\pi\epsilon r} \cdot e^{-\kappa r} \\ &= U_{cm}(R) + U_{rel}(r). \end{aligned} \quad (3.3)$$

¹Improved models will be discussed in section 3.2.4.

3. Yukawa balls

In the case of Coulomb interaction ($\kappa = 0$) the equilibrium distance and the according energy can be easily derived from $U'_{rel} = 0$,

$$r_{0C} = \left[\frac{q^2}{4\pi\epsilon\alpha} \right]^{1/3} \quad (3.4)$$

$$E_{0C} = \frac{3}{2} r_{0C}^2 \alpha = \frac{3}{2} \frac{q^2}{4\pi\epsilon r_{0C}}. \quad (3.5)$$

Figure 3.1 shows the equilibrium positions for two particles interaction via

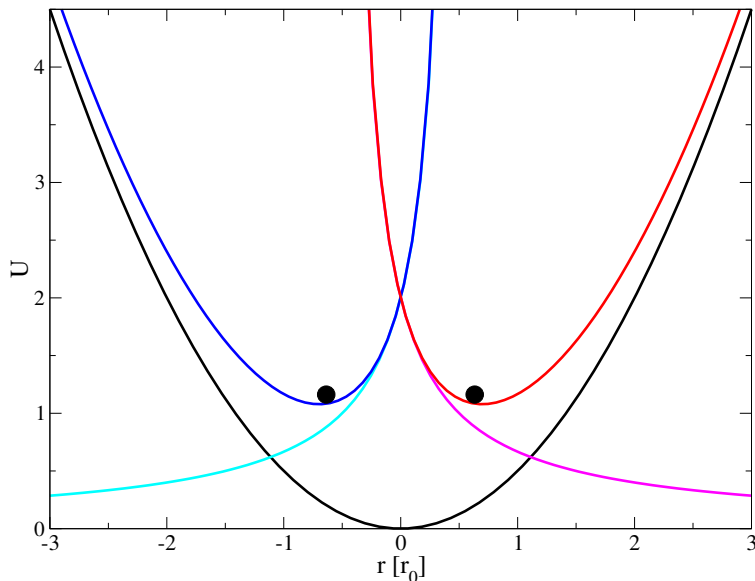


Figure 3.1.: The local particle potentials (blue and red) resulting from superposition of the external potential (black) and the interaction potentials (cyan and magenta). The minima of the local particle potentials are the equilibrium positions (black dots) of the two particles.

Coulomb force in a parabolic potential. With these length and energy scales the Hamiltonian (3.1) can be rewritten dimensionless as

$$\begin{aligned} \frac{H(\mathbf{r}_1 \dots \mathbf{r}_N)}{E_{0C}} &= \frac{1}{3} \sum_{i=1}^N \left(\frac{r_i}{r_{0C}} \right)^2 + \frac{2}{3} \sum_{i \neq j}^N \frac{r_{0C}}{r_{ij}} \cdot e^{-\kappa r_{ij}} \\ &= \frac{1}{3} \sum_{i=1}^N \tilde{r}_i^2 + \frac{2}{3} \sum_{i \neq j}^N \frac{1}{\tilde{r}_{ij}} \cdot e^{-\tilde{\kappa} \tilde{r}_{ij}}. \end{aligned} \quad (3.6)$$

All distances are now measured in units of the two particle equilibrium distance r_{0C} and all energies in the ground state energy of the two particle system E_{0C} . This also results in a dimensionless screening parameter $\tilde{\kappa} = r_{0C}\kappa$. To simplify

the reading, the tilde will be omitted in further equations.

For Yukawa interaction the equilibrium distance is not as easily derived as for Coulomb interaction. Here, the equilibrium distance can only be given as an implicit function [80]

$$\frac{e^{\kappa r_{0Y}} r_{0Y}^3}{1 + \kappa r_{0Y}} = r_{0C}^3. \quad (3.7)$$

Nevertheless, already a Taylor expansion for small screenings $\kappa r_{0Y} < 1$

$$r_{0C}^3 = \frac{e^{\kappa r_{0Y}} r_{0Y}^3}{1 + \kappa r_{0Y}} \approx r_{0Y}^3 \left\{ 1 + \frac{1}{2} \frac{\kappa^2 r_{0Y}^2}{1 + \kappa r_{0Y}} + \mathcal{O}\left(\frac{(\kappa r_{0Y})^3}{1 + \kappa r_{0Y}}\right) \right\} = r_{0Y}^3 \cdot k_1^{-1}(\kappa r_{0Y}),$$

can give an insight into the effect of the screening. The function $k_1(\kappa r_{0Y})$ can be calculated iteratively, starting with $r_{0Y} \approx r_{0C}$

$$\begin{aligned} k_1(\kappa r_{0Y}) &= \frac{r_{0Y}^3}{r_{0C}^3} \approx \frac{(1 + \kappa r_{0C})}{e^{\kappa r_{0C}}} \approx \frac{1 + \kappa r_{0C}}{1 + \kappa r_{0C} + \frac{1}{2} \kappa^2 r_{0C}^2} \\ &\simeq 1 - \frac{1}{2} \frac{\kappa^2 r_{0C}^2}{(1 + \kappa r_{0C})}. \end{aligned} \quad (3.8)$$

Since $\kappa^2 r_{0C}^2 / (2(1 + \kappa r_{0C})) > 0$ it is clear that the cluster compresses with increased screening. A more thorough approximation of equation (3.7) for higher screenings ($\kappa \leq 4$) can be given with the assumption of $r_{0Y} = r_{0C} + z$, where $|z| \ll r_{0C}$ and $z = \kappa(r_{0Y} - r_{0C})$. With $x \stackrel{\text{!}}{=} r_{0Y} \kappa$ and $x_C \stackrel{\text{!}}{=} r_{0C} \kappa$ then follows

$$\begin{aligned} e^x &= \left(\frac{x_C}{x}\right)^3 (1 + x) \\ x_C + z = x &= 3 \ln\left(\frac{x_C}{x_C + z}\right) + \ln(1 + x_C + z) \\ &= \ln(1 + x_C) + \ln\left(1 + \frac{z}{1 + x_C}\right) + 3 \ln\left(\frac{1}{1 + \frac{z}{x_C}}\right) \\ &\stackrel{|z| \ll x_C}{\simeq} \ln(1 + x_C) + \frac{z}{1 + x_C} + 3 \ln\left(1 - \frac{z}{x_C}\right) \end{aligned}$$

and therefore

$$x_C = \ln(1 + x_C) - z \left\{ \frac{1}{1 + x_C} - \frac{3}{x_C} - 1 \right\}, \quad (3.9)$$

and

$$z = \frac{\ln(1 + x_C) - x_C}{x_C^2 + 3x_C + 3} x_C (1 + x_C) < 0, \quad (3.10)$$

because of $\ln(1 + x_C) - x_C < 0$ [80, 85]. The influence of the screening on the two particle equilibrium distance is shown in figure 3.2. For $r_{0C} = 1$ the values for the approximate equilibrium distances are given in table aside. For example, the equilibrium distance for two Yukawa interacting particles with a screening

3. Yukawa balls

value of $\kappa = 0.6$ is 4% smaller than in the Coulomb case. It is also obvious that the relative error of the approximation with a simple Taylor expansion (3.8) is increasing dramatically for screenings $\kappa > 1.0$, while approximation (3.10) holds true for the shown range of screening with an relative error of 5% at $\kappa = 4.0$ against the data computed from Monte Carlo simulations.

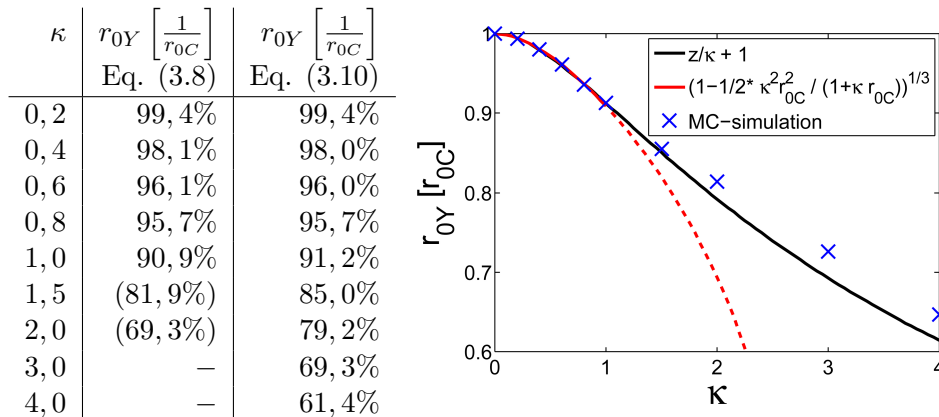


Figure 3.2.: The table shows the equilibrium distance for two Yukawa interacting particles in units of the Coulomb equilibrium distance for the approximations (3.8) (column 2) and (3.10) (column 3). The simple Taylor expansion approximation (3.8) should only be used for screenings $\kappa \leq 1.0$, while the second approximation (3.10) has a relative error of less than 5% (at $\kappa = 4.0$) compared to the equilibrium distance computed by Monte Carlo simulations. This is also shown in the figure, here the crosses mark the Monte Carlo data, the red (dotted) line is the approximation (3.8), while the black line is the approximation (3.10).

3.2. Structural properties

The first interest in these systems is focused on the structural properties of the Yukawa balls. From experiments [32–35] and simulations it is clear that the dust particles arrange themselves in a nested shell structure, as seen in figure 3.3. The concentric shells are filled up to a precise number of particles before a new outer shell is started. The exact shell closures and configurations depend on the total number of particles and the screening κ of the interaction. This behavior will be analyzed in detail for the ground state configurations in the following subsection.

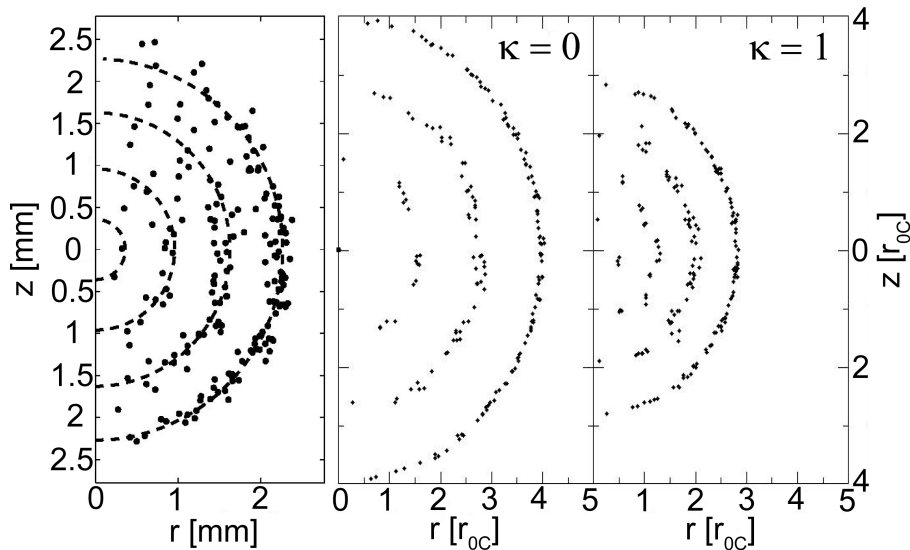


Figure 3.3.: Radial particle distribution for a Yukawa ball with $N = 190$ particles given in cylindrical coordinates. On the left the experimental configuration [32] is shown, while the other two figures display results of simulations for Coulomb ($\kappa = 0.0$) and Yukawa ($\kappa = 1.0$) interaction. The units of length for the simulations are shown in units of the Coulomb two particle equilibrium distance r_{0C} . From reference [80].

3.2.1. Ground states

The first investigation of the model (3.1) was performed by Avilov and Hasse in 1991 [81]. They studied the model for Coulomb interaction ($\kappa = 0.0$) and were able to present ground state energies and configurations for these systems. Nevertheless, the molecular dynamics and Monte Carlo simulations showed substantial deviations from their findings. Some examples of these differences in energy and even in the configuration are given in the table 3.1. The configurations are given by the numbers of particles on each shell, where the first number in the brackets denotes the number of particles on the outermost shell and the next numbers the shell populations for the next shells. Shells are counted from outwards to inwards. Already this short comparison shows the main aspects that are important to find the ground state configurations and energies of these clusters. At first it is necessary to perform the simulations with a high precision in energy and second it is mandatory to repeat the simulations as often as possible to ensure with a high probability that the ground state is reached. If the simulation to find the ground state is only performed once, it is likely that final state is just a metastable state, since only indefinitely long simulations,

3. Yukawa balls

where either the heat bath or the movement of the particles is reduced by an infinitesimal small amount, ensure that the ground state is reached. Since this cannot be done in limited time, the simulations are repeated approximately 1000 times for each total number of particles.

N	configuration			energy per particle (E/N)		
	Avilov/ Hasse	MD	MC	Avilov/ Hasse	MD	MC
3	(3)	(3)	(3)	1.0400	1.04004	1.04004
4	(4)	(4)	(4)	1.4174	1.41741	1.41741
12	(12)	(12)	(12)	3.8407	3.84069	3.84069
13	(12, 1)	(12, 1)	(12, 1)	4.1009	4.10089	4.10089
28	(24, 4)	(25, 3)	(25, 3)	7.4200	7.4198	7.41980
29	(26, 3)	(25, 4)	(25, 4)	7.6162	7.6159	7.61590
30	(27, 3)	(26, 4)	(26, 4)	7.8098	7.8092	7.80919
31	(28, 3)	(27, 4)	(27, 4)	8.0026	8.0001	8.00011
34	(30, 4)	(30, 4)	(30, 4)	8.5648	8.5647	8.56470
35	(30, 5)	(30, 5)	(30, 5)	8.7488	8.7487	8.74874
40	(34, 6)	(34, 6)	(34, 6)	9.6437	9.6436	9.64361

Table 3.1.: Ground state configurations and energies, computed from molecular dynamics (MD) simulations by Avilov and Hasse [81], Ludwig et al. [82] and Monte Carlo (MC) simulations within this work. The differences in the ground state configurations and energies begin with $N = 28$ particles. Sometimes, although the same configurations are noted, the ground state energy differs slightly, e.g. $N = 34$.

The comparison of experimental configurations with those found in simulations shows that for a fixed number of particles the arrangement of particles on the shells differs. An example for $N = 190$ is shown in figure 3.3. First, note that the radius of the Yukawa ball in the simulations differs between the ground state configuration of the Coulomb ball and the Yukawa ball ($\kappa = 1.0$). With increased screening the Yukawa ball gets smaller, which also means that the interparticle distance decreases as predicted in section 3.1.

The second difference is observed when the shell populations for simulations with different screening parameter are compared with the experimental configuration, cf. table 3.2. Clearly, for $\kappa = 0.0$ the simulation results yield systematically more particles in the outer part of the cluster than observed in

3.2. Structural properties

$\kappa \rightarrow$	0.0	0.2	0.3	0.4	0.5	0.6	1.0	experiment
N_4	1	1	2	2	2	2	4	2
N_3	18	18	20	20	21	21	24	21
N_2	56	57	57	58	58	60	60	60
N_1	115	114	111	110	109	107	102	107

Table 3.2.: Shell population results from simulations for different screenings κ for a Yukawa ball with $N = 190$ particles in comparison to the shell population as determined in experiment. For a screening parameter $\kappa = 0.6$ the shell populations of the experiment [32] for all shells coincide with the ground state configuration in the simulation. From reference [80].

the experiment. Additionally, table 3.2 shows that, with increasing κ , particles move from the outer shell inward. For a screening parameter $0.58 \leq \kappa \leq 0.63$ the simulations yield exactly the same shell configuration as the experiment. Therefore, screening may be a possible explanation for the difference in the shell populations.

Other reasons for the difference in the shell populations can be charge fluctuations on the dust particles, friction of the neutral gas, temperature effects and more complicated effects that are not included in the model that is studied here, like wake field effects. Charge fluctuations due to field effects, ion winds and different sizes of the particles have been analyzed with MD simulations of ground state configurations [83]. The particles have a constant charge during the simulation but the initial charges are Gaussian distributed

$$f(q_i) = \frac{1}{\sigma_q(2\pi)^{1/2}} \cdot \exp\left(\frac{-(q_i - q_0)^2}{2\sigma_q^2}\right), \quad (3.11)$$

where q_0 is the mean charge and σ_q the width of the charge distribution. Figure 3.4 shows the number of particles on the shells N_S in dependence of the total charge variance σ_q for three different clusters ($N = 100, 190, 314$). Even for charge fluctuations of more than 20% no considerable effect on the shell populations of the ground state configuration can be seen.

The effect of friction on the shell populations of the Yukawa balls is under current investigation [84]. The experiments are performed in the overdamped regime and therefore the observed configurations can possibly crystallize in a metastable state and will not reach the ground state due to potential barriers that are too high to be overcome by thermal movement. Although this can be

3. Yukawa balls

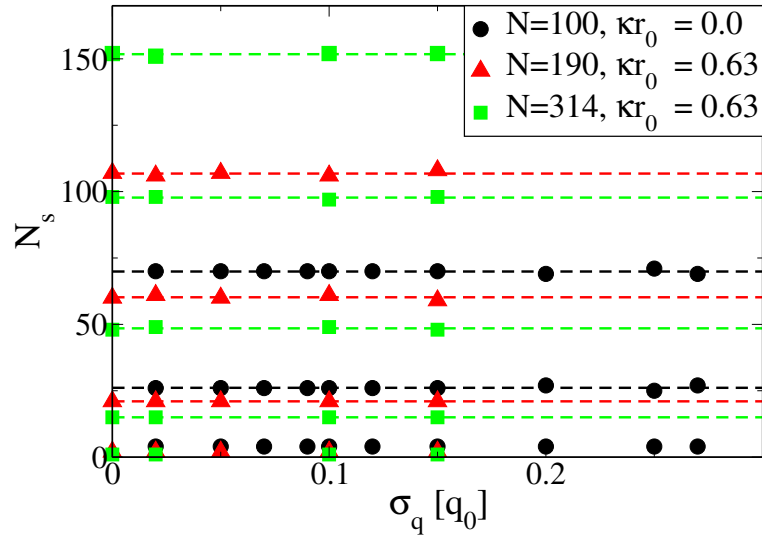


Figure 3.4.: Number of particles on the shells N_S versus the total charge variance σ_q for the clusters with $N = 100$ (black circles), $N = 190$ (red triangles) and $N = 314$ (green squares) particles. There is no significant change in the number of particles on the shells in the range of charge variance tested here. The lines correspond to the average number of particles on the shells over all calculated σ_q and are a guide for the eye. From reference [83].

an important effect it is not investigated here.

3.2.2. Comparison with experiments

The experiments are done at finite temperatures ($\approx 400K$) and therefore it may be questionable to compare ground state configurations found in simulations with the actual configurations observed in experiments. Therefore, Monte Carlo simulations at fixed temperatures were performed. The particles were initialized at random positions and after some initial time (Monte Carlo steps) to reach the thermal equilibrium the occupation numbers of the shells were recorded during the simulation. The averages of these shell populations for each fixed temperature are given in figure 3.5 in different colored lines. Here, clusters with $N = 2$ to $N = 100$ particles were considered with a screening parameter of $\kappa = 0.67$. Compared to the change of the occupation numbers between Coulomb ($\kappa = 0.0$, black lines) and Yukawa ($\kappa = 0.67$, colored lines) interaction the deviations are small in the considered range of temperature. Given in the

3.2. Structural properties

legend of that figure is the Coulomb coupling parameter

$$\Gamma_C = \frac{q^2}{a} \cdot \frac{1}{k_B T}, \quad (3.12)$$

which translates into $1/T$, where the temperature is measured in the units of the equilibrium two particle energy (3.4). The considered Coulomb coupling parameters have been higher or close to the value of the liquid-solid phase transition and therefore the clusters in the simulations can be considered crystallized. The deviations, best seen for the innermost shell population, have the same tendency as the screening, with increase of the temperature (screening) the shell population of the outer shell decreases, while the inner shell populations increase. But the effect of the temperature in the range of the experiments is much smaller than the effect of the screening. Further effects of the temperature will be discussed in section 3.3.

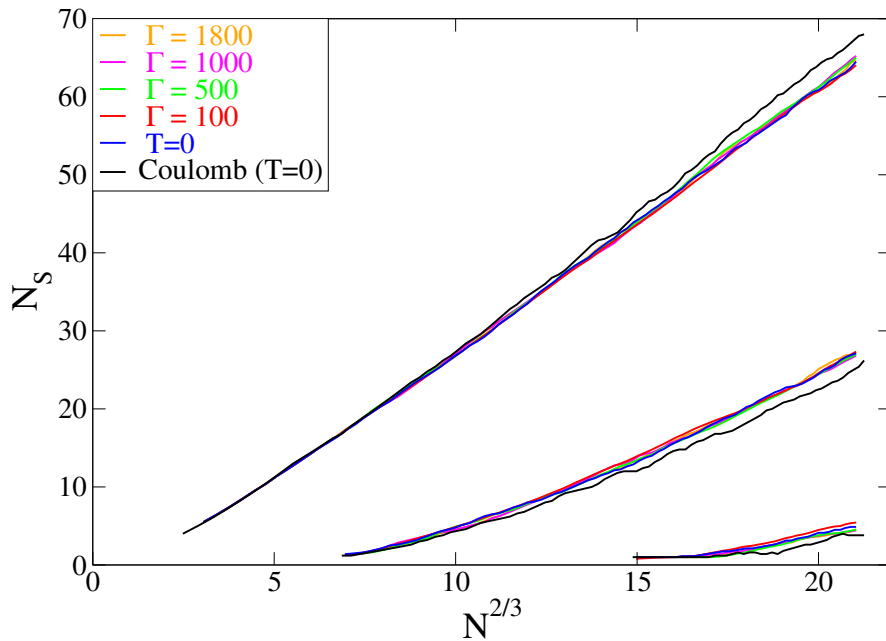


Figure 3.5.: The average shell population N_S as a function of systems size $N^{2/3}$. The shell population has been averaged over the MC simulation for fixed temperatures $\Gamma_C = \infty, 1800, 1000, 500, 100$ and fixed screening $\kappa = 0.67$. The deviations from the ground state configurations ($\Gamma = \infty, T = 0$) are small compared to the change in the occupation numbers between Coulomb and Yukawa ($\kappa = 0.67$) interaction. From references [83, 85].

This leaves the screening parameter κ as the most influential parameter on the

3. Yukawa balls

shell population. To investigate this in more detail, the comparison between experimentally observed clusters and simulation results was extended to 43 Yukawa balls [80]. The Yukawa balls were observed under the exact same plasma conditions (same plasma parameters) in the experiment. All clusters have been spherical symmetric and their diameter had been in the range $d = 4 - 5\text{mm}$. Therefore, the screening parameter is considered to be the same for all observations. The result is shown in the figures 3.6 and 3.7.

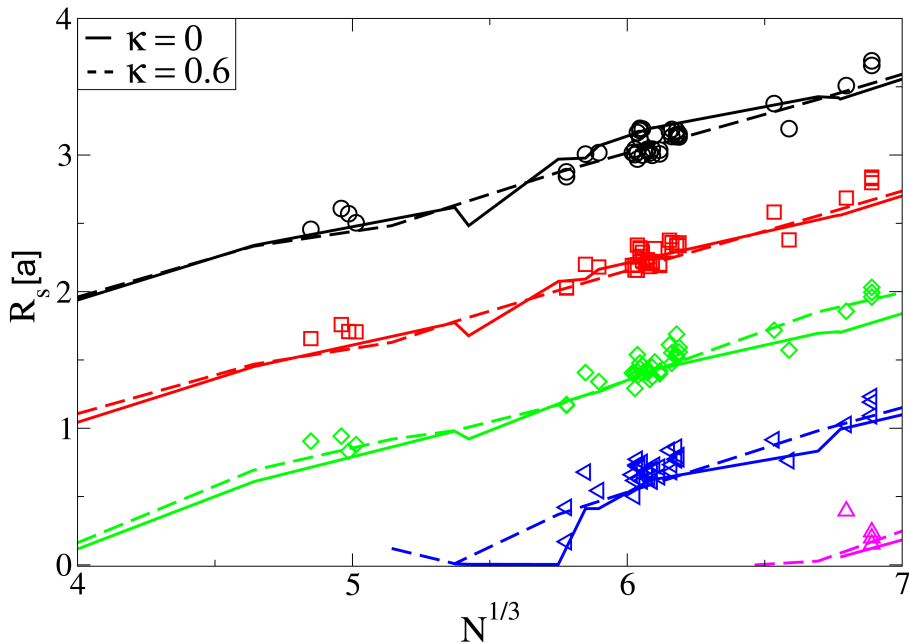


Figure 3.6.: Experimental (symbols) and simulation (lines) results for the shell radii R_S of Yukawa balls in units of the mean interparticle distance a . The different symbols denote the different shells. The dashed line are simulation results for a screening of $\kappa = 0.6$. From reference [80].

Figure 3.6 shows the shell radii of the experimentally observed clusters (symbols) and compares them with the shell radii found in simulations (lines) with Coulomb and Yukawa ($\kappa = 0.6$) interaction. From this comparison it is clear that the shell radii R_S in units of the mean interparticle distance, or Wigner-Seitz radius,

$$a = \left(\frac{3}{4\pi n} \right)^{1/3} \quad (3.13)$$

do not change much with screening. Here, n is the number density. The shell occupation numbers are much more sensitive to the screening.

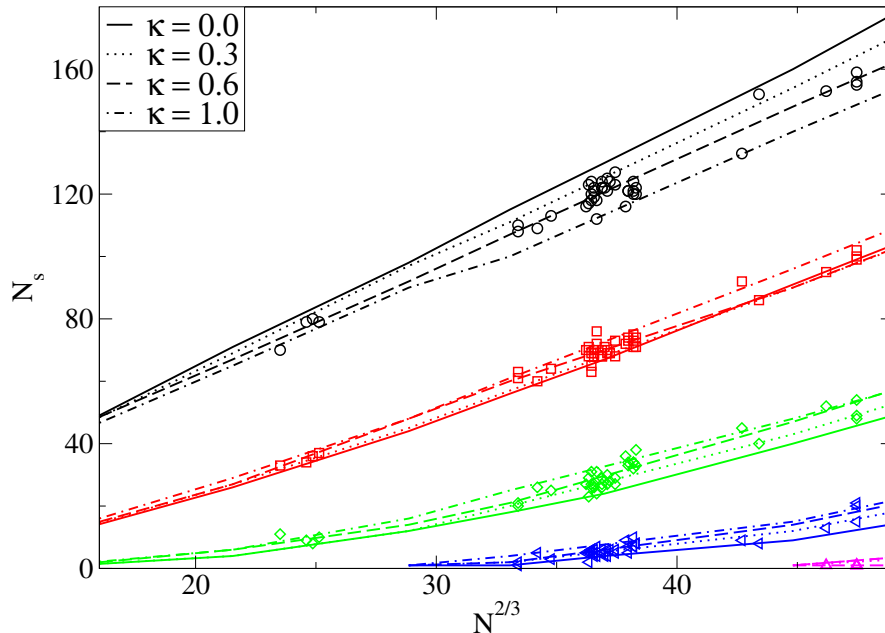


Figure 3.7.: Dependence of the shell population N_S on the screening parameter κ as a function of the system size $N^{2/3}$. The simulation results (lines) show that the particles are redistributed from the outer shell to inner shells with increased screening. The symbols denote the shell occupation numbers observed for the 43 Yukawa balls in the experiment at the same plasma conditions. From reference [80].

Figure 3.7 displays the shell populations N_S of the ground states for different screenings $\kappa = 0.0, 0.3, 0.6, 1.0$ in the simulations (lines) and the observed occupation numbers for the different Yukawa balls observed in the experiment. It reveals an almost linear behavior of the populations of all shells for all screenings as a function of $N^{2/3}$. However, the experimentally obtained population of the outermost shell is significantly smaller than the one of a Coulomb system (solid line), whereas the inner shells show a systematically higher population. Interestingly, the Yukawa simulations (dashed lines) show the same systematic deviation from the Coulomb case. With increasing κ particles move from the outer shell to inner shells. Hence, the finding discussed for the Yukawa balls with $N = 190$ particles hold also generally. It is also found, that the outermost shell exhibits the largest absolute change with κ and is therefore best suited for a detailed comparison with the experimental data. From a least square fit with a linear function of $N^{2/3}$ to the experimental data a screening parameter $\kappa_{exp.} = 0.62 \pm 0.23$ is found. In order to compare this value with the screening parameter in the simulations in units of $1/r_{0C}$ it has to be multiplied with

3. Yukawa balls

the factor that relates the mean interparticle distance a with the two particle Coulomb equilibrium distance r_{0C} , which again depends on the total number of particles, as seen in figure 3.8. If it is roughly approximated as 1.4 for all number of particles this leads to a screening parameter range $0.55 \leq \kappa_{sim.} \leq 1.19$. Further comparison of simulation results to the experimental observations will be found in section 3.4.

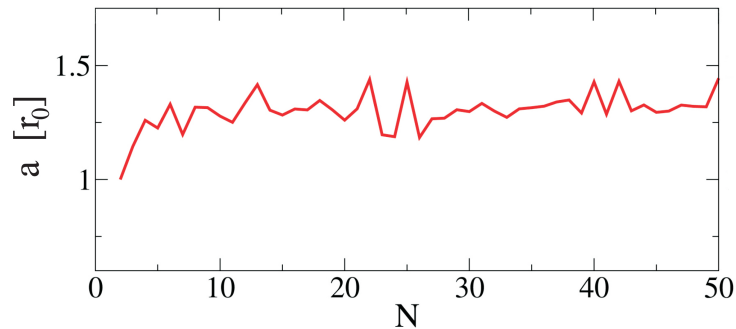


Figure 3.8.: Mean interparticle distance a of neighboring particles versus the total particle number N . The fluctuations indicate the error when replacing the two particle Coulomb equilibrium distance r_{0C} by the mean interparticle distance a , for example in the definition of Γ_C in eq. (3.12).

3.2.3. Ground states of strongly screened mesoscopic Yukawa balls

The general trends that come with the increase of the screening κ are clearly the decrease of the total diameter of the Yukawa ball and the increase of the inner shell populations due to the decrease of the occupation number on the outer shell. Nevertheless, a thorough analysis of the ground states for Yukawa balls was done. Mesoscopic systems with particle numbers from 11 to 60 and screenings from $\kappa = 0.0$ to $\kappa = 5.0$ were of special interest. Small Yukawa balls are experimentally easier to observe in detail, since normally no particles are overlapping each other in the focus of the CCD camera. The screening parameter in the simulation was changed in steps of $\Delta\kappa = 0.1$. When for some N a configuration change at some critical κ was detected, the calculation around this point was repeated with a substantially smaller κ step to ensure an accuracy of ± 0.05 in the critical κ at points of structural transitions from one configuration to another. Additionally it is of theoretical interest what will be the asymptotic shell configuration in the limit of a very short range interaction. To this end, the ground state at $\kappa = 20.0$ was also investigated and structural

3.2. Structural properties

transitions between $\kappa = 5.0$ and $\kappa = 20.0$ were recorded.

A typical simulation result is shown in figure 3.9 where the total energy per particle for the cluster $N = 29$ in the range of $0.0 \leq \kappa \leq 5.0$ is plotted. As one can see the energy decreases rapidly with κ by approximately one order of magnitude, due to the reduction of the pair interaction strength. The same behavior is observed for other particle numbers, as shown for $N = 31$ in figure 3.10 and, for $N = 57$, in figure 3.11. Due to the exponential dependence on the distance one may wonder if the energy decrease with κ follows an exponential law as well as is the case in macroscopic one-component Yukawa plasmas, e.g. [63, 86].

The simplest fit for the ground state total energy per particle has the form

$$\frac{E_{GS}^f(\kappa, N)}{N} = E_1(N) \cdot e^{-r_1(N)\kappa} + E_0(N) \quad (3.14)$$

and uses three κ independent free parameters which are functions of the particle number. In the analyzed range of N this dependence is found to be close to $N^{2/3}$, for the two energies E_0 and E_1 , whereas the effective length r_1 in the exponent scales approximately as $N^{1/3}$. Using the exact results for the ground state energies per particle from the molecular dynamics simulations, the following best fit for the three coefficients is obtained:

$$E_0(N) = 0.015 + 0.12N^{2/3}, \quad (3.15a)$$

$$E_1(N) = -0.81 + 0.92N^{2/3}, \quad (3.15b)$$

$$r_1(N) = 0.51 + 0.19N^{1/3}. \quad (3.15c)$$

In the Coulomb limit this fit reduces to

$$\frac{E_{GS}^f(\kappa = 0, N)}{N} = E_0(N) + E_1(N) = -0.795 + 1.04N^{2/3}. \quad (3.16)$$

This fit is useful to understand the main trends in the analyzed parameter range and reproduces the simulation data within several percent. Some representative examples are given in table 3.3. Further improvements can be easily achieved using e.g. the numerical results of reference [63] or the analytical expressions of reference [88], but this is not of interest in the present analysis. The presented fit for ground state total energies E_{GS}^f is a continuous function of κ and does not immediately reveal possible changes of the shell configuration. In fact, in many cases there co-exist several stationary states (shell configurations), the

3. Yukawa balls

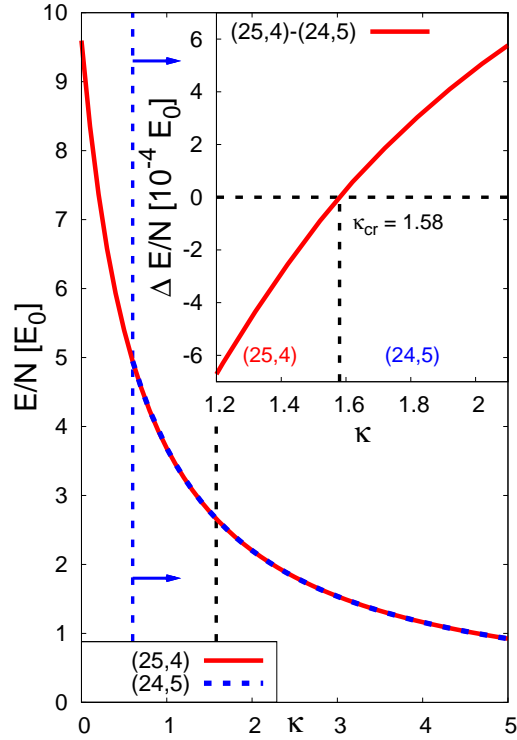


Figure 3.9.: Energy per particle of a Yukawa cluster with $N = 29$ particles for screenings $0.0 \leq \kappa \leq 5.0$. The red solid [blue dashed] line indicates the configuration (25, 4), [the configuration (24, 5)]. The vertical blue dashed line denotes the screening from which the configuration (24, 5) begins to occur in the simulations. The configuration (25, 4) is present in the complete range of screening. The inset shows the energy difference per particle of these two configurations in a small range of screening parameters around the critical value, where the ground state shell configuration changes from (25, 4) to (24, 5). The critical value is indicated by the vertical black dashed line in the inset. From reference [87].

energies of which may become equal at a certain value of κ . At this point a structural transition of the ground state is observed. This can be seen in figure 3.9 for the cluster with $N = 29$ particles. For small κ the configuration (25, 4) is the ground state until at the critical value of $\kappa_{cr} = 1.58$ the configuration (24, 5) has the same energy and a smaller energy beyond this point, see inset of figure 3.9. Thus, if κ crosses κ_{cr} from below, one particle of the cluster moves from the outer to the inner shell. This ground state change is accompanied by a jump of the derivative of the exact ground state energy $dE_{GS}/d\kappa$ at κ_{cr} , so this structural transition resembles a first order phase transition.

3.2. Structural properties

N	κ	E_{GS}/N (MD)	E_{GS}^f/N [Eq. (3.16)]	$\Delta(\%)$
12	0.0	4.839	4.656	-3.8
12	4.0	0.685	0.736	+7.4
58	0.0	15.875	14.788	-6.8
58	4.0	1.692	1.902	+12.4

Table 3.3.: Ground state energies per particle from equation (3.15a), compared to the exact results from MC simulations, and the relative error Δ , for some examples.

Figure 3.10 shows a more complicated example with two ground state changes occurring in a small range of screening parameters. For $\kappa < 1.5623$ the ground state configuration is $(27, 4)$ whereas at $\kappa_{cr1} = 1.5623$ the configuration $(26, 5)$ becomes the ground state. Finally, at $\kappa_{cr2} = 1.6142$ this configuration is replaced by $(25, 6)$ which remains the ground state for larger κ . This behavior can be seen in the energy differences plotted in the inset of figure 3.10. Around the interval $[\kappa_{cr1}, \kappa_{cr2}]$ all three states co-exist and have very close energies which illustrates the high accuracy and fine κ -grid required in this analysis.

These two examples are typical for most cases: at small κ the cluster structure is strongly influenced by the spherical trap. In contrast, in the limit of very large screening the pair interaction tends to a hard sphere interaction and the clusters approach a closed packed structure. This is often a layered structure allowing for an optimal compression [83] and makes it difficult to determine shells. In between the two limits of long range and short range interaction the shell configurations change via one or several structural transitions where one particle from the outer shell moves to the inner shell as this configuration becomes energetically favorable.

There are, however, several interesting exceptions to this general behavior. We observe three kinds of “anomalies” which will be analyzed in the following.

Anomalies of first kind: Correlated two-particle transitions

The cluster with $N = 57$ particles, as seen in figure 3.11 is of special interest because of its anomalous behavior in its structural transitions. At small screening, the configuration $(45, 12)$ is the ground state until at $\kappa_{cr1} = 0.10$ one particle from the outer shell moves to the cluster center forming the configuration $(44, 12, 1)$. Thereby the second shell is not changed since it has a “closed shell” configuration with 12 particles. Besides this “normal” transition,

3. Yukawa balls

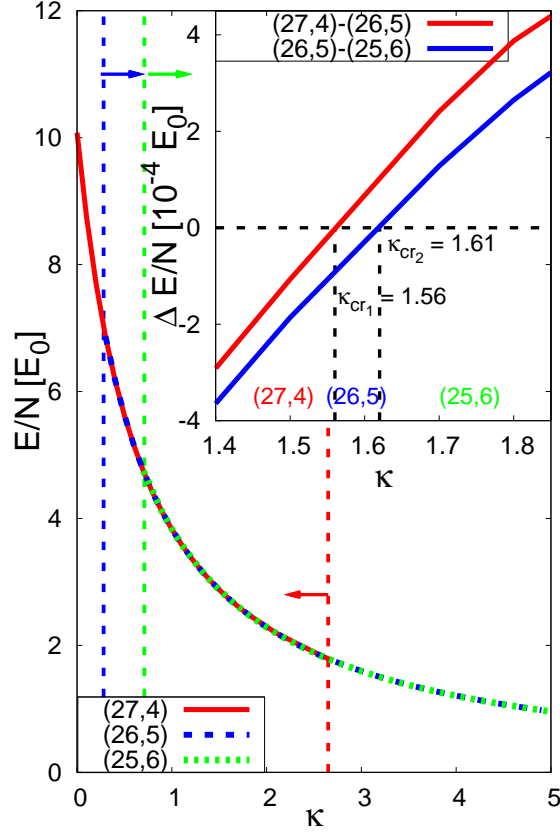


Figure 3.10.: Energy per particle of a Yukawa cluster with 31 particles for screenings $0.0 \leq \kappa \leq 5.0$. The red solid line indicates the configuration (27, 4) and the blue dashed [green dotted] line the configuration (26, 5) [(25, 6)]. The vertical dashed lines denote the beginning [blue for (26, 5) and green for (25, 6)] and the end [red for (27, 4)] of occurrence of these configurations in the simulations. The inset shows the energy difference per particle for two stable states the red [blue] solid line for the configurations (27, 4) – (26, 5) [(26, 5) – (25, 6)] around the critical value of screening. The critical values for the changes in the ground state configurations are indicated by the vertical black dashed lines in the inset. From reference [87].

at $\kappa_{cr2} = 1.04$ a new type of structural change is observed: The configuration changes according to $(44, 12, 1) \rightarrow (42, 14, 1)$. This means, at this point a correlated inter-shell transition of two particles is observed. This unusual behavior will be called “anomaly of first kind”. The reason of this anomaly is the particularly high stability of the closed shell configuration of the second shell which dominates the structure up to rather large screening. In contrast, a configuration with 13 particles on the second shell is energetically very unfavor-

3.2. Structural properties

able, although it exists in a broad range of κ values, in fact, the configuration (45, 13, 1) is never the ground state as can be seen in the inset of figure 3.11.

The first occurrence of an anomaly of the first kind is at $N = 30$ where a transition (26, 4) \rightarrow (24, 6) is observed at $\kappa \approx 1.5$. There is a total of 18 occurrences of such anomalies within the considered range of $N = 11, \dots, 60$: at $N = 30, 34, 36, 38, 40, 45 - 54, 57, 58, 60$. The reason for this behavior is, M that in all cases but for $N = 57, 58, 60$ the new ground state configuration, e.g. (24, 6) at screening above $\kappa = 1.5$, always forms a platonic body on the inner shell. This is a highly symmetric configuration which obviously decreases the energy per particle better than by just adding one particle [82, 89]. For the cases $N = 30, 34, 36, 38, 40$ the ground state configuration even change from one platonic body to another, while for the cases $N = 46 - 54$ the system changes from 10 particles on the inner shell to the closed shell configuration with 12 particles.

The only configuration with 11 particles on an inner shell is found for the case $N = 44$, at the very large screening value of $\kappa = 20.0$, which leads to the conclusion that this configuration is energetically unfavorable. In the other three cases, $N = 57, 58, 60$, the ground state configuration changes from (12, 1) to (14, 1) on the inner shells. Although a ground state configuration with (13, 1) particles in the cluster center is observed for some particle numbers in a certain range of screening parameters, the configurations (12, 1) and (14, 1) are far more often the ground state.

These anomalies are shown in the full ground state diagram 3.12, by the black circles (when moving upwards in the diagram). The complete list is also shown in appendix A.1 by the bold numbers.

Anomalies of the second kind: Reduction of inner shell population upon increase of N

Another kind of anomaly is seen, when considering changes of the total particle number N at constant screening (move right in the diagram 3.12). The “normal” trend upon an increase of the particle number by one is, of course, that the new particle is added to one of the existing shells (leaving the other shells unchanged) or moves into the center opening a new shell. However, again, one observes exceptions from this rule, cf. figure 3.9. This effect was also already observed for the Coulomb cluster ($\kappa = 0$) with $N = 59$ [82]. It has the ground state configuration (46, 12, 1). Addition of another particle to the cluster gives

3. Yukawa balls

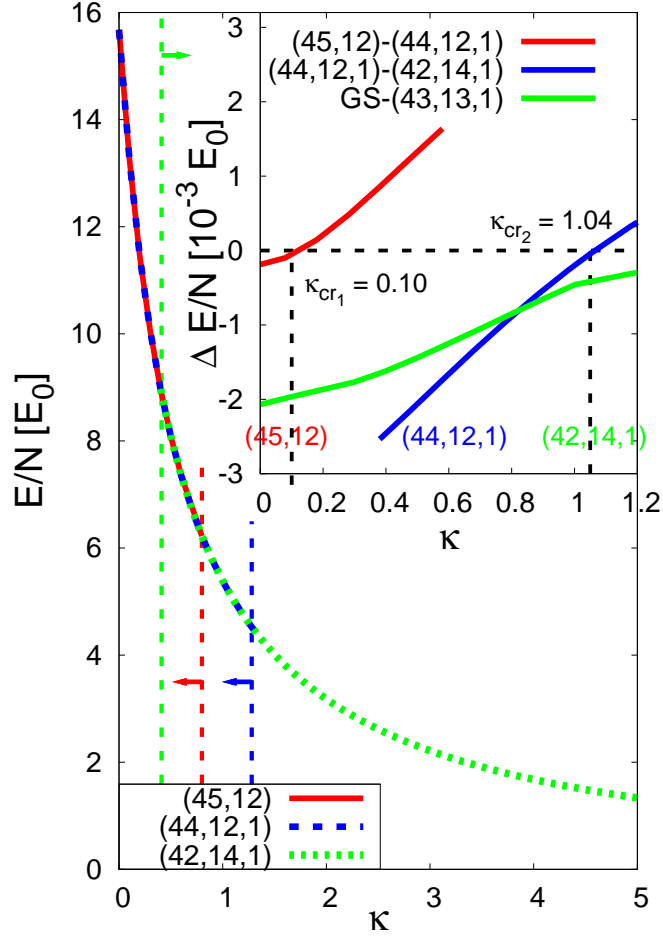


Figure 3.11.: Energy per particle of a Yukawa cluster with 57 particles for screenings $0.0 \leq \kappa \leq 5.0$. The red solid line indicates the configuration (45, 12) and the blue dashed [green dotted] line the configuration (44, 12, 1) [(42, 14, 1)]. The vertical dashed lines denote the beginning [green for (42, 14, 1)] and the end [red for (45, 12) and blue for (44, 12, 1), respectively] of occurrence of these configurations in the simulations. The inset shows the energy difference per particle: the red [blue] solid line for the configurations (45, 12) – (44, 12, 1) [(44, 12, 1) – (42, 14, 1)] around the critical range of screening. The green solid line is the energy difference of the metastable configuration (43, 13, 1) to the current ground state, this configuration is never the ground state. The critical values for the changes in the ground state configurations are indicated by the vertical black dashed lines. The change (44, 12, 1) \rightarrow (42, 14, 1) at $\kappa_{cr2} = 1.04$ shows an *anomaly of the first kind*. From reference [87].

3.2. Structural properties

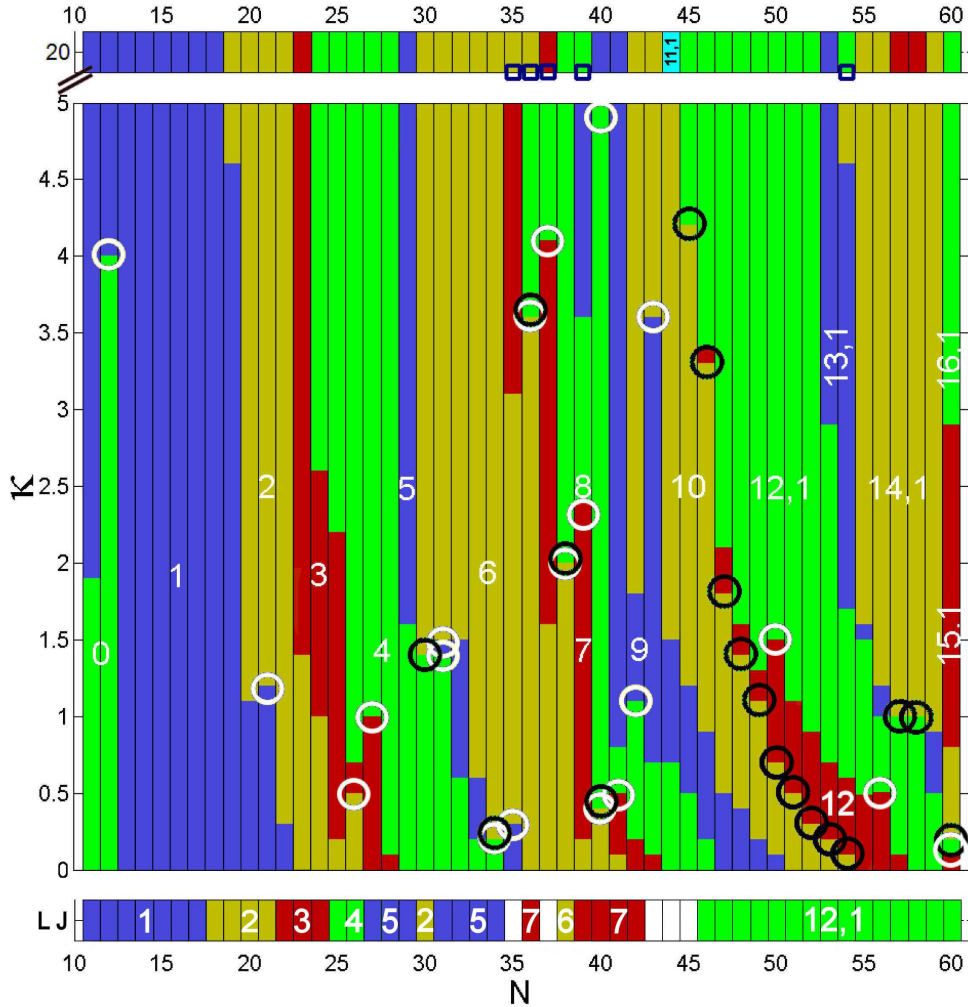


Figure 3.12.: Ground states of small ($11 \leq N \leq 60$) Yukawa balls for the range of screening parameter ($0.0 \leq \kappa \leq 5.0$). The numbers on the bars denote the number of particles on the inner shell(s). The black circles indicate anomalies of the 1st kind. The white circles indicate the end of the screening range, where anomalies of the 2nd kind appear. The ground states for a screening parameter $\kappa = 20.0$ are plotted above the diagram for comparison in what range the ground states at $\kappa = 5.0$ are stable. The cyan bar for $N = 44$ at $\kappa = 20.0$ refers to a ground state of (11, 1) in the center region; it is the only time this configuration is part of a ground state. The dark blue squares just below $\kappa = 20.0$ indicate anomalies of the 3rd kind, where a ground state configuration reappears with increased screening. Also for comparison the ground state configurations for Lennard Jones (LJ) interaction are plotted below the diagram, where possible. In the cases $N = 35, 37, 43 - 45$ it is not possible to define radial shells in the LJ-systems. From reference [87].

3. Yukawa balls

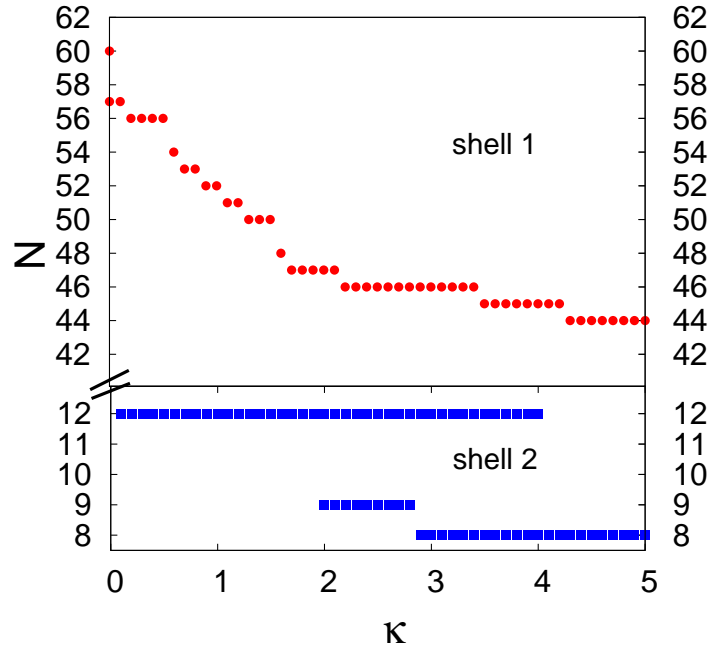


Figure 3.13.: Shell closures for the ground state configurations for the first two shells in the range of screening $0.0 \leq \kappa \leq 5.0$. The particle number N for the last closed shell is given by red dots [blue squares] for the shell 1 [2] in the considered range of screening. In some cases ($\kappa = 0$ [$2.0 \leq \kappa \leq 4.0$] for shell 1 [shell 2]) there exist different number of particles with closed shells, e.g. $N = 57$ and $N = 60$ for $\kappa = 0$. From reference [87].

rise to the configuration (48, 12). This is again a structural transition involving correlated behavior of two particles which will be called “anomaly of the second kind”. In this particular case this transition is even associated with a change of the number of shells: the three-shell configuration (first appearing at $N = 58$) disappears again and, instead, a two-shell configuration is restored. This is, of course, a consequence of the particular stability of the latter which contains two closed shells with 12 and 48 particles, respectively. The closed shell configurations are given in figure 3.13.

While, in Coulomb systems, $N = 59$ is the only known case of an anomaly of the second kind, in Yukawa clusters this behavior appears quite frequently. The first occurrence is at $N = 11$ for κ values between about 2 and 4. Here, addition of a particle gives rise to the configuration change $(10, 1) \rightarrow (12, 0)$, i.e. one

3.2. Structural properties

particle moves away from the inner shell (the shell vanishes), and the population of the outer shell increases by two. There is a total of 20 such anomalous transitions observed for 18 particle numbers: $N = 11, 20, 25, 26, 30, 33 - 42, 49, 55, 60$. There are two particle numbers where this effect occurs two times: for $N = 30 \rightarrow 31$, in the κ range $[1.5623, 1.6142]$ the configuration changes from $(24, 6)$ to $(26, 5)$. Interestingly, for screening parameters just below this range, i.e. $[1.4866, 1.5623]$ the inner shell loses even two particles, i.e. the transition $(24, 6) \rightarrow (27, 4)$ is observed. The second case where two such transitions occur is the transition $39 \rightarrow 40$. There for κ between 0.2223 and 0.4179 the ground state changes according to $(32, 7) \rightarrow (34, 6)$ whereas at $\kappa > 3.612$ the configuration change is $(31, 9) \rightarrow (32, 8)$.

Finally, anomalies of the second kind which are additionally associated with vanishing of one “shell”, i.e. removal of one particle from the cluster center, are found four times: for $N = 11 \rightarrow 12$ the transition $(10, 1) \rightarrow (12)$ is observed, cf. last paragraph. Return to a two shell configuration occurs three times: for $N = 49 \rightarrow 50$ the transition $(36, 12, 1) \rightarrow (38, 12)$, for $N = 55 \rightarrow 56$, the transition $(42, 12, 1) \rightarrow (44, 12)$ and, for $N = 59 \rightarrow 60$, the transition $(46, 12, 1) \rightarrow (48, 12)$ is found, which is known from the Coulomb case, cf. last paragraph, and appears here in a narrow range of small κ values. The complete set of these anomalies is given in appendix A.2.

Anomalies of the third kind: Reentrant shell transition upon increase of κ

Finally, there is a third kind of anomalous behavior which deviates from the “normal” shell filling trend of increased populations of the inner shells upon increase of κ at a constant N . This tendency is never violated in the considered range of particle numbers, $11 \leq N \leq 60$, and for $\kappa \leq 5$. Since $\kappa = 5$ corresponds to a pair interaction of very short-range one might expect that further increase of κ will not change the cluster structure qualitatively. To verify whether this is the case, for all N , additional calculations for an even larger screening, $\kappa = 20.0$, cf. figure 3.12, were performed. In most cases there is, indeed, no further change of the ground state configuration compared to $\kappa = 5$, as expected. For four particle numbers, $N = 40, 44, 57, 58$, the ground state configuration still changes in the “normal” way such that one particle is relocated from the outer shell to the inner shell.

However, there are six remarkable cases which violate this trend: $N = 35, 36, 37, 39, 54$ and $N = 44$. Consider first the total particle number $N = 44$.

3. Yukawa balls

This case is interesting, because it is the only case where the central configuration $(11, 1)$ is part of the ground state, apart from the cluster with 12 at screenings $\kappa \geq 4.1$. This arrangement does otherwise not occur because the clusters prefer the platonic body with 12 particles on the inner shell (closed shell configuration). Here the configuration $(31, 11, 1)$ becomes the ground state at $\kappa = 17.4$ and remains the ground state for larger screening.

In the other five cases, at $\kappa = 20.0$, several stationary states which differed only very little in their energies were observed. Therefore, MD simulations using separately each of these states as an input at $\kappa = 20.0$ were carried out and then the screening was slightly decreased, letting the system relax into a new stationary state, often with the same configuration and symmetry. This way, all metastable states were followed for certain and their energy dependence on κ could be recorded independently. The above five cases fall into two groups which differ with respect to the cluster symmetry. For the first, i.e. $N = 35, 36, 37, 39$, the cluster decreases the number of particles on the inner shell when the screening is increased between $\kappa = 5.0$ to 20.0 . The resulting new ground state configuration contains again a platonic body on the inner shell. Allowing for such a highly symmetric configuration here turns out to be energetically more favorable compared to the previous shell configuration or a simple increase of the number of particles on the inner shell.

Consider, for example, the cluster $N = 39$, cf. figure 3.14(d). Here, at $\kappa = 5$ the ground state is $(30, 9)$ until, at $\kappa_{cr} = 13.40$, the configuration $(31, 8)$ with one particle less on the inner shell becomes the ground state.

The particle number reduction on inner shells is sometimes accompanied by another trend: With increasing κ shells tend to split into subshells with close radii, as was already observed in references [83, 90]. This is observed e.g. for $N = 35$, cf. figure 3.14(a). Here the configuration $(28, 7)$ which is the ground state at $\kappa = 5$ has in fact two subshells each containing 14 particles which will be denoted as $([14, 14], 7)$. The radii of the two subshells differ only slightly, $R_{2,1} = 0.947$ and $R_{2,2} = 0.875$, respectively, while the inner shell radius is $R_1 = 0.426$, clearly distinguishable from the outer shell. At $\kappa_{cr} = 8.76$ we observe a transition $([14, 14], 7) \longrightarrow ([18, 11], 6)$, i.e. one particle from the inner shell moves outward and, in addition, three particles from the inner subshell move to the outer subshell.

Similar behavior is observed for $N = 36$, cf. figure 3.14(b). Here the

3.2. Structural properties

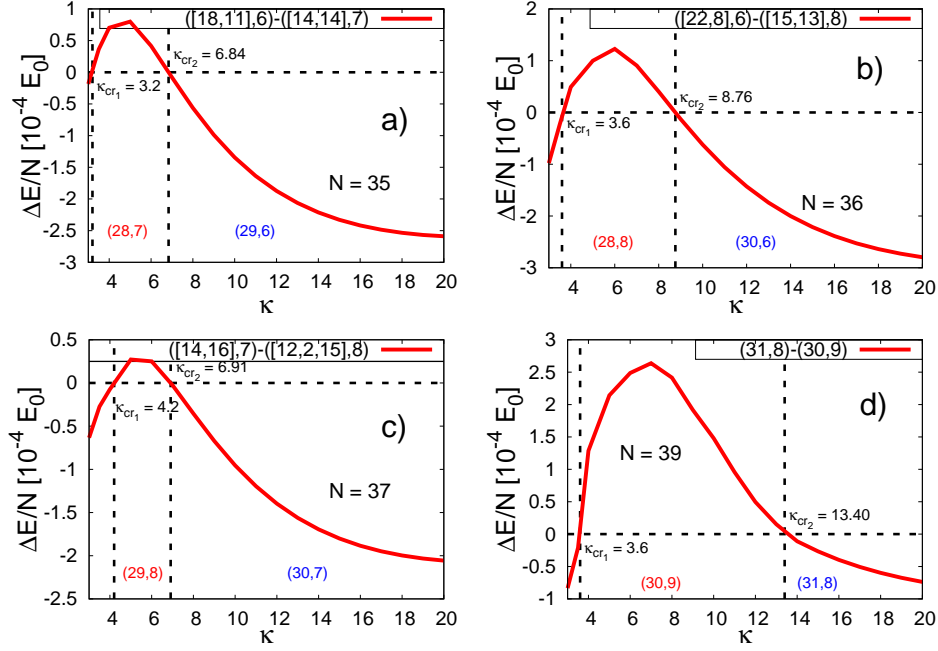


Figure 3.14.: Reentrant shell configuration changes for $N = 35$ (top left), $N = 36$ (top right), $N = 37$ (bottom left) and $N = 39$ (bottom right). When κ is increased, at κ_{cr1} one particle moves towards the center and, at κ_{cr2} , one particle returns to the outer shell restoring the former ground state configuration. The critical values of κ are indicated by the vertical dashed lines. The solid red line shows the energy difference of the two configurations which has two zeros. The legend shows the shell configurations, including the splitting of the outer shell into subshells, given by the numbers in square brackets. From reference [87].

configuration $([15, 13], 8)$ is the ground state at $\kappa = 5$. At $\kappa_{cr} = 6.84$ a transition $([15, 13], 8) \rightarrow ([22, 8], 6)$ is observed, where the inner shell loses two particles and, in addition, the inner subshell transfers 5 particles to the outer subshell. Analogously, for $N = 37$, cf. figure 3.14(c), the configuration $([12, 2, 15], 8)$ is the ground state at $\kappa = 5$. At $\kappa_{cr} = 6.91$ we observe a transition $([12, 2, 15], 8) \rightarrow ([14, 16], 7)$, where the inner shell loses one particle.

The cluster with $N = 54$ shows a similar behavior, cf. figure 3.15. Here, first the second shell population increases by one, at $\kappa_{cr1} = 5.04$, according to $(40, 13, 1) \rightarrow (39, 14, 1)$. Further increase of screening makes a third configuration more favorable which has even two particles less on the second shell: The configuration $(41, 12, 1)$ becomes the ground state again at $\kappa_{cr2} = 15.02$ which again is a consequence of the high symmetry (closed shell configuration).

3. Yukawa balls

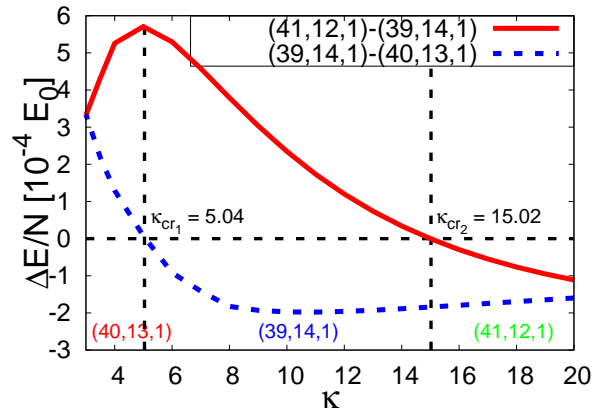


Figure 3.15.: The energy differences of all states, which become the ground state in the screening range $4.0 \leq \kappa \leq 20.0$ for the particle number $N = 54$. In this case increase of κ leads to a ground state with fewer particles on the second shell, returning to a ground state configuration, that already existed at lower screenings. In this case an “anomaly of the third kind” is observed. From reference [87].

Finally, particularly interesting behavior is observed for all mentioned $N = 35, 36, 37, 39, 54$, if a larger range of screening is considered, cf. figure 3.14 and figure 3.15. Here, for $\kappa \geq 1.7$, there are two states which become the ground state. At a first critical value κ_{cr1} one particle moves to the inner shell until at κ_{cr2} this transition is reversed. The only difference for $N = 54$ is that there is an additional ground state configuration between these two critical screenings. One particle moves outward and the original configuration with fewer particles on the inner shell is restored which remains the ground state for all larger values of κ . This contradiction to the general trend (of increasing the inner shell population with increased screening), together with the reappearance of a ground state configuration, will be called “anomaly of the third kind”. The complete set of these cases can be found in appendix A.3 with the exact critical screening parameters for the ground state configuration changes. The re-entrance of these ground state configurations at large screening are in all cases not different in their symmetries compared to the ground state configurations below κ_{cr1} , they have the same number of nearest neighbors and same shape of the Voronoi cells [91], with only their length scale strongly reduced due to the weaker interaction force.

In general, the restored ground state configurations consist of platonic bodies

3.2. Structural properties

on the inner shell, except for the case of $N = 37$. Here, the ground state configuration changes from $(30, 7)$ to $(29, 8)$ at a screening value of $\kappa = 4.2$ and back to $(30, 7)$ at a screening value of $\kappa = 6.91$. The 7 particles on the inner shell are not a platonic body and, as one can see from figure 3.12, it is not a common configuration compared to 6 or 8 particles in the center. Nevertheless, this can be understood by looking at the outer shell. The 30 particles are placed on the edges of an icosahedron which results in a highly symmetric configuration for the outer shell.

Experimentally interesting clusters

From figure 3.12, together with the estimated value of screening in the experiments $0.55 \leq \kappa_{sim.} \leq 1.19$ experimentally interesting clusters can be found. First, anomalies of the first kind, movement of two particles on the inner shell instead of one with increase of the screening, are possibly seen under experimental conditions for clusters with $N = 30, 48, 49, 50, 57, 58$ particles. Although anomalies of the second kind, increase of the inner shell population with increase of total particle number, might not be so interesting experimentally they might be observed for clusters with $N = 20/21, 25/26, 26/27, 30/31, 41/42, 49/50$. Since the adding of another particle is different in the experiment, it is not clear that anomalies of the 2nd kind are easily observed. Last it might be interesting to look closer at clusters that have a structural transition within the range of screening in the experiment since one might observe phase transitions here, but this will be discussed in more detail in section 3.4.

3.2.4. Improved models

Apart from analyzing the investigated model (3.1) by simulations in this work, it is also possible to derive other models, e.g. shell models or a macroscopic description. Furthermore it is of interest to investigate the different forces in the experiment that allow the simplified description of (3.1) in more detail. These approaches and their main results are briefly discussed here.

Confinement

The Hamiltonian (3.1) includes an external confinement potential that only depends on the parameter α , the strength of the confinement potential. As described in section 2.1 this confinement is resulting from the superposition of the thermophoretic force (2.4), the electrostatic forces of the rf-field and surrounding cuvette (2.5), gravity (2.1) and a possible ion-drag force although the

3. Yukawa balls

last has been found to play no role in the experimental setup. Psakhie et al. have implemented these different forces [92] in detail, depending only on the size and therefore the mass and surface charges of the dust particles. In this model it is possible to study the configurations in the presence of two different species. Under zero-gravity conditions these species separate, the smaller particles are on the outer shells and the larger particles on the inner shells. In the presence of gravity these two species not only separate within one Yukawa ball but even form two distinct Yukawa balls, often severely deformed. Despite these differences, the results of this model for equal masses backed the results of this work up.

Interaction

The model (3.1) also includes a static screening, condensed in the parameter κ which is the inverse Debye length λ_D in units of the two-particle Coulomb equilibrium distance r_0 . In reality kappa then depends on the temperatures and densities of the different species, electrons, ions and the dust particles. Therefore, for Monte Carlo simulations for each temperature of the heat bath or temperature of the dust particles there should be a self-consistent parameter

$$\kappa = \frac{1}{\lambda} = \sum_{\alpha} \left(\frac{e^2 n_{\alpha}}{\epsilon_0 k_B T_{\alpha}} \right), \quad (3.17)$$

which can be calculated by solving the Poisson equation $[\Delta - \lambda^2]u(\vec{r}) = -f(\vec{r})$, where λ is the Debye shielding length and α is the index for the species. This can be achieved by particle in cell (PIC) simulations. However, although the most advanced PIC simulations can take the time dependence of the discharge into account [93], only a very small number of dust particles in the plasma environment can be treated. Also, a simplified model which treats the streaming electrons and ions within linear response and computes the dynamically screened potential of the dust particles was developed [94]. These simulations yield an anisotropic and non-monotonic (wake) potential around the dust grain if the ion streaming velocity exceeds the sound speed which is normally the case in the plasma sheath. At the same time, simulations for the conditions of Yukawa balls which are produced in the plasma bulk revealed that there the streaming velocities are much lower [57]. Therefore, the static screening of the model (3.1) is justified. The idea of dynamically screened interaction is nevertheless followed in future work [95], which might have interesting effects on the formation and configuration of Yukawa balls but definitely on other dusty plasma experiments. It could also explain the attractive part of the interaction

potential measured in other experiments on Yukawa balls [96].

Ground state configurations

For ground state configurations of three or more particles the Hamiltonian (3.1) cannot be solved explicitly. But this is only true if the symmetry of the system is neglected. If one takes this into account, explicit solutions for the energies and vibrational force constants can be found for clusters with $N = 3 - 8$ Coulomb interacting ($\kappa = 0.0$) particles [88]. The found ground state configurations are an equilateral triangle ($N = 3$), a regular tetrahedron ($N = 4$), a regular octahedron ($N = 6$), bipyramidal geometries ($N = 5, 7$) and for the largest cluster ($N = 8$) that can be solved analytically a square antiprism. When eight points are distributed on the surface of a sphere with the aim of maximizing the distance between them in some sense, then the resulting shape corresponds to a square anti-prism rather than a cube. The given energies and vibrational force constants then only depend on the parameters of the ground state geometry, e.g. the edge length.

Shell models

For large particle numbers $N > 10000$ MD and MC simulations become costly in computing time and it is necessary to use other models to compute the ground state. Considering that the particles - at least for Coulomb interaction - are positioned on very well defined shells with small widths, this observation can be used to develop shell models. Here, the particles on a shell are not considered as distinct particles anymore. The particles on a shell are replaced by a uniform charge density on that shell and only the shells are interacting with each other. The first shell model for Yukawa balls [81]

$$E = \sum_{\nu=1}^L \left(\frac{N_{\nu}}{NR_{\nu}} \frac{N_{\nu}}{2} + \frac{1}{2N} N_{\nu} R_{\nu}^2 + \sum_{\mu < \nu} \frac{N_{\mu} N_{\nu}}{NR_{\nu}} \right) \quad (3.18)$$

had some flaws besides only be able to treat Coulomb interacting particles. Here, ν and μ denote the shell numbers, R_{ν} is the radius of shell ν and N_{ν} the number of particles on that shell. The second term in the outer summation is the confinement and the third term is the interaction of a shell with all inner shells. The interaction with outer shells is assumed to be zero, since the parts from different directions vanish in the summation over the angles. The first term though, is the important one. It includes the interaction of the particles on the same shell, but first it did not calculate the pairs correctly

3. Yukawa balls

and more importantly it neglected the fact, that there should be some space around each particle which cannot be used by other particles due to repulsion. Enhancements [97–99] finally lead to [63, 100]

$$E(N; \kappa) = \sum_{\nu=1}^L N_{\nu} \left\{ \Phi(R_{\nu}) + Q^2 \frac{e^{-\kappa R_{\nu}}}{R_{\nu}} \times \left(\frac{\sinh(\kappa R_{\nu})}{\kappa R_{\nu}} \frac{N_{\nu} - \epsilon_{\nu}(N, \kappa) \sqrt{N_{\nu}}}{2} + \zeta + \sum_{\mu < \nu} \frac{\sinh(\kappa R_{\mu})}{\kappa R_{\mu}} N_{\mu} \right) \right\}. \quad (3.19)$$

This model not only treats Yukawa interacting particles but enhances (3.18) by taking into account correlation effects by modifying the interacting pairs $N_{\nu} \rightarrow N_{\nu} - \epsilon_{\nu}(N, \kappa) \sqrt{N_{\nu}}$. The parameter $\epsilon(N, \kappa)$ was analyzed in detail [83] and found to be, for three values of κ ,

$$\begin{aligned} \epsilon(N, \kappa = 0.3) &= 0.891 \cdot N^{0.164}, \\ \epsilon(N, \kappa = 0.6) &= 0.957 \cdot N^{0.204}, \\ \epsilon(N, \kappa = 1.0) &= 1.001 \cdot N^{0.231}. \end{aligned} \quad (3.20)$$

For Coulomb interaction the correlation parameter $\epsilon(N, \kappa = 0.0)$ converged for large N to $\epsilon = 1.104$, a result which could be recently derived from the Thomson model [101, 102].

Macroscopic description

The idea, that the particles are not considered as individual particles but as some charge density, was used for a totally different approach to describe the many-particle behavior [100, 103]. Although a fluid-like statistical theory, where the particles are treated as a continuum, seems to be far from reality, it is able to achieve physical insight by the description of spatially averaged properties, e.g. the mean radial density profile. It is known that in a spherically symmetric parabolic potential particles interacting via the Coulomb potential establish a radially constant density profile, but the profile for a screened interaction was unknown. From the ground state energy ($p_i = 0, \forall i = 1, \dots, N$) of the Hamiltonian (3.1) as a functional of the density [100]

$$H_0[n] = E[n] = \int d^3r u(\mathbf{r}), \quad (3.21)$$

3.2. Structural properties

with the potential energy density

$$u(\mathbf{r}) = n(\mathbf{r}) \left\{ \Phi(\mathbf{r}) + \frac{N-1}{2N} \int d^3r_2 n(\mathbf{r}_2) \frac{q^2}{4\pi\epsilon|\mathbf{r}-\mathbf{r}_2|} e^{-\kappa|\mathbf{r}-\mathbf{r}_2|} \right\} + u_{corr}, \quad (3.22)$$

the radial density profile can be derived by minimization of the total energy E under the constraint $\int d^3r n(\mathbf{r}) = N = \text{const}$. The first term on the right hand side is the mean-field contribution with the confinement potential Φ , and u_{corr} denotes the density of the correlation energy. For a parabolic confinement, $\Phi(r) = \alpha/2r^2$, the ground state density profile is isotropic and parabolically decaying away from the trap center,

$$n(r) = \frac{\alpha N}{4\pi(N-1)q^2} \left(c - \frac{\kappa^2 r^2}{2} \right) \Theta(R-r), \quad c = 3 + \frac{R^2 \kappa^2}{2} \frac{3 + \kappa R}{1 + \kappa R}, \quad (3.23)$$

and the density drops to zero at a finite radius $R(N, \kappa)$ which follows from the normalization

$$-15 \frac{Q^2}{\alpha} (N-1) - 15 \frac{Q^2}{\alpha} \kappa (N-1) R + 15R^3 + 15\kappa R^4 + 6\kappa^2 R^5 + \kappa^3 R^6 = 0. \quad (3.24)$$

This equation only has one non-negative real solution for the radius R of the Yukawa ball. This density is equivalent to a local force balance [41, 100]. The derivation up to this point neglects correlation effects, which can be included by the application of the local density approximation (LDA) [103, 104], where the nonlocal terms within the energy density at point r are replaced by local expressions using the known energy density of the homogeneous system [63]. Figure 3.16 shows the density profiles derived from the mean field (MF) result (3.23) (solid lines) and compares them to the averaged shell densities of MD simulations (symbols). In the case of weak screening (a) the MF results agree perfectly with the exact MD results, while for increased screening discrepancies show up, especially in the trap center. For increased screening (b) the LDA approximation with correlations is very accurate, while this approximation fails to reproduce a good profile for weak and moderate screening $\kappa r_0 \geq 2.0$. This is due to the long range of the interaction which cannot be accounted for within a local approximation. An extension of these results to finite temperatures has been outlined in reference [105]. It is impressive that the MF model combined with the LDA in the case for large screening, if applied to the mesoscopic Yukawa balls, can give the correct radial density profile and size of the Yukawa balls. A more detailed discussion of this approach can be found in the thesis [106] and in [107].

3. Yukawa balls

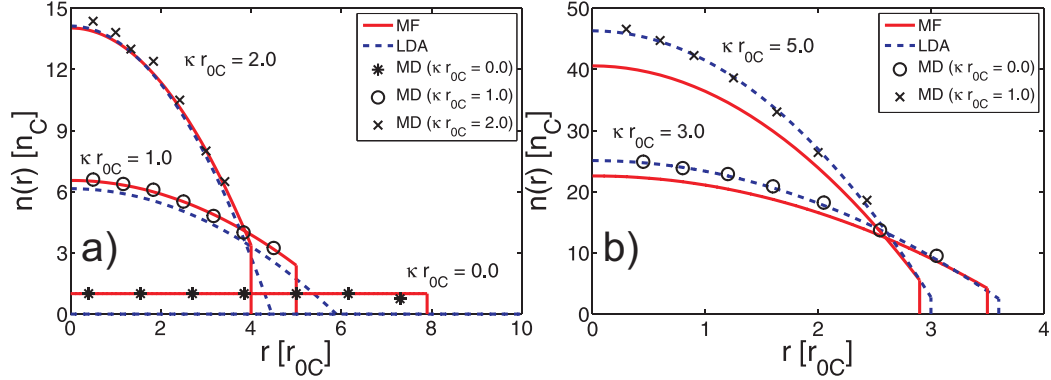


Figure 3.16.: Radial density profiles of a 3d plasma of $N = 1000$ particles calculated with the mean-field (MF) model (solid lines) and with the LDA including correlation contributions (dashed lines) for Coulomb and Yukawa interaction with four different screening parameters: $\kappa = 1, 2, 3$, and 5 . Averaged shell densities of MD simulations of a plasma crystal for the same parameters are shown by the symbols.

3.2.5. Potential barriers

It is interesting to have a closer look on the potential barriers in the Yukawa balls, since lower potential barriers would indicate a lower temperature for a phase transition. These barriers exist already at $T = 0$ temperature. Unfortunately the potential barriers between individual particles are not easily studied in the simulations without changing the system dramatically. For radial potential barriers though, the estimation is possible. Monte Carlo simulations were performed to calculate the radial potential barriers in these clusters by moving a particle of a known ground state configuration stepwise inwards (outwards). At each radial step the particle is fixed to that position, while all other particles are allowed to relax for 10^6 Monte Carlo steps at a finite temperature $T > 0$ after which the total energy of the system is calculated. Then the particle is again moved inwards (outwards) until it has reached the next shell. This procedure is repeated for each particle on each shell to include the effect that the radial potential barrier can be different for different particles since the starting position is different. Figure 3.17 shows the effect of different temperatures on the calculated barrier height. For the total particle number $N = 12$ and screening parameter $\kappa = 4.040$ the barrier was calculated for three different temperatures or coupling parameter $\Gamma_C = 500, 1000, 10000$, which are all within the solid-like regime of this cluster. The same analysis was performed for a wide range of particle numbers and screenings but the temperature of the heat bath for the

3.2. Structural properties

relaxation in the Monte Carlo simulation is found to have no effect on the calculated barrier height, it only adds to the total potential energy. This is seen as a constant shift for the different temperatures in the figure. Instead of the temperature the number of Monte Carlo steps for the relaxation is found to have an effect. In Figure 3.18 for all potential barriers and each radial step 10^5 MC steps at $\Gamma_C = 1000$ were used for relaxation in the cluster with $N = 31$ particles and a screening parameter $\kappa = 1.1$. The particles were moved inwards by $0.01r_0$ each step. The sharp drops or peaks in the barrier heights emerge from the simulation length and stepping size. The faster the particle is moved, by either picking a large step size or a small number of MC steps, the more likely the system does not relax into the configuration with the lowest energy. Nevertheless, these peaks might still have some physical meaning, because in reality the radial transition also occurs on a specific time scale, depending on the particle velocity and damping coefficient in the experiment. Therefore, for experimentally observed transitions there exist also a related simulation time that matches this transition. In the case of the kink in the radial transition (26, 5) to (27, 4) (blue line) in figure 3.18 that is indeed the case, cf. section 3.4.1 and figure 3.32.

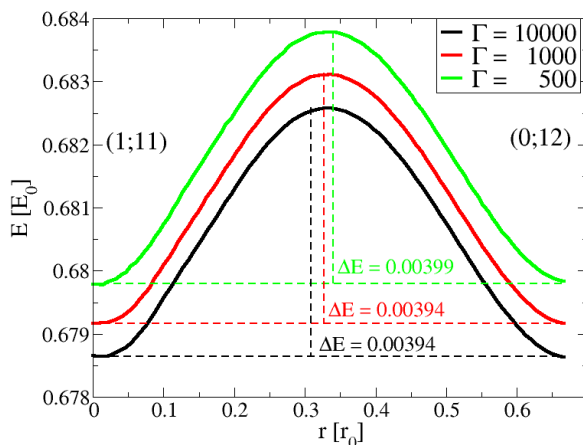


Figure 3.17.: Potential energy landscape measured by a Monte Carlo simulation where one particle is moved, while all other particles are allowed to relax into a new minimum energy configuration ($N = 12$, $\kappa = 4.040$). The curves show the potential barriers for the transition $(12,0) \rightarrow (11,1)$ for three different coupling parameters, $\Gamma_C = 10000, 1000$ and 500 , all in the solid-like regime. The computed barrier height does not depend on the temperature of the heat bath in the simulation.

3. Yukawa balls

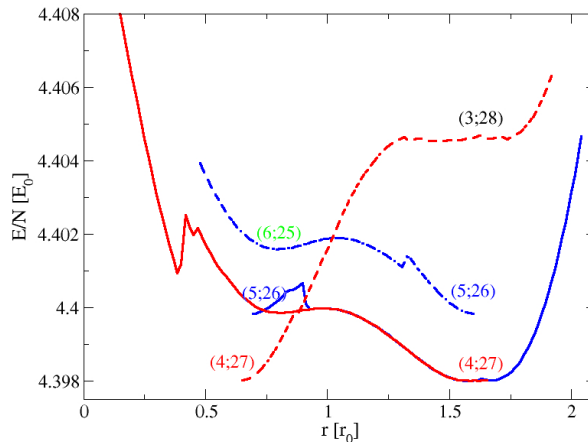


Figure 3.18.: Potential energy landscape for a Yukawa ball with $N = 31$ particles and a screening $\kappa = 1.1$. Curves show the potential barriers for three transitions $(27, 4) \rightarrow (26, 5)$ (solid line), $(26, 5) \rightarrow (25, 6)$ (dashed) and $(27, 4) \rightarrow (28, 3)$ (dashed). The peak in the solid curve around $0.75 < r_0 < 0.9$ occurs when the number of Monte Carlo steps is reduced simulating incomplete relaxation. Interestingly this peak matches the return point in the experiment, cf. figure 3.32 (a)

For the computation of the *radial minimum energy barrier* in the clusters given in the appendices B.1 for $(N = 31, \kappa = 0.0 \dots 4.0)$ and B.1 for $(N = 11 \dots 40, \kappa = [0.0, 1.0, 1.5, 4.0])$ a radial step of $0.01r_0$ and 10^6 MC steps were used. Only radial barriers from the ground state configuration were considered. In the example of figure 3.18 for $N = 31$ and $\kappa = 1.1$ the ground state configuration is $(27, 4)$ and only the transitions $(27, 4) \rightarrow (26, 5)$ and $(27, 4) \rightarrow (28, 3)$ (red lines) would be considered. The results for $N = 11 \dots 40$ particle numbers and screenings $\kappa = 0.1 \dots 5.0$ are given in figure 3.19. Since from this figure it is hard to distinguish differences, the energy barrier heights for the Yukawa ball with $N = 31$ particles and screening ranging from 0.0 to 5.0 are given in the first column of the table in appendix B.1. In figure 3.19 for some examples a low energy barrier height is found. For $N = 12, \kappa \approx 4.0$ or $N = 25, \kappa \approx 0.2$ the barrier height is much smaller than for screening above or below that value. Comparing this result with the ground state configurations from figure 3.12 it is found, that in this region also a structural transition from one ground state configuration to another occurs, e.g. $(12, 0)$ to $(11, 1)$ for $N = 12$ at $\kappa = 4.1$ and $(23, 2)$ to $(22, 3)$ for $N = 25$ at $\kappa = 0.3$.

Furthermore, figure 3.20 shows the dependence of the potential barrier height on the screening for the cluster with $N = 31$ particles. Comparing that re-

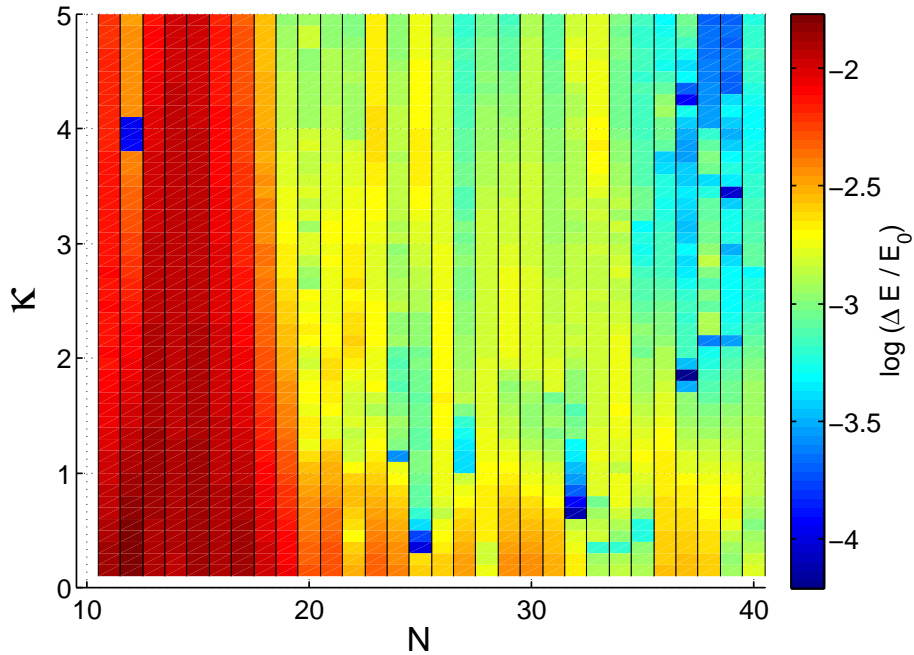


Figure 3.19.: Potential energy barrier height ΔE in logarithmic scale as a function of total particle number N and screening κ . Comparison with the ground state configurations in figure 3.12 yields that in the region of a structural transition between ground states the energy barrier height is also very low. This can best be seen for e.g. $N = 12$, $\kappa \approx 4.0$ or $N = 25$, $\kappa \approx 0.2$

sult with the ground state configurations in figure 3.12, the drop in the barrier height can easily be matched with the structural transition of the ground state configuration from $(27, 4)$ to $(26, 5)$ at $\kappa = 1.56$. Additionally figure 3.21 shows the dependence of the potential barrier height on the total particle number N for a fixed screening of $\kappa = 0.2$. The main peak corresponds to the cluster with $N = 12$ particles, forming a perfect dodecahedron. The cluster with $N = 13$ particles again forms a dodecahedron, but with an additional particle in the center. These structures are exceptionally stable against melting processes.

3. Yukawa balls

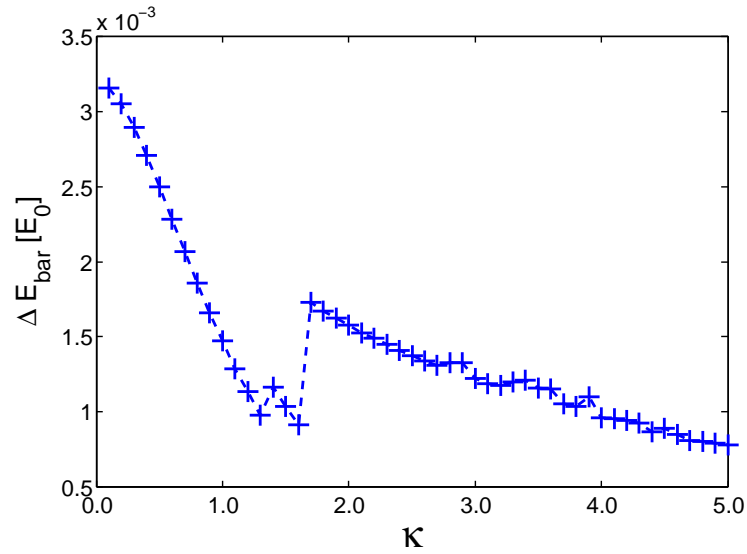


Figure 3.20.: Potential energy barrier height as a function of screening for a Yukawa ball with $N = 31$ particles. The drops at screenings around $\kappa = 1.5$ roughly correspond to the structural transitions of the ground state configurations at $\kappa = 1.56$ and 1.61 .

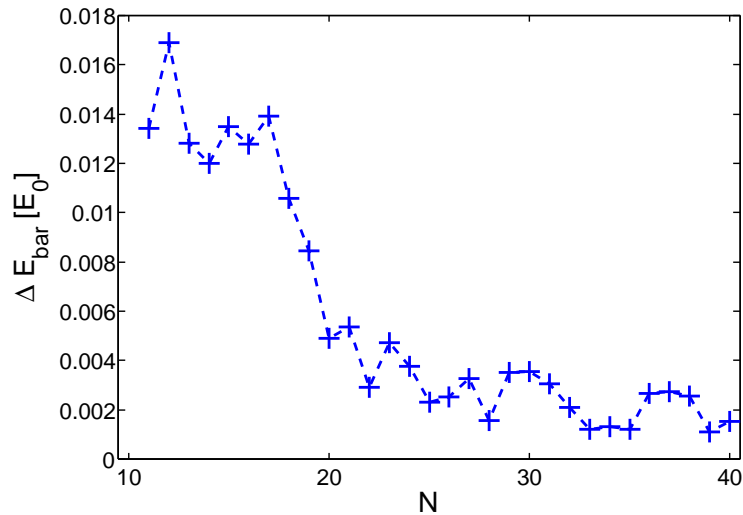


Figure 3.21.: Potential energy barrier height as a function of total particle number N for a fixed screening of $\kappa = 0.2$. The main peak corresponds to the cluster with $N = 12$ particles, forming a perfect dodecahedron. The dashed line is only a guide for the eye.

3.3. Thermodynamic properties

Finite thermal energy caused only occasional transitions between stationary states. This behavior is typical for matter at very strong coupling characterized by very low kinetic energy, typical for a Wigner crystal. This physical situation can be quantified by the Coulomb coupling parameter (3.12), which is the ratio of the mean interaction energy to kinetic energy. The transition from strong coupling where the system is in a crystalline state to a liquid occurs for infinite matter at critical value Γ_{crit} , which has been computed as 175 (137) in $3d$ ($2d$) [108], although this value changed constantly over the years, e.g. [109, 110].

Here we are concerned with systems with Yukawa interaction and have to generalize the coupling parameter. The straightforward way to do this would be to replace the Coulomb energy of a pair of particles by the mean Yukawa energy, which then leads to $\Gamma = e^{\kappa a} \Gamma_C$. Nevertheless, simulations [86] showed that with that replacement a phase diagram cannot be defined systematically. The reason is that the melting is driven by the excitation energy of particles which leads to increasing fluctuations of the particles around their stationary positions. These fluctuations are defined by the local curvature of the potential [80, 111], i.e. its second derivative in the minimum. This allows to define a proper effective Yukawa coupling parameter [112],

$$\Gamma(\kappa) = \Gamma_C \frac{e^{\kappa a}}{1 + \kappa a + (\kappa a)^2/3}, \quad (3.25)$$

which allows to qualitatively correctly predict the melting point $\Gamma_{crit}(\kappa)$ for any κ , based on the known critical value for an infinite Coulomb system.

However, for the analysis of melting in Yukawa balls one has to take into account the peculiarity of small systems. For finite systems melting is not defined as in a macroscopic system, there exists no strict phase transitions. Nevertheless, a similar transition or crossover from solid-like to liquid-like behavior is well known and has been studied as a function of particle number for Coulomb interaction [113]. In [113] it was shown, that the melting temperatures for smaller systems, where a bigger fraction of particles are at the boundary, are typically higher than in the macroscopic limit, e.g. $\Gamma_{crit} = 500$ for $N = 100$ particles. It is also known, that for smaller clusters the crossover proceeds over a finite range of temperatures, making it hard to identify a melting point. Figure 3.22 gives an example of this crossover and shows the relative distance fluctuations (3.33) as a function of temperature for a Yukawa ball with $N = 190$ particles and $\kappa = 0.67$. Although the transition point can be determined

3. Yukawa balls

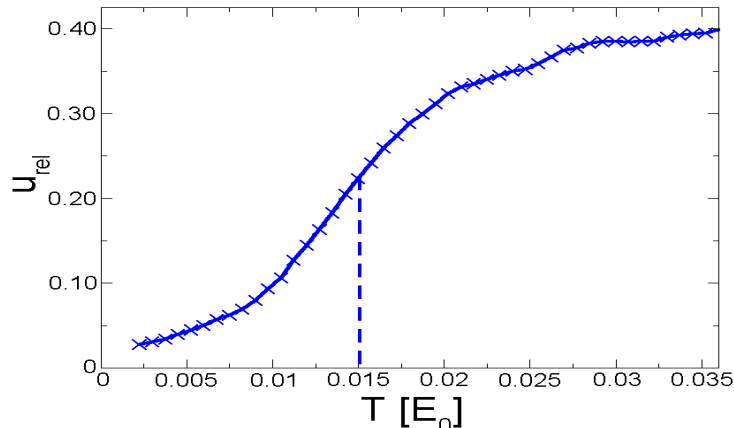


Figure 3.22.: Relative distance fluctuations u_{rel} as a function of temperature $k_B T$ for a Yukawa ball with $N = 190$, $\kappa = 0.67$. The increase in the relative distance fluctuations corresponds to the transition between the solid-like and liquid-like phase of that crystal.

as $T_m^{crit} \approx 0.015E_0$ by choosing the middle of the increase in u_{rel} , the phase transition occurs really in the region $0.01 \leq T_m^{crit} \leq 0.02$. Furthermore, finite systems are strongly influenced by the symmetry of the confinement potential and the structure of the Yukawa balls. This is also known from Lennard-Jones clusters, where the phase transitions are also strongly dependent on the particle number [114].

The effect of screening on the stability and melting of Yukawa balls was analyzed in reference [80, 85] where a simple analytical estimate can be observed for the example $N = 2$. Expanding the total potential energy to second order around the ground state, as in the macroscopic system, a formula analogous to (3.25) is obtained,

$$\Gamma(\kappa, N = 2) = \Gamma_C(N = 2) \frac{e^{\kappa r_{0Y}}}{1 + \kappa r_{0Y} + (\kappa r_{0Y})^2/2}. \quad (3.26)$$

Here, r_{0Y} is the two-particle equilibrium distance for Yukawa interaction (3.7), which also replaces the Wigner-Seitz radius a in Γ_C . As in the macroscopic case (3.25) screening destabilizes the crystal and the only difference is seen in the third term of the denominator.

3.3.1. Melting parameter

In order to compute the critical coupling parameter of a phase transition, sensitive parameters, that show peculiar behavior in the region of the phase tran-

3.3. Thermodynamic properties

sition, are required. There are several melting criteria that fit this description.

1. The short time self-diffusion is given by the Stokes-Einstein value

$$D_s = \frac{k_B T}{6\pi\eta R}, \quad (3.27)$$

where η is the viscosity of the solvent and R is the radius of the particle. The long time self-diffusion, where the diffusion occurs on a large time scale compared to the time needed to move over the distance of the particle radius R , can be defined by the Einstein relation

$$D_t = D = \lim_{t \rightarrow 0} \frac{1}{6t} \langle |\mathbf{r}_j(t) - \mathbf{r}_j(0)|^2 \rangle, \quad (3.28)$$

where $\mathbf{r}_j(t)$ is the time-dependent trajectory of particle j . This was studied also for infinite Yukawa systems [115], but it is claimed [116] that this criterion is only universal for Brownian dynamics, while in real fluids a simple scale is missing.

2. The ratio of the first maximum to the first minimum in the pair distribution function is sensitive to a phase transition, e.g. [117].
3. The specific heat capacity (specific heat) is mathematically defined as the ratio of a small amount of heat ∂Q added to the system, to the corresponding small increase in its temperature dT ,

$$C_V = \left(\frac{\partial Q}{\partial T} \right)_V. \quad (3.29)$$

The index V denotes the specific heat at constant volume. This parameter shows also for mesoscopic systems a kink at the point of the phase transition, although the characteristic of this kink depends heavily on the total particle number, which is known from studying melting temperatures of Gallium, Natrium and metal clusters [118–120].

4. The Lindemann-like criteria are parameters which detect fluctuations of single particles or pairs in a system. Lindemann argued [121] that the rigid lattice structure of a solid breaks down if the particle oscillations grow larger than a critical value. Additional energy pumped into the system then cannot be absorbed into further increased oscillations and must be transferred to particle translations.
5. The correlation time of the potential energy autocorrelation function (2.18) is sensitive to melting. The idea is similar to the velocity autocor-

3. Yukawa balls

relation function which leads to the diffusion coefficient. The correlation time of the potential energy autocorrelation function, or the number of MC steps in case of a MC simulation, is long in the solid regime, because the particles only fluctuate within their local potential and the resulting potential energy does not fluctuate much. In the liquid regime the particles are exchanged often between the lattice sites and therefore the correlation time is long too. In the transition region between the solid and liquid regime the correlation time is short. The particles fluctuate in their local potential but sometimes are able to perform particle translations as well. Therefore the fluctuations in the potential energy are small during the time when the particles fluctuate only in their local potential and large when the particles also perform exchanges.

This list shall not be considered as complete. Often there are further order parameters in different systems, e.g. the susceptibility in magnetic materials. Apart from the potential barrier heights, which can give a good estimate of the radial melting temperature as well, cf. section 3.2.5, here the following parameters were used:

The *specific heat* per particle C_v is defined by the temperature derivative of the average potential energy $\langle U \rangle$ and is also given by the mean square fluctuation as

$$C_V = \frac{1}{N} \frac{d}{dT} \langle U \rangle = \frac{\langle U^2 \rangle - \langle U \rangle^2}{Nk_B T^2}. \quad (3.30)$$

For the combinations of parameters N and κ listed in the appendices B.1 and B.2, we measure the specific heat by sampling at least 10^9 MC steps after the system attains thermal equilibrium. Confirming that the values obtained from both expressions are consistent, we adopt the latter values that are much more accurate as opposed to the former, which require the numerical derivative. With the specific heat it is possible to detect the two-stage melting process in the Yukawa balls [122, 123], as seen in figure 3.23 on the example of $N = 38$, $\kappa = 1.0$. An analogous two-stage melting process is known for $2d$ plasma crystals [124], where the two stages are intershell rotations and radial melting.

Corresponding to the two peaks in figure 3.23, figure 3.24 shows snapshots of the same system at different temperatures. First, in figure 3.24 (a) the particles are dislocated on the shell and the shells are rotating against each other. Then in figure 3.24 (b) the shell width is increasing, indicating that the particles are starting to fluctuate in radial direction as well, but are not yet able to overcome the radial potential energy barrier. In figure 3.24 (c) the particles are performing radial transitions as well and the radial melting starts and in

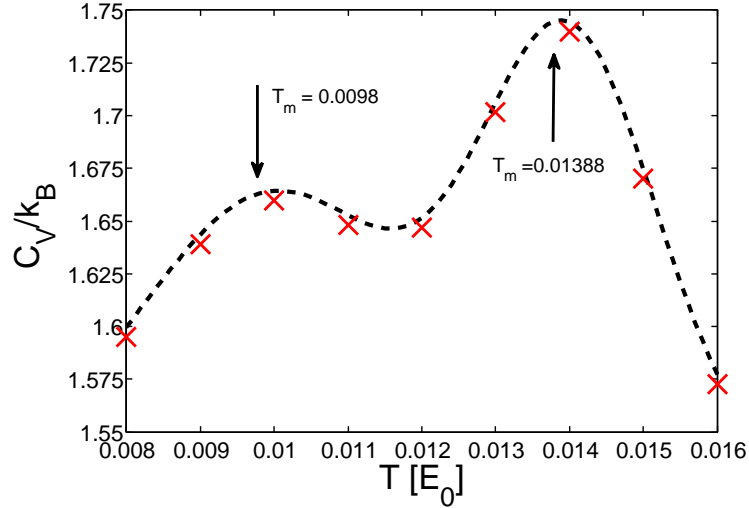


Figure 3.23.: Specific heat C_V as function of temperature T for a Yukawa ball of $N = 38$, $\kappa = 1.0$. The two peaks in the specific heat correspond with two kinds of melting, the first peak corresponds to intrashell melting and the second peak corresponds to intershell melting, cf. figure 3.24.

figure 3.24 (d) the cluster is radially melted. Therefore, it is obvious that the two melting processes correspond to intra-shell melting, where the local order on a shell is lost, and inter-shell melting, where the particles are able to move between the shells. Normally, the peak from the radial melting is at higher temperatures and better accentuated, which often makes it easier to detect. The metastable states with the same shell configuration are energetically much closer [84, 125] and are much easier to access. Unfortunately the potential energy barrier heights are not easily calculated because the path is unknown and no symmetry argument is possible as in the radial energy potential barrier case. The fine structure, metastable states with the same shell configurations, of the Yukawa balls has been analyzed in [78, 82, 125]. The computation of the Voronoi diagrams [91], which is necessary for the fine structure, is computationally expensive and has not been studied as a function of temperature here.

3. Yukawa balls

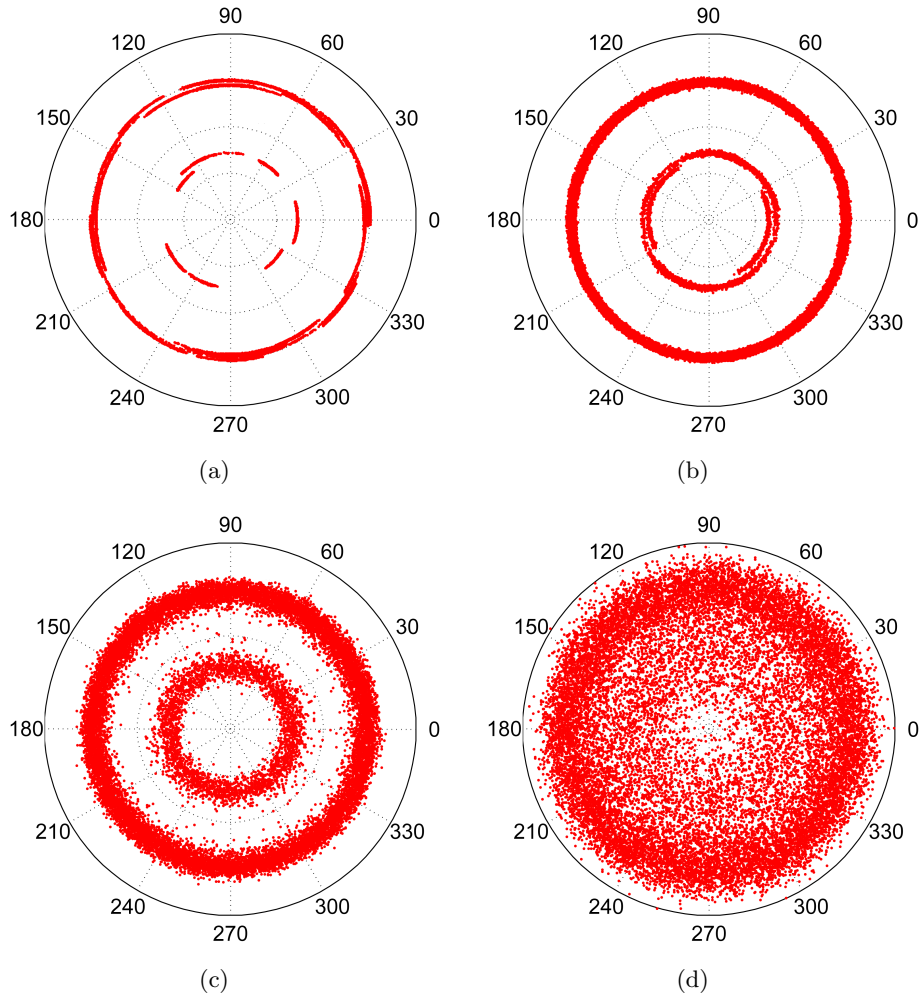


Figure 3.24.: Particle positions over several MC steps for a Yukawa ball with $N = 38$, $\kappa = 1.0$ projected onto the plane (ϕ, θ) . The different snapshots show the same cluster at different temperatures, ranging from low (a) to high (d) temperature, $T = 0.008$ (a), $T = 0.010$ (b), $T = 0.013$ (c) and $T = 0.016$ (d). In (a) and (b) the system is dislocated within the shells, while being stable radially and in (c) and (d) the system also melts radially.

As a second parameter, the relative frequency of occurrence of possible shell populations has been studied by MC simulations. This parameter can be compared with order parameters in lattices, where the defects in a lattice are analyzed. Here, the idea to detect metastable states is limited to such metastable states that are different in their shell population. This procedure has the huge advantage that relatively few MC steps, 10^6 , are enough to get a good estimate for the probability, that a specific shell population occurs during the MC simu-

3.3. Thermodynamic properties

lation at a fixed finite temperature. For each combination of N and κ listed in the appendices B.1 and B.2 10^7 MC steps were used to compute the probabilities for all possible shell populations. To determine a specific shell population the shell radii of the ground state configuration were used to compute the radii which separate two shells. Although the shell radii for metastable states are slightly different from the ground state configuration, this effect plays no role for the probability of occurrence $P_{conf.}$. For example, the radius, where the two shells of the cluster with $N = 31$, $\kappa = 1.1$ are separated, is $r_{s,gs} = 0.89234$ for the ground state $(27, 4)$ and $r_{s,ms} = 0.89211$ for the metastable state $(26, 5)$.

For the determination of the melting point, as given in the appendices B.1 and B.2, a fixed probability of 90% of the ground state configuration was used.

Figure 3.25 shows the probability of occurrence of all accessed configurations of a unscreened ($\kappa = 0.0$) Yukawa ball with $N = 27$ particles. The ground state configuration for that cluster is $(24, 3)$ and therefore this state has the highest probability at $T = 0$. With increasing temperature the frequency of occurrence of the ground state configuration drops below 40%. This raises the probability of other metastable states. While the configurations $(25, 2)$ and $(22, 5)$ have low probabilities, even for very high temperatures $\Gamma_C < 20$, the energetically lowest metastable state $(23, 4)$ increases the frequency of occurrence until, at $T > 0.033$, it is more probable to find this metastable configuration in the simulation than the ground state configuration. With the above definition of the melting temperature by the frequency of occurrence the critical temperature was found to be $T_m^{crit} = 0.00985$ for this cluster.

The melting point, determined by the frequency of occurrence, for a Yukawa ball with $N = 30$ particles, as seen in figure 3.26 shows the same dependence on the screening κ as other parameters. Here, the melting temperatures were computed as $T_m^{crit} = 0.00601$ at $\kappa = 1.4$ and $T_m^{crit} = 0.00273$ at $\kappa = 1.5$, while (cf. table in appendix B.2) the melting temperatures determined by the specific heat (3.30) and the variance of the block averaged relative distance fluctuations (3.35) show the same drop of about a factor of 3. The frequency of occurrence for $N = 30$, $\kappa = 1.5$ in figure 3.26 (b) shows very interesting behavior. The ground state configuration of $(24, 6)$ nearly vanishes at low temperatures $T > 0.005$ and then slowly increases its frequency. In a very small range of temperatures, $0.0035 \leq T \leq 0.008$, the metastable configuration $(26, 4)$ is the most probable configuration in the simulations. This configuration has been the ground state configuration for smaller screenings, cf. figure 3.26 (a). At higher temperatures then the metastable configuration $(25, 5)$ is the most probable configuration in the MC samples.

3. Yukawa balls

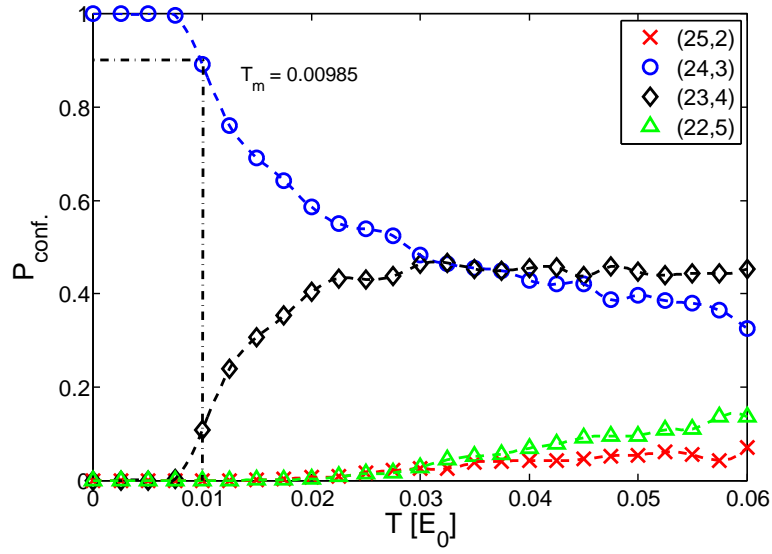


Figure 3.25.: Frequency of occurrence for all accessible configurations (ground state and metastable states) as a function of temperature for a cluster with $N = 27$, $\kappa = 0.0$.

The last example for the probability of occurrence is for the cluster with

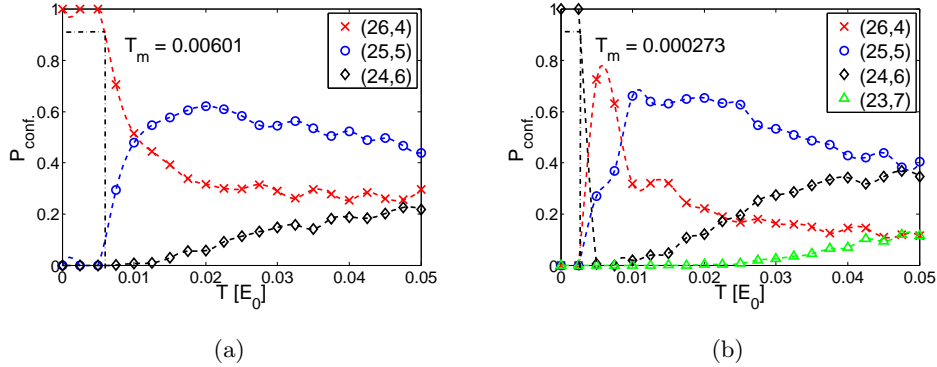


Figure 3.26.: Same as figure 3.25, but for (a) $N = 30$, $\kappa = 1.4$ and (b) $N = 30$, $\kappa = 1.5$.

$N = 40$ particles at two different screenings $\kappa = 0.0$, figure 3.27 (a), and $\kappa = 1.0$, figure 3.27 (b). Again the melting temperatures are similar to other parameters in the sense that the melting point for the system with higher screening is at higher temperature, $T_m^{crit} = 0.01124$ for the frequency of occurrence, compared to the system at lower screening, $T_m^{crit} = 0.00879$ for the frequency

3.3. Thermodynamic properties

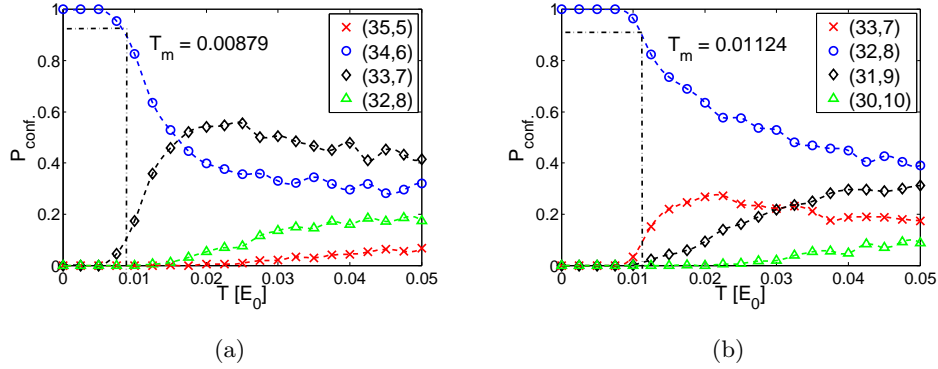


Figure 3.27.: Same as figure 3.25, but for (a) $N = 40$, $\kappa = 0.0$ and (b) $N = 40$, $\kappa = 1.0$.

of occurrence. This is normally not the case, systems with higher screenings melt at lower temperatures [112]. The second peculiarity is found for the higher screening in figure 3.27 (b). Here, the ground state configuration (32, 8) stays the most probable configuration in the MC samples over the complete range of temperatures tested.

Last but not least the third parameter used to identify the melting point was a generalized Lindemann-like criterion. The Lindemann criterion [126]

$$u_L = \frac{\langle \mathbf{u}^2 \rangle}{a^2} \quad (3.31)$$

predicts the melting when the fluctuation in the lattice positions $\mathbf{u}_i = \mathbf{r}_i - \mathbf{r}_{0,i}$ reaches a significant part of the lattice constant a and is widely used for a whole range of similar parameters. It was shown that this ratio has a universal value along the melting line [126] and differs even for different interaction potentials only slightly. For small clusters it was shown, that a phase transition causes a sudden increase in the width of the first peak of the bond length distribution, which is proportional to the pair distribution [127–129]. This knowledge was used by Peeters et al. to define the next neighbor distance fluctuations [131]

3. Yukawa balls

for radial melting, inter-shell melting and intra-shell melting

$$u_{intra}^k = \frac{1}{N_S} \sum_{i=1}^{N_S} \sqrt{\frac{\langle r_{ni}^2 \rangle}{\langle r_{ni} \rangle^2}} - 1, \quad (3.32a)$$

$$u_{inter}^k = \frac{1}{N_S} \sum_{i=1}^{N_S} \sqrt{\frac{\langle r_{mi}^2 \rangle}{\langle r_{mi} \rangle^2}} - 1, \quad (3.32b)$$

$$u_{rad} = \frac{1}{N_S} \sum_{i=1}^{N_S} \sqrt{\frac{\langle r_i^2 \rangle}{\langle r_i \rangle^2}} - 1. \quad (3.32c)$$

Here, k denotes the index for a shell, ni the next neighbor to particle i on the same shell, mi the next neighbor in an adjacent shell and r_i is the modulus of the position vector of the i th particle. These parameters can also be defined for not only neighboring particles, but all particles in the system, e.g. the *relative distance fluctuations* [130]

$$u_{rel} = \frac{2}{N(N-1)} \sum_{i<j} \sqrt{\frac{\langle r_{ij}^2 \rangle}{\langle r_{ij} \rangle^2}} - 1 = \frac{2}{N(N-1)} \sum_{i<j} \frac{\sqrt{Var(r_{ij})}}{\langle r_{ij} \rangle}, \quad (3.33)$$

where r_{ij} is the interparticle distance $r_{ij} = |\mathbf{r}_i - \mathbf{r}_j|$ for all pairs of particles. The main advantage is that there is no identification of neighboring particles, which even change during the simulation, needed to identify phase transitions. The identification of neighboring particles can be time consuming in the simulations due to the numerically challenging Voronoi analysis [91]. In contrast to the parameters (3.32a)-(3.32c), which define the melting by the amplitude of local oscillations, this parameter has a sharp increase at the phase transition point or region, while it is nearly constant in the solid ($u_{rel} \approx 0.05$) and liquid ($u_{rel} \approx 0.25$) phase. Although this parameter is widely used [114, 131, 132], extreme caution must be exercised when interpreting the $u_{rel}(T)$ curves, since they are dependent on simulation parameters such as the simulation length, as well as the ensemble that is used [133–135]. Figure 3.28 explains this behavior. The sharp increase and therefore the melting point moves with increasing simulation length to lower temperatures. The reason is, that for any finite temperatures a single pair distance averaged over the simulation will converge against the total pair distribution. And an indefinitely long simulation will even yield no visible increase at all. The relative distance fluctuations (3.33) include large scale diffusive motion without fixing a time scale for this motion. The simulation length artificially introduces a time scale, but this scale is without physical meaning. To circumvent this problem, it is possible to introduce a time scale by comparison with another melting parameter. The autocorrelation function

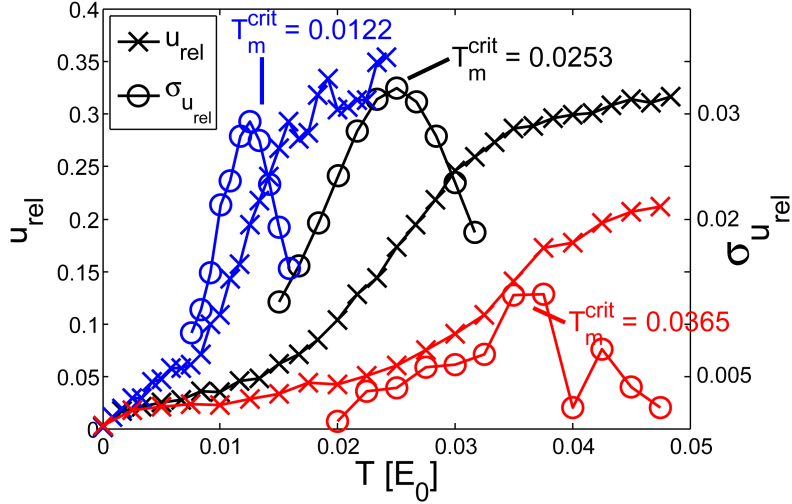


Figure 3.28.: Block averaged relative distance fluctuations u_{rel} and its variance $\sigma_{u_{rel}}$ as a function of temperature for a Yukawa ball with $N = 37$, $\kappa = 0.0$. The parameters u_{rel} and $\sigma_{u_{rel}}$ are averaged over 100 (red), 10^4 (black) and 10^6 (blue) MC steps which leads to different melting temperatures, ranging from $T_m^{crit} = 0.0122$ (10^6 MC steps) to $T_m^{crit} = 0.0365$ (100 MC steps).

of the total energy

$$C_E(k) = \frac{\sum_{i=1}^{L-k} (E_{i+k} - \langle E \rangle)(E_i - \langle E \rangle)}{(L-k)(\langle E \rangle - \langle E \rangle^2)} \quad (3.34)$$

is such a parameter. Here, L is the total number of steps in the simulation and k the lag of the correlation. This parameter shows the slowest decay in the transition region and the melting temperature can be identified by the maximum of the correlation time of $C_E(k)$. It was found [136] that the block length, where the melting temperatures of $C_E(k)$ and u_{rel} agree, is in the range of $1000 \dots 10000$. For the estimation of the melting point T_m^{crit} by the relative distance fluctuations it is suitable to use the *variance of the block averaged relative distance fluctuations*

$$\sigma_{u_{rel}} = \frac{1}{K} \sum_{s=1}^K \sqrt{\langle u_{rel}^2(s) \rangle - \langle u_{rel}(s) \rangle^2}, \quad (3.35)$$

with K the number of blocks. This parameter allows to identify the melting point instead of a region more easily, cf. figure 3.28, and is used for the comparison of the melting temperatures in the appendices B.1 and B.2.

3. Yukawa balls

3.3.2. Phase diagram

With the melting parameters C_V , P_{conf} , and $\sigma_{u_{rel}}$ the melting temperatures can be determined and used to draw a phase diagram for mesoscopic Yukawa balls. With the parameters C_V and $\sigma_{u_{rel}}$ sometimes intrashell as well as inter-shell melting processes are detected, but for the comparison and tables only the lower melting temperature, generally the intrashell melting temperature, is considered. Such a phase diagram is given in figure 3.29. The critical temperature

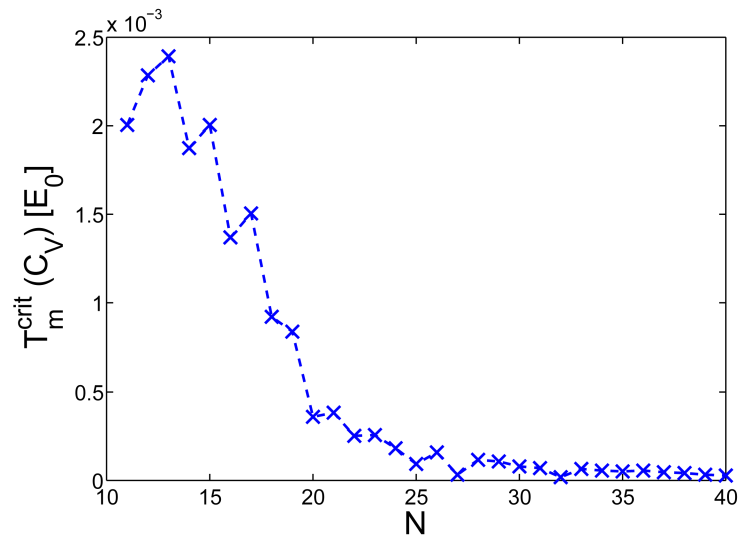


Figure 3.29.: Phase diagram of Yukawa balls with $N = 11, \dots, 40$ and a fixed screening $\kappa = 1.0$. The given melting temperatures are calculated by the specific heat and decrease with increasing total number of particles. The exceptions at $N = 15, 17, 21, 26, 28, 33$ are small compared with decrease in their vicinity.

of the solid-liquid phase transition is determined by the specific heat (3.30) and given for $N = 11, \dots, 40$ and fixed screening $\kappa = 1.0$. The melting temperature T_m^{crit} as a function of the total particle number N is non-monotonically dropping from $T_m^{crit} = 0.002396$ for $N = 13$ to $T_m^{crit} = 0.000024$ for $N = 40$. Some exceptions of this decrease in the melting temperature are $N = 15, 17, 21, 26, 28, 33$ although the increase is small compared to the overall decrease of the melting temperature as a function of the total particle number.

The essential information of the phase diagram in figure 3.29 is the melting temperature T_m^{crit} . This critical temperature is given in the figure 3.30 for C_V (a) and for $\sigma_{u_{rel}}$ (b) for particle numbers $N = 11 \dots 40$ and screenings $\kappa = 0.1 \dots 5.0$. Additionally the melting temperatures and potential barrier

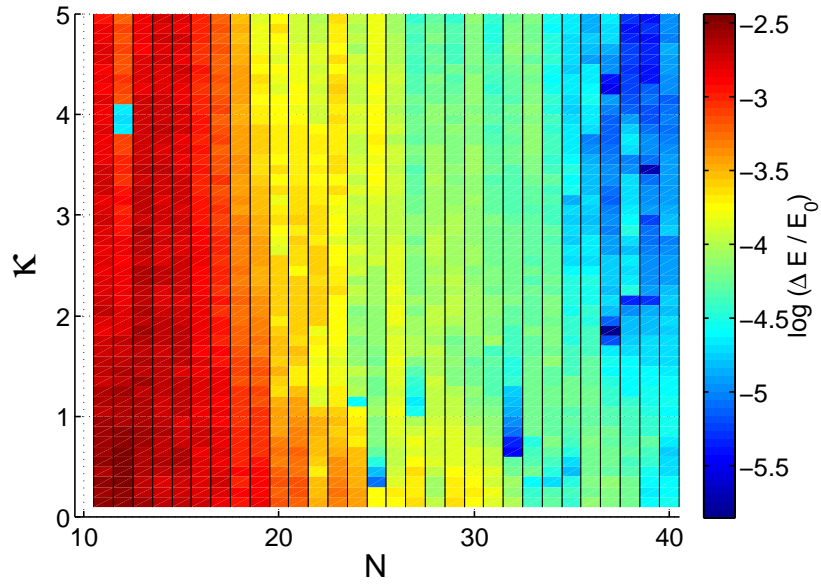
3.3. Thermodynamic properties

heights for these particle numbers are given in appendix B.2 for comparison. The melting temperatures of C_V and $\sigma_{u_{rel}}$ coincide most of the time, which proves that the estimate of a block length of 1000, used in the simulations is indeed a good value to determine phase transitions in the MC simulations carried out in this work. This is also seen in figure 3.30 since differences are hardly spotted in the two diagrams. Only for $N = 23$ at high screenings $\kappa = 4.0 \pm 0.5$ a difference in the melting temperatures measured by the specific heat (a) and the variance of the block averaged relative distance fluctuations (b) can be seen. Nevertheless, the melting temperatures deviate a little between these parameters, but this can only be seen in the table of appendix B.2. Also, the measured melting temperatures coincide roughly with those measured by other authors [122, 131].

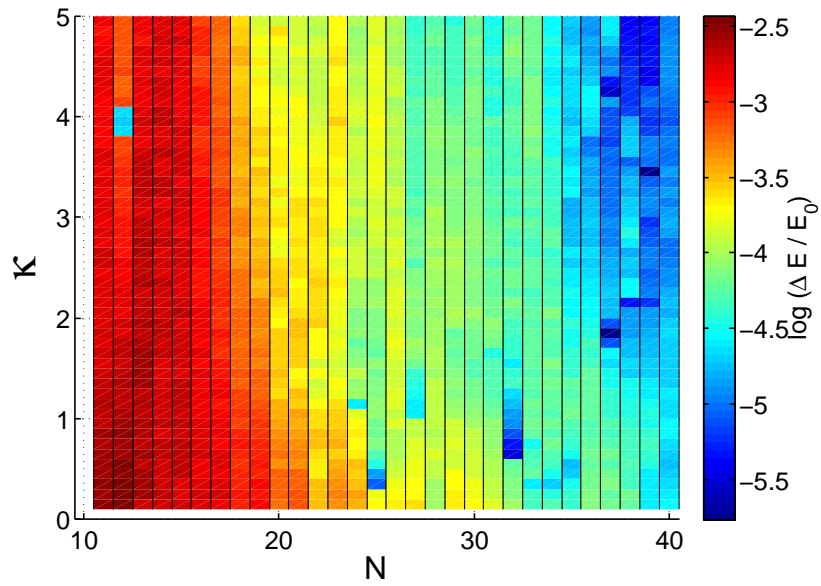
The melting temperatures measured by the frequency of occurrence of different shell configurations are better compared against the radial potential energy barrier heights because these temperatures only involve radial transitions. These critical temperatures are plotted in figure 3.31. Compared with the radial potential energy barrier heights in figure 3.19 and appendices B.1 and B.2 some deviations are seen, but the general trends are alike. The reason for the deviations is that for the frequency of occurrence the potential energy barrier heights of the metastable states also influence the probability of the states. A low potential energy barrier height for the first metastable state compared to the potential energy barrier height of the ground state implies that it is relatively easy for particles to leave the metastable state, which reduces the relative frequency of occurrence. Then even if the temperature is high enough to leave the ground state the metastable state will not occur much more often. This is also seen in the comparison of the potential energy barrier heights and melting temperatures measured by the frequency of occurrence in the appendices B.1 and B.2. In general, the measured melting temperature is higher than the potential barrier height.

To summarize, the known general trends, that the liquid-solid phase transitions occur at lower temperatures with increased screening [86, 112] and decreased system size [113] are not necessarily seen in the computed critical temperatures of mesoscopic Yukawa balls. Indeed, in general the melting temperatures decrease with increase of screening for a fixed particle number N . On the other hand, the trend that smaller systems melt earlier [113] is reversed here. Here, often magic number clusters are part of the configuration. Magic

3. Yukawa balls



(a)



(b)

Figure 3.30.: Critical temperatures for the solid-liquid transition of mesoscopic Yukawa balls with $N = 11, \dots, 40$ and $\kappa = 0.1, \dots, 5.0$. The color indicates the logarithmic melting temperature as measured by the specific heat (a) and the variance of the block averaged relative distance fluctuations (b).

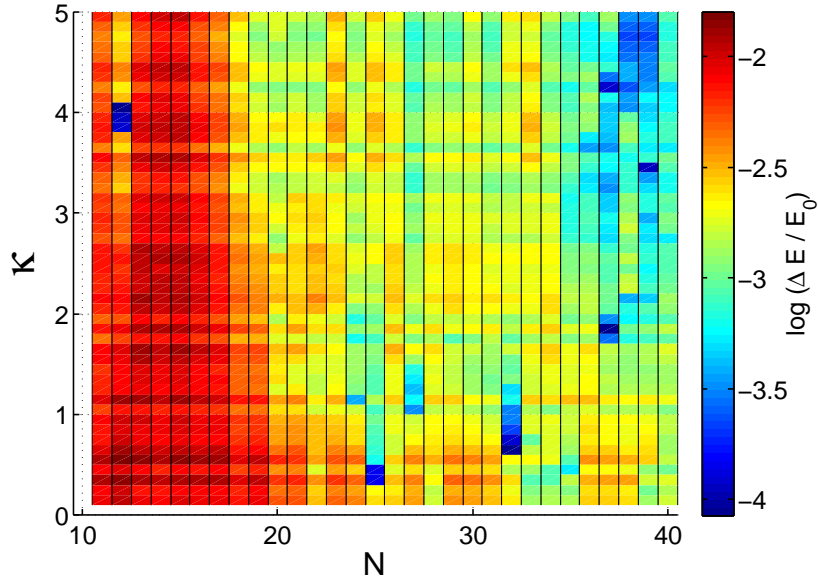


Figure 3.31.: Critical temperatures for the solid-liquid transition of mesoscopic Yukawa balls with $N = 11, \dots, 40$ and $\kappa = 0.1, \dots, 5.0$. The melting temperature, given in logarithmic scale, is measured by the relative frequency of occurrence, cf. section 3.3.1.

number clusters are those that form a perfect symmetric structure, in other words a platonic body. The platonic bodies are the tetrahedron (4 particles), the octahedron (6 particles), the cube or hexahedron (8 particles), the icosahedron (12 particles) and the dodecahedron (20 particles). These bodies are very stable against any transitions and occur often as part of the ground state configurations and are for mesoscopic clusters a huge fraction of the total system. Exceptions to the lowered melting temperature with increased total number of particles are frequent but the increase in the critical temperature is small compared to the general trend of decreasing melting temperatures. For bigger systems with a few hundred particles the platonic bodies are only a very small fraction of the total system and therefore do not influence the stability of the whole cluster. Already in [113] the smallest calculated system for $N = 100$ had a melting temperature above the predicted value. Therefore, the reversal of this trend for the mesoscopic clusters analyzed here with $N = 11, \dots, 40$ can be understood.

3. Yukawa balls

3.4. Results in relation to experiments and theory

Already the found ground state configurations were able to reproduce the shell populations of experimental clusters when the particles are interacting with a Yukawa potential instead of a Coulomb potential. For screening parameters $0.55 \leq \kappa_{sim} \leq 1.19$ the ground state configurations in the simulation were consistent with the experimentally observed shell populations, cf. section 3.2.2. Still some observation in experiments need to be studied in more detail.

3.4.1. Structural transitions

In the experiments of references [137, 138] particle movement did also lead to structural transitions as seen in the simulations. In the upper image of figure 3.32 such a particle movement can be seen for a cluster with 31 particles. The cluster is in the configuration (27, 4) when one particle leaves the outer shell at $t \approx 420s$ and moves to the inner shell in the next 80s. In the lower part the potential energy barrier is plotted again for comparison, cf. figure 3.18. Interestingly the kink in the calculated barrier coincides with the return point of the particle in the experiment.

Hence, these measurements consistently show that metastable configurations

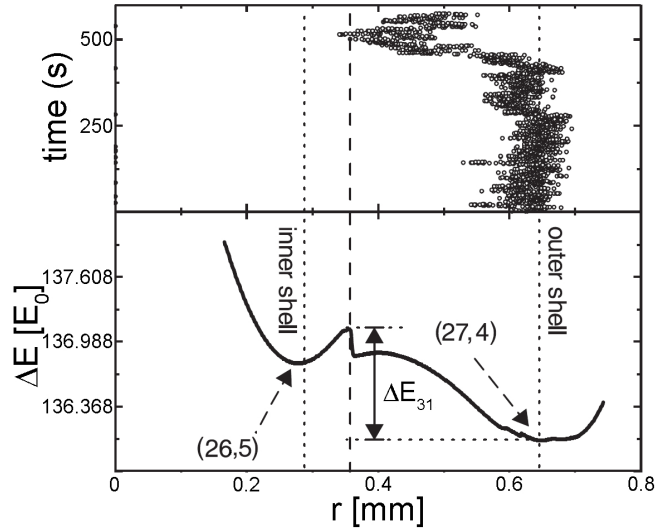


Figure 3.32.: Radial component of the trajectory of the particle leaving the outer shell in the experiment (upper image). Potential energy barrier for the Yukawa ball with $N = 31$, $\kappa =$, cf. figure 3.18. From reference [137].

are thermally accessible in experiments at room temperature [137] and can occur frequently in experiments [138]. To my knowledge no experiments have

3.4. Results in relation to experiments and theory

been performed yet that record the configurations over time at the given temperature in an experiment and could be compared to the relative frequency of occurrence in the MC simulations at finite temperatures. Nevertheless, simulations showed, as seen in figure 3.5, that for the assumed coupling parameter in the experiments, finite temperature effects are negligible for radial transitions.

3.4.2. Probability of occurrence of stationary states

However, there are experiments that record the probability of occurrence of different configurations for the same cluster. In this set of experiments it was intended to realize different metastable configurations of clusters with fixed total particle number. For the production of the different metastable configurations the following procedure was applied. After the trapping of the particles, the rf-power was varied, so that the particles were not confined for a few seconds. The Yukawa ball is destroyed and before the particles leave the discharge the trapping was reestablished, so that the particles may form a new stable configuration [137, 138]. With this procedure a total of 37 different clusters with 31 particles could be observed. From the table in appendix A.1 it is known that the ground state configuration for a Yukawa ball with 31 particles is (27, 4) up to $\kappa = 1.56$, (26, 5) thereafter up to $\kappa = 1.61$ and then (25, 6). These configurations are all seen in this experiment as well and the probabilities are $35 \pm 10\%$ for the ground state configuration (27, 4), $62 \pm 13\%$ for (26, 5) and $3 \pm 3\%$ for the configuration (25, 6).

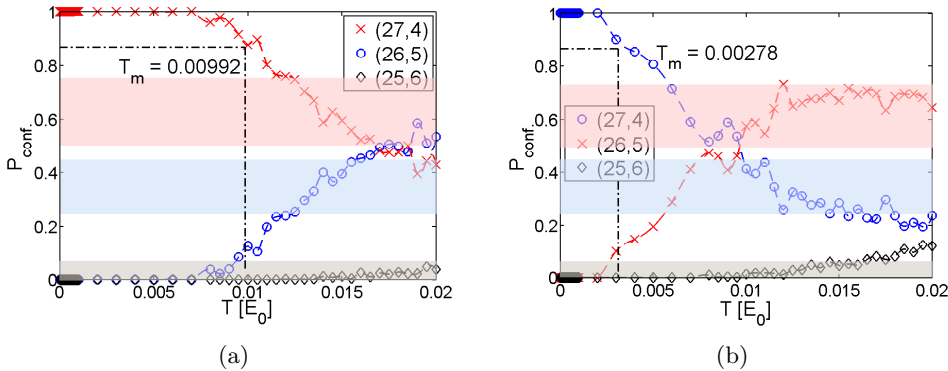


Figure 3.33.: Probability of occurrence of different stable configurations for a cluster with (a) $N = 31$, $\kappa = 0.8$ and (b) $N = 31$, $\kappa = 1.1$. The horizontal bars indicate the experimentally observed frequencies of occurrences with error bars.

3. Yukawa balls

Figure 3.33 shows the probability of occurrence P_{conf} of these states for the cluster with 31 particles at screenings of $\kappa = 0.8$ (a) and $\kappa = 1.1$ (b). The horizontal bars indicate the experimentally observed frequencies of occurrence for the configurations (27, 4) (red), (26, 5) (blue) and (25, 6) (grey). Assuming that the experimental screening is around this range of screening $\kappa \approx 1.0$, the lowest temperature that is able to reproduce the experimental observations is $T \approx 0.01$, which translates into the coupling parameter $\Gamma_C \approx 100$. However, the corresponding potential barrier heights are an order of magnitude smaller than this temperature whereas the estimated coupling parameter in the experiments is $\Gamma_C^{exp} \approx 500$. Therefore the reason for the more frequent observation of configuration (26, 5) can not be finite temperature effects.

It has been shown [84] that the main effect in these repetition experiments is the friction of the neutral gas. An analysis by extensive MD simulations showed that the damping coefficient strongly affects the occurrence probabilities of metastable states even if the interaction and the confinement are not changed. This is similar to the liquid solid transition in macroscopic systems where rapid cooling may give rise to a glass-like disordered solid rather than a crystal with lower energy. While slow cooling leads predominantly to the lowest energy state, strong damping gives rise to an increased probability of metastable states. This is the main effect seen in the repetition experiments [137, 138]. For friction coefficients of $\nu > 2.0\omega_0$, where ω_0 is simply the scaled strength of the external confinement α in (3.1), the system is in the overdamped regime and the probability distribution of the stable states for the cluster with 31 particles and $\kappa = 0.8$ is found to be within the experimental error. In the overdamped regime, $\nu > 2.0\omega_0$ the probabilities of the different configurations will not change much with increasing the friction coefficient. The assumed friction parameter in the experiments is in the range $\nu = 3 \dots 6\omega$ [137] which then coincides with the observations in the simulations.

From the comparison of the potential barrier height and the particle movement in the experiment, cf. figure 3.32, together with an estimated screening parameter of $0.5 < \kappa < 1.2$, the estimated kinetic energy of the moved particle is $0.0012 < E_{kin} < 0.0025$. Assuming this, one can determine other experimentally interesting clusters, that have lower or equal potential barrier heights than the cluster with $N = 31$, $0.5 < \kappa < 1.2$. The following particle numbers may be of interest to experimenters. The particle numbers $N = 25, 27, 32$ all have lower radial potential energy barriers compared to the $N = 31$ cluster for all

3.4. Results in relation to experiments and theory

screenings considered, while the particle numbers $N = 26, 33, 34, 35, 40$ have at least one radial potential energy barrier that is lower than the one of the $N = 31$ cluster. For these clusters radial transitions due to thermal movement can be expected in the experiments. For other clusters thermal induced transitions out of the ground state should not occur. Of course, if the experimental cluster is not in the ground state configuration, other potential energy barriers and melting temperatures are valid and transitions out of these metastable states might be more likely to happen.

Harmonic approximation

A promising approach to calculate the probabilities of occurrence of different states of Yukawa balls is an analytical description. The total energy of the system thermally excited from a given state s (ground or metastable state) can be expanded around the local minimum with energy E_0 and individual particle positions r_1^0, \dots, r_N^0 up to second order in the displacements, which then allows the evaluation of the partition function [139]. Here, the partition function

$$Z_s = n_s Z_s^{int} Z_s^{vib} Z_s^{rot}, \quad \text{with the degeneracy factor } n_s = \frac{N!}{\prod_{i=1}^L N_i^{s!}}, \quad (3.36)$$

where L is the number of shells and N_i^s the occupation number of shell i with $\sum_{i=1}^L N_i = N$, can be factorized. The internal, vibrational and rotational parts are

$$Z_s^{int} = e^{-\beta E_s^0} \quad (3.37a)$$

$$Z_s^{vib} = \left(\frac{k_B T}{\hbar \Omega_s} \right)^f \quad (3.37b)$$

$$Z_s^{rot} = \left(\frac{2\pi k_B T \bar{I}_s}{\hbar^2} \right)^{3/2}. \quad (3.37c)$$

Here, f denotes the degrees of freedom, $\Omega_s = (\prod_{i=1}^f \omega_{s,i})^{1/f}$ is the geometric mean eigenfrequency and $\bar{I}_s = (I_{s,1} I_{s,2} I_{s,3})^{1/3}$ the mean moment of inertia. With these formulas it is possible to compute the ratio of probabilities of two states s and s' as [84]

$$\frac{P_s}{P_{s'}} = \frac{n_s}{n_{s'}} \left(\frac{\Omega_{s'}}{\Omega_s} \right)^f \left(\frac{\bar{I}_s}{\bar{I}_{s'}} \right)^{3/2} e^{-\beta(E_s^0 - E_{s'}^0)} \approx \frac{n_s}{n_{s'}} \left(\frac{\Omega_{s'}}{\Omega_s} \right)^f e^{-\beta(E_s^0 - E_{s'}^0)}. \quad (3.38)$$

Although this harmonic approximation is only valid for small temperatures a

3. Yukawa balls

comparison with MC simulations shows a very good agreement. Figure 3.34

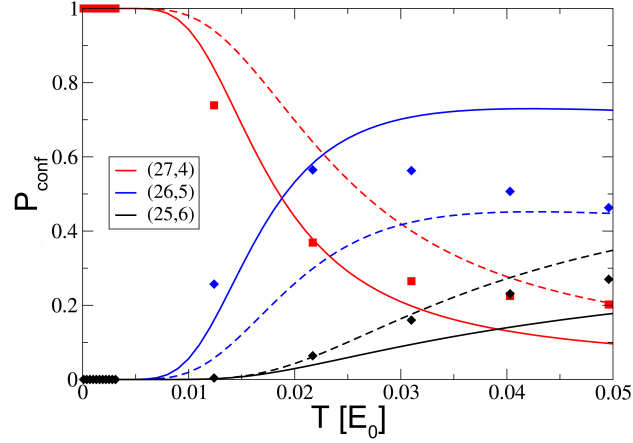


Figure 3.34.: Probability of occurrence for the different stable states of a cluster with $N = 31$, $\kappa = 0.8$. The symbols denote the probabilities obtained from MC simulations at these temperatures while the solid lines are the probabilities calculated by equation (3.38).

gives an example for $N = 31$, $\kappa = 0.8$. The results of equation (3.38) (solid lines) agree even to quite large temperatures $T \leq 0.02$, compared to the melting temperature $T_m^{crit} = 0.000079$ as determined by the specific heat parameter, cf. appendix B.1. If this good agreement holds for several clusters and screenings and if the probability of occurrence of the ground state configuration can be used to determine the melting temperature, this approximation should be able to predict melting temperatures for Yukawa balls as well.

4. Yukawa tubes

Yukawa tubes are another system of dust particles considered in this thesis. These systems are periodic in the z -direction and restricted by a harmonic confinement in the $(x - y)$ plane. An example of a simulated Yukawa tube with a length density of $N/L_z = 75.0$ and a screening parameter of $\kappa r_0 = 2.0$ is given in figure 4.1. These systems are described by considering N identical interacting particles with mass m and charge q in a axial symmetric harmonic confinement potential in a simulation box of length L_z with periodic boundary conditions, described by the Hamiltonian

$$H(\mathbf{r}_i, \mathbf{p}_i) = \sum_i^N \frac{\mathbf{p}_i^2}{2m} + \sum_i^N \frac{\gamma}{2} (x_i + y_i)^2 + \sum_{i < j}^N \frac{q^2}{r_{ij}} \exp^{-\kappa r_{ij}}. \quad (4.1)$$

In the simulations, dimensionless length and energy variables are used by introducing the units $r_0 = (2q^2/\gamma)^{1/3}$ and $E_0 = (2\gamma q^4)^{1/3}$, respectively. Due to the periodic boundary condition along the z -direction it is impossible to take into account all pair interactions and therefore one can define a cutoff distance (normally the boxlength L_z) in which case the interaction energy is subject to errors. To reduce this error alternative methods can be used, e.g. the Ewald summation.

Figure 4.1 shows an example of a Yukawa tube with a length density $\rho_l = N/L_z = 75.0$ and a screening parameter of $\kappa r_0 = 2.0$. The view from top (a) is an integrated view along the lateral dimension over all particles in the simulation box and it shows a similar shell structure as in the $2d$ dust crystals [22, 29, 140]. Along the z -dimension (b) no special structure is observed at this length density and screening.

4.1. Ewald summation

When applying periodic boundary conditions for three-dimensional systems, the sum of the energy over the images of the system is only conditionally convergent. To solve this problem, the Ewald summation technique [141] is widely used [142–145]. In general, the Ewald summation technique is based on the idea of

4. Yukawa tubes

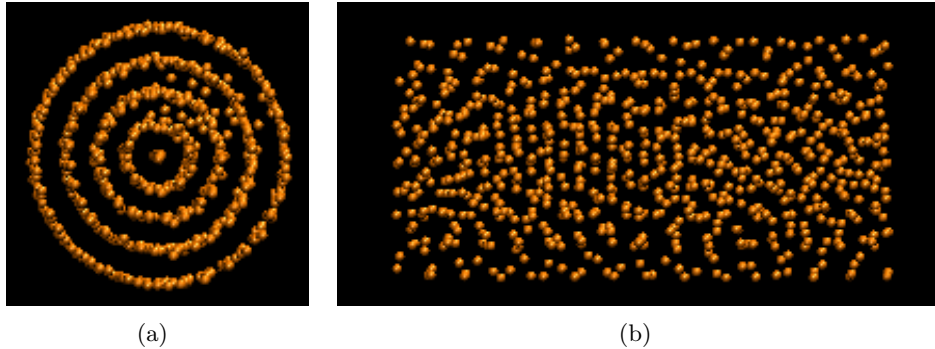


Figure 4.1.: Example of a simulated Yukawa tube with a length density of $N/L_z = 75.0$ and a screening parameter of $\kappa r_0 = 2.0$. a) View from top along the z -dimension and b) orthographic view from the side. Similar to $2d$ dust crystals [22, 29, 140] a shell structure can be seen in a). These structures are arranged in layers, while the shell population in each layer can vary slightly from layer to layer (cf. section 4.2.2).

Ewald [146] in 1921. He proposed an efficient way to recast the summation of interaction energies in a periodic lattice in two rapidly converging series

$$V(r) = V_{long}(r) + V_{short}(r), \quad (4.2)$$

a short range term and a long range term, where

$$V_{short}(r) = V(r) \operatorname{erfc}(\sqrt{\alpha}r) \quad (4.3a)$$

$$V_{long}(r) = V(r) - V_{short}(r) = \operatorname{erf}(\sqrt{\alpha}r)V(r) \quad (4.3b)$$

and

$$r = |\mathbf{r}_i - \mathbf{r}_j|.$$

Here, erf is the error function and erfc the complimentary one. The short range interaction potential decays very fast in real space and the long range part can be easily evaluated in Fourier space. Therefore, the method implicitly assumes that the system is infinitely periodic, which is the case in this study. The control parameter α determines the convergence speed in both the real and Fourier space series. There are a lot of textbooks [147–149] on the application of this idea to various systems.

However, in some cases one may encounter systems, which are infinite in some directions and finite in other directions. For example, in simulations of membranes and other liquid or solid surfaces, one needs to extend the Ewald summa-

tion technique to three-dimensional systems with periodicity in two directions only, where the result has been obtained recently [150, 151]. Here, results of the Ewald summation technique are used to compute the energy of longrange electrostatic interactions in three-dimensional systems with periodicity in one direction [152]. Apart from complex plasmas, possible applications include transport of charged particles through channels or wires [153–155]. So far, only results for Coulomb interaction for quasi-1d systems are available and therefore, for the Yukawa tubes with screened Coulomb interaction the standard technique of defining a cutoff distance for the interactions was used. The error in the computed energies decreases with the increase of the screening κ and therefore only for small screenings $\kappa < 1.0$ one really awaits a difference, while for larger screenings the computed energies should not vary too much.

Coulomb interaction

The third sum in equation (4.1) in a system with periodic boundary conditions in z direction reads in the Coulomb case as

$$V_{ij}(\mathbf{r}_i, \mathbf{r}_j) = \frac{1}{2} \sum_{i,j=1}^N \sum'_n \frac{q^2}{|r_{ij} + n|}. \quad (4.4)$$

The sum over $n = (0, 0, aL_z)$ with integer a is the sum over the original and the images of the system, and the prime indicates that for $n = \mathbf{0}$ the terms with $i = j$ are to be omitted. Defining the function $\Phi(r)$ and the factor Φ_0 as

$$\Phi(r) = \sum_n \frac{1}{|r + n|} \quad \text{for } r \neq 0 \quad (4.5a)$$

and

$$\Phi_0 = \sum_{n \neq \mathbf{0}} \frac{1}{|n|} \quad (4.5b)$$

one may rewrite the equation (4.4) as

$$V_{ij}(\mathbf{r}_i, \mathbf{r}_j) = \sum_{i < j}^N q^2 \Phi(r_{ij}) + \frac{1}{2} \sum_{i=1}^N q^2 \Phi_0. \quad (4.6)$$

The first term in equation (4.6) sums up the contributions from each charge interacting with all other charges, the originals as well as their images, whereas the second term represents the contribution from the interaction of each charge with its own images.

To calculate the sums in equation (4.5a), the work of Porto [152], who devel-

4. Yukawa tubes

oped Ewald summation formulas for quasi-one dimensional system with no net charge, was followed and the expressions for $\Phi(r)$ and Φ_0 are given by

$$\begin{aligned} \Phi(r) = & \sum_n \frac{\operatorname{erfc}(\alpha|r+n|)}{|r+n|} + \frac{1}{L} \sum_G \left[\left\{ \frac{1}{L} \left(\log(\alpha^2) - \lim_{t \rightarrow 0^+} \log(t) - \gamma \right. \right. \right. \\ & \left. \left. \left. - \Gamma\left(0, \alpha^2[r_x^2 + r_y^2]\right) - \log\left(\alpha^2[r_x^2 + r_y^2]\right) \right) \right\} \right. \\ & \left. + \left\{ \sum_{\nu=0}^{\infty} \frac{(-1)^\nu}{4^\nu \nu!} G^{2\nu} [r_x^2 + r_y^2]^\nu \Gamma\left(-\nu, \frac{G^2}{4\alpha^2}\right) \right\} \right], \end{aligned} \quad (4.7a)$$

and

$$\begin{aligned} \Phi_0 = & \sum_{n \neq 0} \frac{\operatorname{erfc}(\alpha|n|)}{|n|} + \frac{1}{L} \left[\log(\alpha^2) - \lim_{t \rightarrow 0^+} \log(t) \right] \\ & + \frac{1}{L} \sum_{G \neq 0} \Gamma\left(0, \frac{G^2}{4\alpha^2}\right) - \frac{2\alpha}{\sqrt{\pi}}, \end{aligned} \quad (4.7b)$$

where γ denotes Euler's constant, $\Gamma(s, t)$ the incomplete gamma function and r_x and r_y the x and y components of \mathbf{r} . Here, a factor α is introduced as a damping factor, which is used in simulations so that the sum in real space can be truncated by omitting contributions from pairs (i, j) for which $|r_{ij}| > L/2$. This means, that the real-space sum is restricted to the original simulation box by applying the minimum image convention. For the sum over the reciprocal space, normally 100 – 200 wavevectors are used. Putting together equations (4.7a) and (4.6) yields the final result

$$\begin{aligned} V_{ij}(\mathbf{r}_i, \mathbf{r}_j) = & \frac{1}{2} \sum_{i,j=1}^N q^2 \sum_n' \frac{\operatorname{erfc}(\alpha|r_{ij}+n|)}{|r_{ij}+n|} + \frac{1}{2L} \sum_{i,j=1}^N q^2 \sum_{G \neq 0} \exp(iGr_{ij,z}) \\ & \times \begin{cases} \sum_{\nu=0}^{\infty} \frac{(-1)^\nu}{4^\nu \nu!} G^{2\nu} [r_{ij,x}^2 + r_{ij,y}^2]^\nu \Gamma\left(-\nu, \frac{G^2}{4\alpha^2}\right) & \text{for } r_{ij,x}^2 + r_{ij,y}^2 \neq 0 \\ \Gamma\left(0, \frac{G^2}{4\alpha^2}\right) & \text{for } r_{ij,x}^2 + r_{ij,y}^2 = 0 \end{cases} \\ & + \frac{1}{2L} \sum_{\substack{i,j=1 \\ r_{ij,x}^2 + r_{ij,y}^2 \neq 0}}^N q^2 \left\{ -\gamma - \Gamma\left(0, \alpha^2[r_{ij,x}^2 + r_{ij,y}^2]\right) - \log\left(\alpha^2[r_{ij,x}^2 + r_{ij,y}^2]\right) \right\} \\ & + \frac{\alpha N q^2}{\sqrt{\pi}} + \frac{q^2}{L} \sum \left[\log(\alpha^2) - \lim_{t \rightarrow 0^+} \log(t) \right]. \end{aligned} \quad (4.8)$$

The divergent part, $\log(\alpha^2) - \lim_{t \rightarrow 0^+} \log(t)$, resulting from the case $G = 0$ would vanish for systems with charge neutrality. The distances $r_{ij,x}$, $r_{ij,y}$ and

4.2. Structural properties

$r_{ij,z}$ denote the x, y and z components of r_{ij} . Also note, that $\lim_{\mu \rightarrow 0^+} (-\gamma - \Gamma(0, \mu) - \log(\mu)) = 0$.

Using the integral representation of the gamma function and the Poisson summation formula [156] an Ewald summation technique is developed for long-range electrostatic interactions in systems that are periodic in one direction and have a finite extension in the two other directions. A convergence factor, proposed for the summation with periodicity in all three directions [144], is not needed. This result is similar to the case of three-dimensional systems with periodicity in two directions [150, 151].

Yukawa interaction

For Yukawa interaction, Ewald summation equations have not been available, although they should be easily derived from the Ewald summation formulas for Coulomb interaction following the idea of [157, 158]. Nevertheless, here standard periodic boundary conditions in the z -direction with the minimum image convention were used. Therefore the computed energies may have small errors but with increasing screening strength κ these errors will decrease since the interaction strength will decrease exponentially, too. On the other hand the errors increase with the increase of the length density $\rho_L = N/L_z$, as seen in figure 4.2. Here, the ground state energies for different length densities and for a fixed screening parameter of $\kappa r_0 = 1.0$ are plotted. For length densities $\rho_L \leq 6.0$, boxlengths of $L_z \geq 10r_0$ are sufficient to compute the ground state energy with a good precision. For higher screening parameter even smaller boxlength can be used in the simulations. For the simulations of the ground states normally a boxlength around $L_z = 10r_0$ was used for length densities $\rho_L \leq 6.0$ and $L_z \approx 20r_0$ above.

4.2. Structural properties

With the help of the correct energies, calculated by the Ewald summation, one can compute the ground states by standard Monte Carlo simulation techniques with the Metropolis algorithm [76] as described in section 2.2.2. The first interest in these systems focuses on the structural properties. Therefore, the system is initialized from randomly placed particles at a high temperature and then it is systematically cooled down, so that the particles can relaxate into a equilibrium position. This procedure is repeated several hundred times up to several thousand times to ensure a high probability that the found stable state is actually the ground state configuration of the system. Figure 4.3 shows a

4. Yukawa tubes

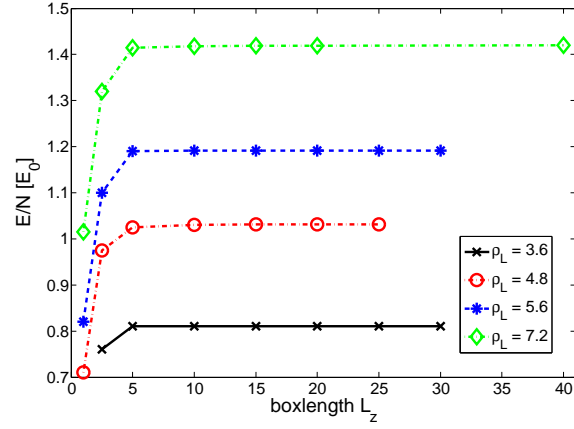


Figure 4.2.: Ground state energies of Yukawa tubes with a fixed screening parameter of $\kappa r_0 = 1.0$ and different length densities $\rho_L = \{3.6, 4.8, 5.6, 7.2\}$. The ground state energies are reaching the asymptote for boxlengths $L_z \geq 15$.

schematic view of a Yukawa tube with the according descriptions of the distances within this system. In the simulation we can vary the length density ρ_L

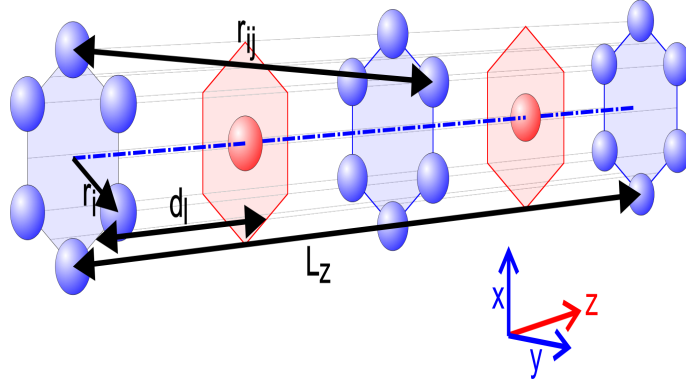


Figure 4.3.: Schematic view of a Yukawa tube with description of the different distances. r_{ij} is the 3d-distance, L_z is the length of the simulation box and d_l is the distance between the layers. r_i is the radial position of particle i .

by changing the number of particles N and/or the simulation box length L_z ; the other parameters are the screening strength of the interaction κ and the coupling parameter Γ . The harmonic confinement strength γ in equation (4.1) cancels out when one introduces the length scale r_0 . To reduce the influence of the simulation box on the final stable state configuration, the boxlength L_z and

the total number of particles N were changed so that the length density ρ_L was constant. For future analysis and in order to reduce the error from the shape (length) of the simulation box grandcanonical simulations should be performed.

4.2.1. Unit cell definition

All found final stable states can be very complicated; one can find twisted helica, line ordered systems or other configurations. Therefore, one needs to find a suitable description to define the configurations. In general, the stable state configurations consists of layers of certain shape, like $2d$ dust crystals [22, 159]. But first, each layer can have a different configuration from the one before and after, and second, even if the layers have the same configurations the layers can be twisted by a well defined angle. Therefore a unit cell of the system is defined as the smallest number of layers after which the layer configurations repeat themselves. Additionally a rotation angle is determined between the layer in the unit cell and the same layer in the next cell. An example is shown in figure 4.4. Here the unit cell is $[(1, 5)]$ with a rotation angle of $[(0^\circ, 36^\circ)]$, which means that the unit cell consists of one layer with 5 particles on the outer shell and 1 particle in the center. The next layer again consists of 5 particles on the outer shell and 1 particle in the center, but the outer shell is rotated by 36° so that the integrated view from top 4.4(b) shows 10 particles for the outer shell. With this rotation angle, the layers with their specific shell configurations *and* rotation angles repeat themselves after 2 cells, therefore a packing notation would be $ABABAB\dots$. There can be also configurations of unit cells with several layers, as seen in figure 4.5. Here, the unit cell consists of 2 layers with the configurations $(1, 7)$ and $(3, 7)$, where the first number represents the shell population on the inner shell or the center and the second number the shell population on the outer shell. The center particle can be rotated arbitrarily, the 3 particles on the inner shell of the second layer are (nearly) staying in the same place in the plane (x, y) . From the integrated view from top in figure 4.5(b) one can see 14 positions of particles on the outer shell, but from the pictures of the layers of the unit cell in (c) it is clear that the 7 particles of the second layer are rotated by $\approx 26^\circ$ against the 7 particles of the first layer. Therefore, the notation for this ground state configuration is $[(1, 7); (3, 7)], [(0^\circ, 0^\circ); (0^\circ, 0^\circ)]$. These short examples give an insight to the manifold of possible configurations which can be stable state configurations. Fortunately, the ground state configurations normally have a simple structure of one or two layers which repeat themselves after 2 cells, as seen in the example here.

4. Yukawa tubes

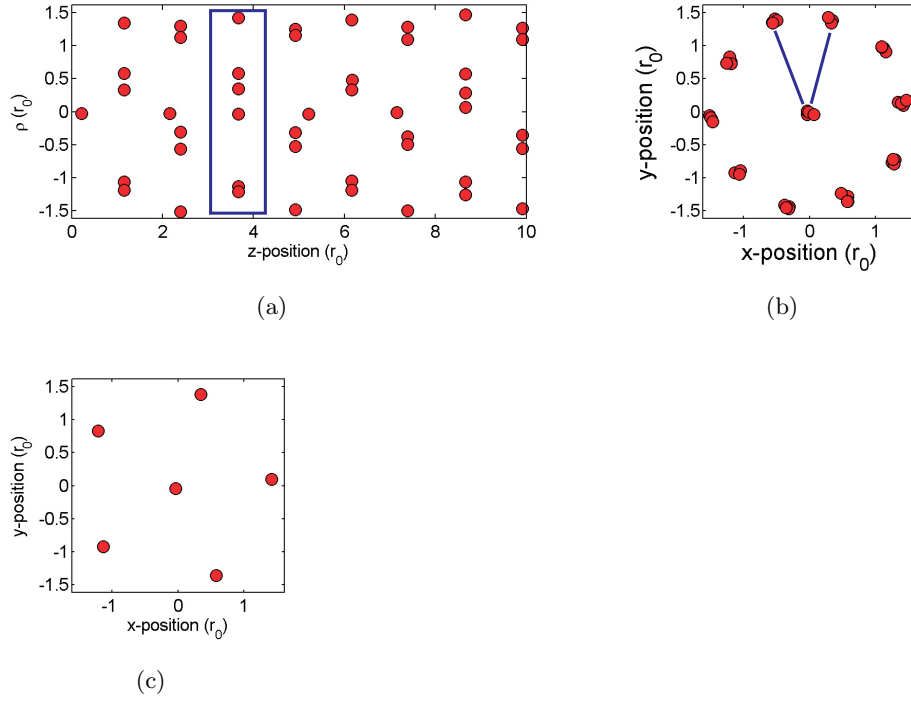


Figure 4.4.: Ground state configuration $[(1, 5)]$ with a rotation angle $[(0^\circ, 36^\circ)]$. The example for this configuration is chosen for a length density of $\rho_L = 4.6$ and Coulomb interaction ($\kappa = 0.0$). The view from the side (a) shows that each layer consists of 6 particles, while the integrated view from top (b) shows 10 positions of particles on the outer shell and the center particle. Therefore, the unit cell, seen in (c), of 5 particles on the outer shell and the center particle is rotated by 36° for the outer shell and arbitrarily for the center particle.

4.2.2. Ground states

Extensive Monte Carlo simulations were performed in order to compute the ground states of Yukawa tubes with different length densities and different screening. For each tuple of length density and screening at least 100 Monte Carlo simulations (1000 for $\rho_L < 7.0$) with 10^9 Monte Carlo steps in total were performed, where the system was cooled down by 0.1% every 1000th Monte Carlo step. The presented states with the lowest energy are referred to as ground states of the Yukawa tubes, although there might be configurations with lower energy as explained in 3.2.1.

General trends are not as easy to obtain as seen in section 3.2.1. Figure 4.5

4.2. Structural properties

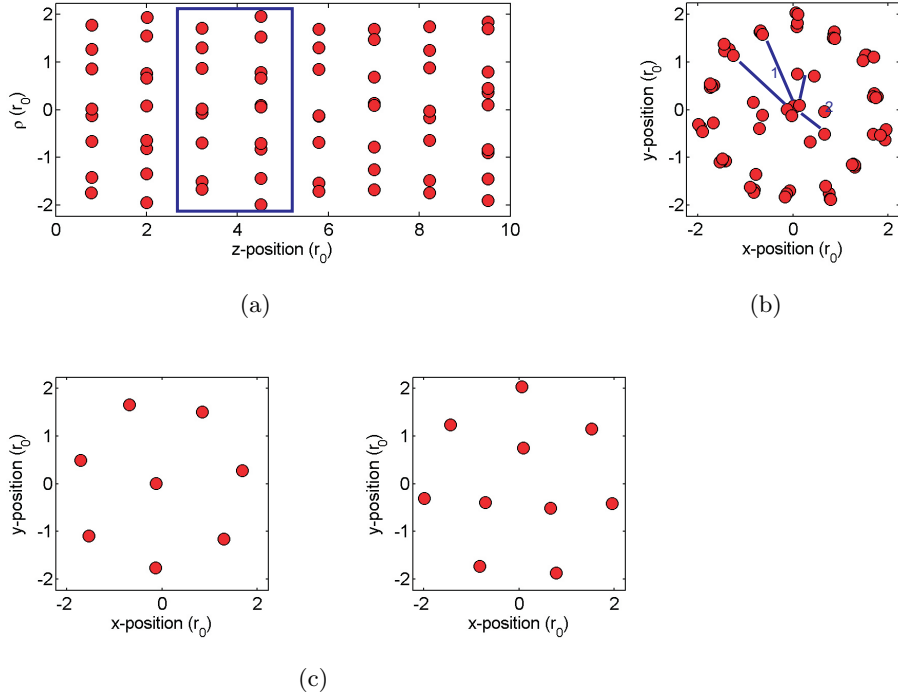


Figure 4.5.: Ground state configuration $[(1, 7); (3, 7)]$ with a rotation angle $[(0^\circ, 0^\circ); (0^\circ, 0^\circ)]$. The example for this configuration is chosen for a length density of $\rho_L = 6.8$ and Coulomb interaction ($\kappa = 0.0$). The view from the side (a) shows that each layer consists of 8 particles for the first layer and 10 particles for the second layer, while the integrated view from top (b) shows 14 positions of particles on the outer shell, 3 positions for the inner shell and the center particle. Therefore, the unit cell consisting of 2 layers with 8 and 10 particles, as seen in (c), where both layers have an outer shell population of 7 particles, which are rotated by $\approx 26^\circ$. The other particles are not rotated within the unit cell.

shows an example of a ground state configuration for a length density of $\rho_L = 6.8$ and a screening value of $\kappa = 0.0$. Since this is a Coulomb interacting system, the Ewald summation technique was applied to calculate the energy. The ground state configuration is $[(1, 7); (3, 7)]$ and the figure shows a simulation snapshot at a very low temperature ($\Gamma_C = 10000$). The length density of $\rho_L = 6.8$ was simulated for different typels (N, L_z) but this example is for $N = 68$ and $L_z = 10.0r_0$. The view from the side 4.5(a) shows 8 layers on the length of $10r_0$, containing alternating 8 and 10 particles each. Here, the first problem in simulating these systems becomes obvious. For this tupel ($N = 68, L_z = 10.0$) the ground state configuration of alternating layers (1, 7) and (3, 7) there is no

4. Yukawa tubes

integer solution for the number of layers. Therefore there are defects, in this case two layers with just 7 particles. The integrated view from top 4.5(b) shows 14 positions on the outer shell, meaning that the 7 particles of the outer shells of the different layers (1, 7) and (3, 7) are rotated by $\approx 26^\circ$. Interestingly, the 360° of the full circles cannot be divided by the 14 positions with an integer solution. The inner shell shows 3 positions and an additional center particle. These particles are not rotated, neither within the unit cell nor between the units cells.

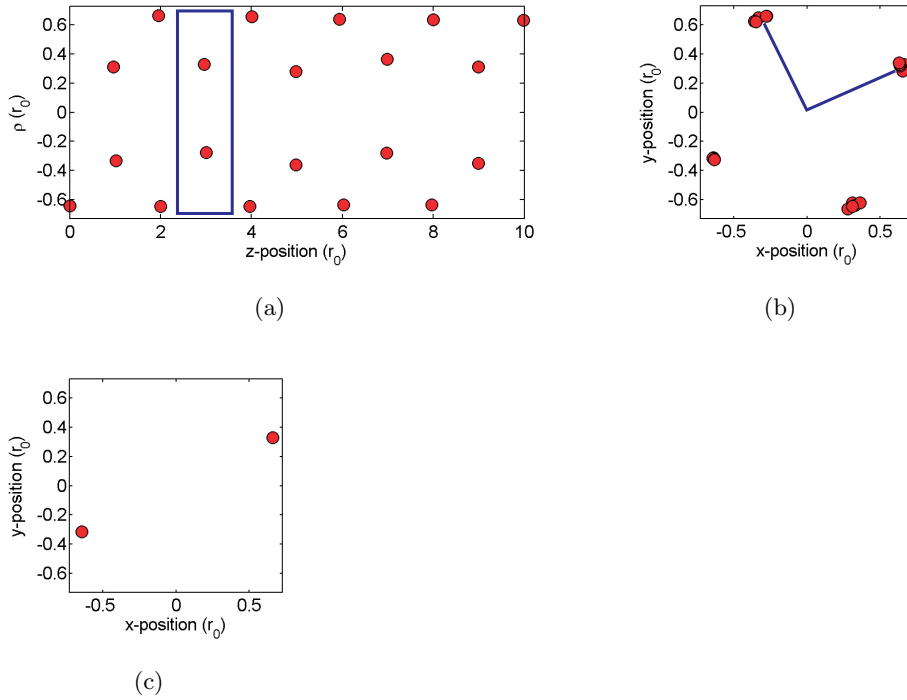


Figure 4.6.: Ground state configuration $[(2)]$ with a rotation angle $[(90^\circ)]$. The example is chosen for a length density of $\rho_L = 2.0$ and a screening parameter of $\kappa = 0.5$, but this configuration also applies to the same configurations given in figure 4.19 and appendix C.1, e.g. $2.0 < \rho_L < 3.45$ and $\kappa = 1.0$. Subfigure (a) shows the view from the side and one can see that the particles are arranged in layers of 2 particles each, while subfigure (b) shows the integrated view from top along the simulation box. Since this view shows 4 positions of particles, it is clear that the unit cell, seen in (c), of 2 particles is rotated by 90° resulting in the notation of the ground state configuration of $[(2)],[(90^\circ)]$.

At low length densities the Yukawa tubes are a 1-dimensional chain of parti-

4.2. Structural properties

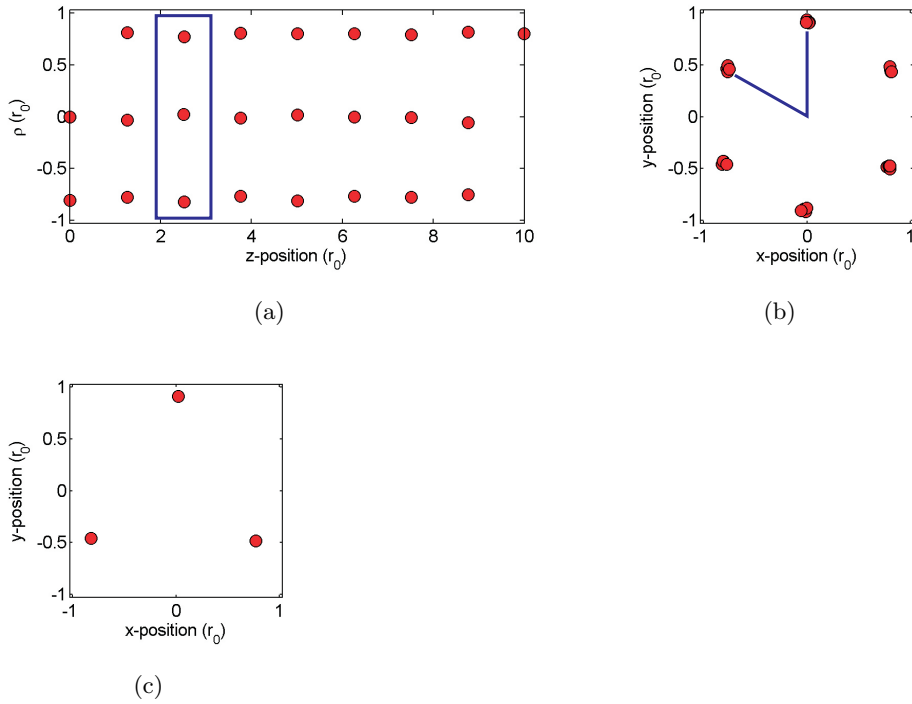


Figure 4.7.: Ground state configuration [(3)] with a rotation angle [(60°)]. The example for this configuration is chosen for a length density of $\rho_L = 2.4$ and Coulomb interaction ($\kappa = 0.0$). The view from the side (a) shows that each layer consists of 3 particles, while the integrated view from top (b) shows 6 positions of particles. Therefore, the unit cell, seen in (c), of 3 particles is rotated by 60° from layer to layer.

cles. This line is performing a zig-zag transition [160] at higher length densities just before Yukawa tubes as 3-dimensional systems are recognized. The easiest system is given in figure 4.6. This ground state configuration of [(2)] is given for a length density of $\rho_L = 2.0$ and a screening parameter of $\kappa = 0.5$. The view from the side 4.6(a) shows 10 layers of 2 particles each. Since the integrated view from top 4.6(b) shows 4 positions, the unit cell of 2 particles is rotated by 90° to the next unit cell. In this case the total number of particles divided by the number of particles in the unit cell is an integer and therefore no defects are seen. The same holds true for the examples of the next ground state configurations with only one shell [(3)], [(4)] and [(5)]. Figure 4.7 shows the ground state configuration [(3)] for $\rho_L = 2.4$ and a screening $\kappa = 0.0$. There are 8 layers with 3 particles each seen in the view from the side 4.7(a), while the view from top shows 6 positions. This implies that the unit cell 4.7(c) is rotated by 60°.

4. Yukawa tubes

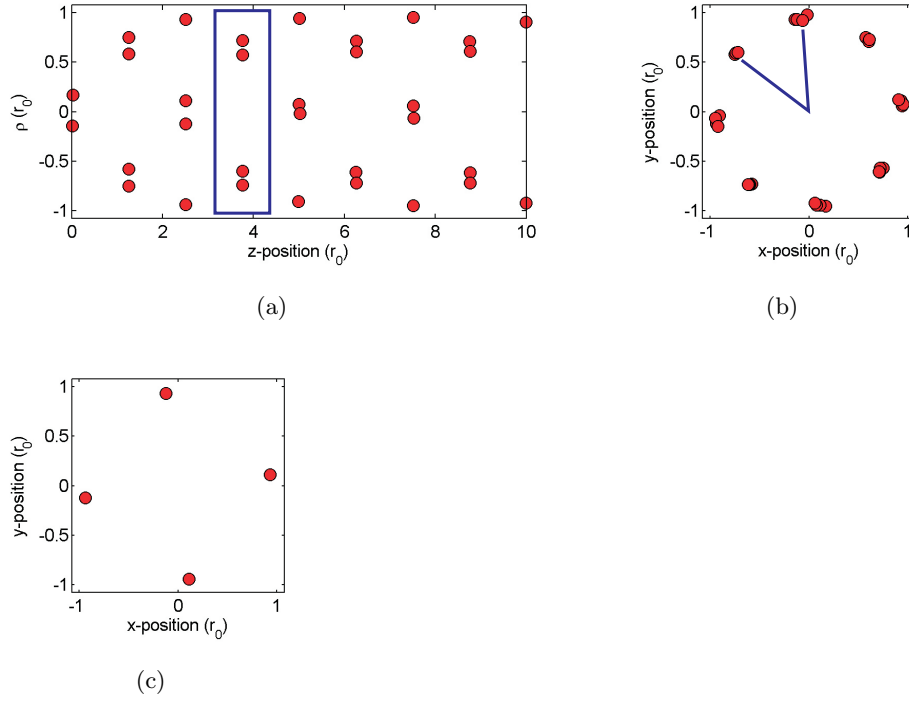


Figure 4.8.: Ground state configuration [(4)] with a rotation angle [(45°)]. The example for this configuration is chosen for a length density of $\rho_L = 3.2$ and a screening parameter of $\kappa = 0.5$. The view from the side (a) shows that each layer consists of 4 particles, while the integrated view from top (b) shows 8 positions of particles. Therefore, the unit cell, seen in (c), of 4 particles is rotated by 45° from layer to layer.

Also figure 4.8 shows no defects in the snapshots. The view from the side 4.8(a) also shows 8 layers with 4 particles each. The integrated view from top 4.8(b) displays 8 positions, which means that the unit cell 4.8(c) is rotated by 45°.

Although also the example for the ground state configuration [(5)] in figure 4.9 shows no defects, it is a good example for another challenge. From the view from the side 4.9(a) it is hard to determine layers as easy as in the previous examples. The integrated view from top 4.9(b) shows that 5 positions are used. But the unit cell splits into sublayers of 2 and 3 particles which is the reason for the challenge in determining the layers in the sideview. The example is given for $\rho_L = 3.5$ and $\kappa = 0.5$ which results into a system without defects. From the sideview one can also imagine that the system looks very similar to a helix since every particle is rotated by 72° and also displaced in the z -direction by

4.2. Structural properties

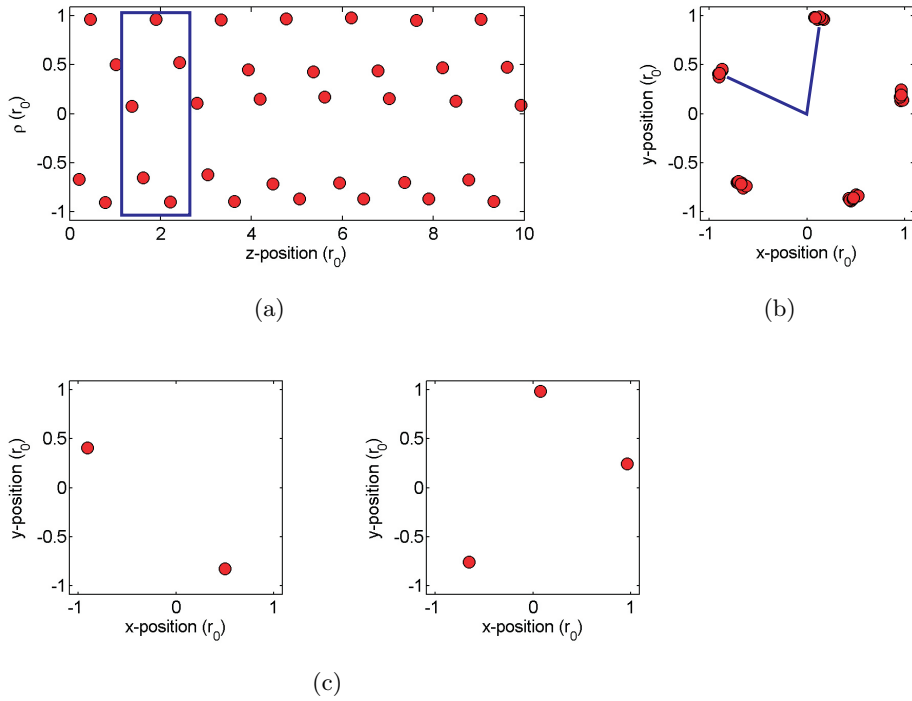


Figure 4.9.: Ground state configuration $[(5)]$ with a rotation angle $[(0^\circ)]$. The example for this configuration is chosen for a length density of $\rho_L = 3.5$ and a screening parameter of $\kappa = 0.5$. The view from the side (a) shows that it is hard to define layers here, but a possible unit cell consists of 5 particles and the view from top again shows only 5 particles and therefore the next cell is not rotated. However, the algorithm that tried to calculate the unit cell shows in (c) that the unit cell has a substructure of a 2 and 3 particle layer. After a layer consisting of two sublayers with 2 and 3 particles the cell repeats itself, starting with a sublayer of 2 particles again.

some distance. Helices are a quite common configuration in nature. Molecules, DNA and now Yukawa tubes often have a helix like structure since they make optimal use of the given space [161]. The ground state configuration $[(6)]$ also makes use of this type of configuration.

The first configuration with two layers is $[(1); (5)]$. Figure 4.10 shows an example of this configuration for $\rho_L = 5.9$ and $\kappa = 2.0$. The view from the side 4.10(a) shows 19 layers with alternating 1 and 5 particles, but since the 59 particles cannot be distributed only in layers of 1 and 5 particles there are defects as well. At some point the layer with 1 particle is missing. Despite that, the view from top 4.10(b) shows evenly distributed particles on 10 positions on the

4. Yukawa tubes

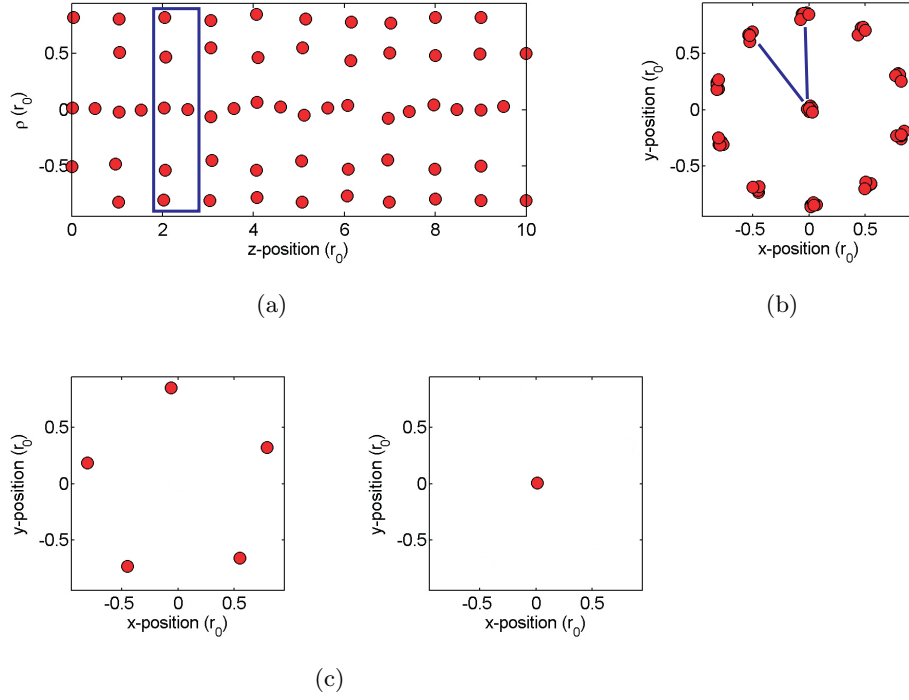


Figure 4.10.: Ground state configuration $[(1);(5)]$ with a rotation angle $[(0^\circ);(36^\circ)]$. The example for this configuration is chosen for a length density of $\rho_L = 5.9$ and a screening parameter of $\kappa = 2.0$. The view from the side (a) shows that the layers consists of 5 particles and the next layer only of a center particle, while the integrated view from top (b) shows 10 positions of particles on the outer shell and a center particle. Therefore, the unit cell, seen in (c), of 5 particles on the outer shell and 1 particle in the center of the next layer is rotated by 36° for the outer shell and arbitrarily for the center particle.

outer shell and a center particle. The unit cell consists of two layers with 1 and 5 particles and the 5 particle layer is rotated by 36° to the next unit cell. The smallest length density at which this two-layer-configuration can be observed as a ground state configuration is $\rho_{L,crit.} = 3.6$ (at $\kappa = 0.0$). The example of the ground state configuration $[(1);(6)]$ in figure 4.11 deviates in the type of defects that occur. The example is chosen for $\rho_L = 4.4$ and $\kappa = 0.0$. Since the unit cell 4.11(c) consists of two layers with 1 and 6 particles and here, again, 44 particles were used at a length $L_z = 10r_0$, defects are needed to distribute the total number of particles. In this case, there are layers with 7 particles on the outside instead of 6. A result of these defects is the integrated view from top 4.11(b), where no clearly distinct positions can be observed. Nevertheless, apart

4.2. Structural properties

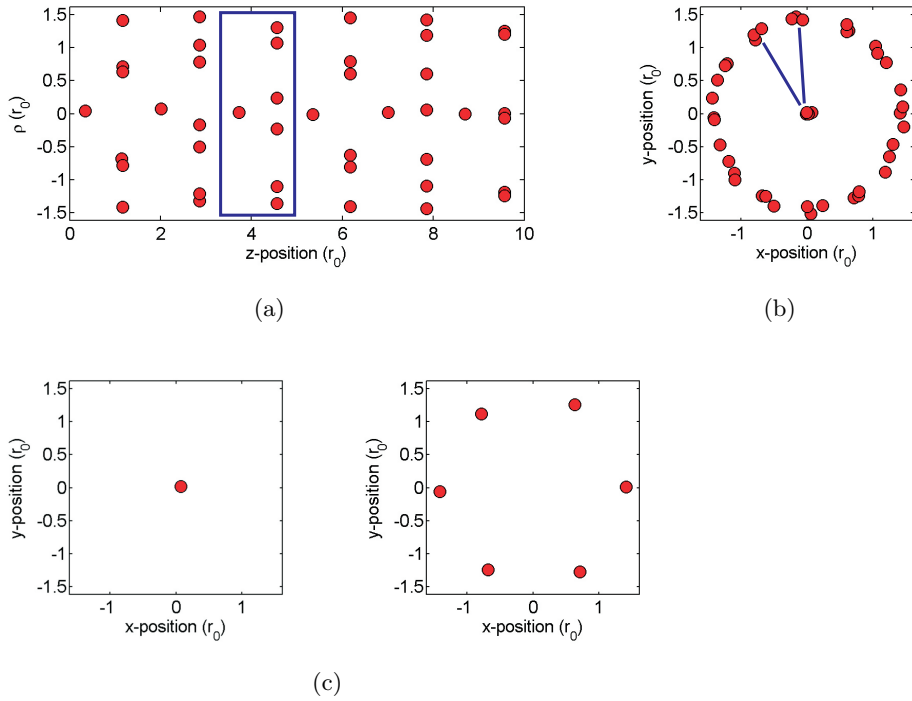


Figure 4.11.: Ground state configuration $[(1); (6)]$ with a rotation angle $[(0^\circ); (30^\circ)]$. The example for this configuration is chosen for a length density of $\rho_L = 4.4$ and Coulomb interaction ($\kappa = 0.0$). The view from the side (a) shows that the layers consists of 6 particles and the next layer only of a center particle, while the integrated view from top (b) shows 12 positions of particles on the outer shell and a center particle. Therefore, the unit cell, seen in (c), of 6 particles on the outer shell and 1 particle in the center of the next layer is rotated by 30° for the outer shell and arbitrarily for the center particle. The algorithm that determines the unit cells has found a different unit cell though, because it is close ($\rho_{L,crit.} = 4.55$) to another ground state configuration and in this regime not only one kind of cells are existing but also “defects” with other layer configurations, here $(7, 0)$. This is also the reason why the integrated view from top (b) does not clearly show the 12 positions of the particles.

from the defects the layers with 6 particles are rotated by 30° to fill 12 positions.

The next example is given for the first configuration with two shells in one layer. Figure 4.12 displays an example for the ground state configuration $[(1, 6)]$ for $\rho_L = 5.2$ and $\kappa = 0.0$. Despite some defects, seen in the view from top 4.12(b) this example consists of 8 layers with 7 particles each. The unit cell

4. Yukawa tubes

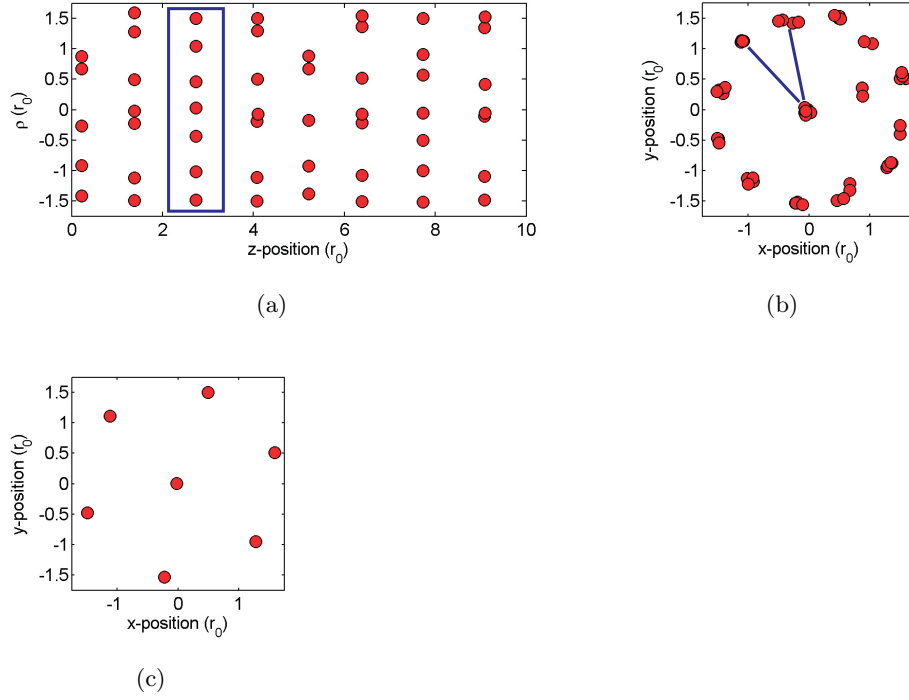


Figure 4.12.: Ground state configuration $[(1, 6)]$ with a rotation angle $[(0^\circ, 30^\circ)]$. The example for this configuration is chosen for a length density of $\rho_L = 5.2$ and Coulomb interaction ($\kappa = 0.0$). The view from the side (a) shows that each layer consists of 7 particles, while the integrated view from top (b) shows 12 positions of particles on the outer shell and 1 center particle. Therefore, the unit cell, seen in (c), of 6 particles on the outer shell and 1 particle in the center is rotated by 30° for the outer shell and arbitrarily for the center particle.

4.12(c) consists of two shells with 6 particles on the outer shell and a center particle. The particles on the outer shell are rotated by 30° to the next unit cell.

The configuration $[(1); (1, 7)]$ is the first ground state configuration which combines two layers and two shells. The example in figure 4.13 is given for $\rho_L = 6.5$ and $\kappa = 0.5$. The view from the side 4.13(a) displays 14 layers with alternating 1 and 8 particles. The only defect is that one layer with a single central particle is missing and therefore the view from top 4.13(b) shows 14 clearly distinct positions used by particles. Again (cf. figure 4.5) a configuration where the outer shell is filled with 7 particles despite the impossibility to distribute the particles by an integer angle on the outer shell. The unit cell 4.13(c) consists of two layers, where the first layer only contains one central

4.2. Structural properties

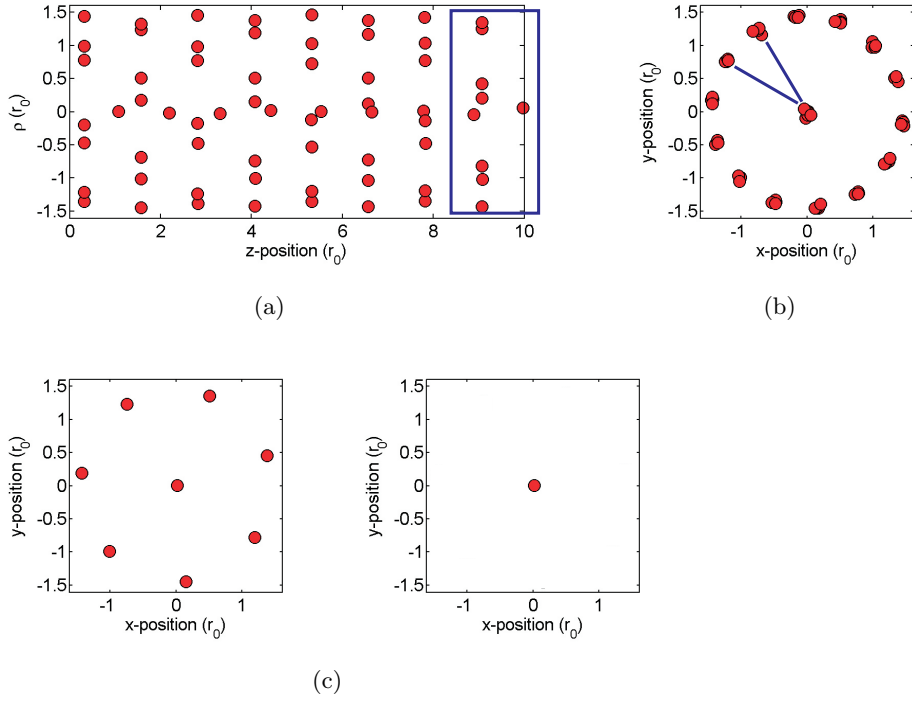


Figure 4.13.: Ground state configuration $[(1); (1, 7)]$ with a rotation angle $[(0^\circ); (0^\circ, 26^\circ)]$. The example for this configuration is chosen for a length density of $\rho_L = 6.5$ and a screening parameter of $\kappa = 0.5$. The view from the side (a) shows that the layers consist of alternating 1 particle and 8 particles, while the integrated view from top (b) shows 14 positions of particles for the outer shell and a center particle. Therefore, the unit cell, seen in (c), of 6 particles on the outer shell and 1 particle in the center of the next layer is rotated by $\approx 26^\circ$ for the outer shell and arbitrarily for the center particle.

particle and the next layer two shells where the 7 particles on the outer shell are rotated by $\approx 26^\circ$ to the next unit cell.

The groundstate configuration $[(2, 8)]$ as seen in figure 4.14 has the special feature that the unit cell 4.14(c) splits into two subshells of $(1, 4)$. The particles on the inner shell form a zig-zag line that is twisted by 180° between the two subshells. Therefore the view from top 4.14(b) displays two positions with particles on the inner shell and 8 positions with particles on the outer shell, since the 4 particles on the subshells are also rotated by 45° . The length density for this example is $\rho_L = 6.8$ and the screening parameter is $\kappa = 0.5$. Although the configuration $[(2, 9)]$ does not look different by the unit cell definition, it

4. Yukawa tubes

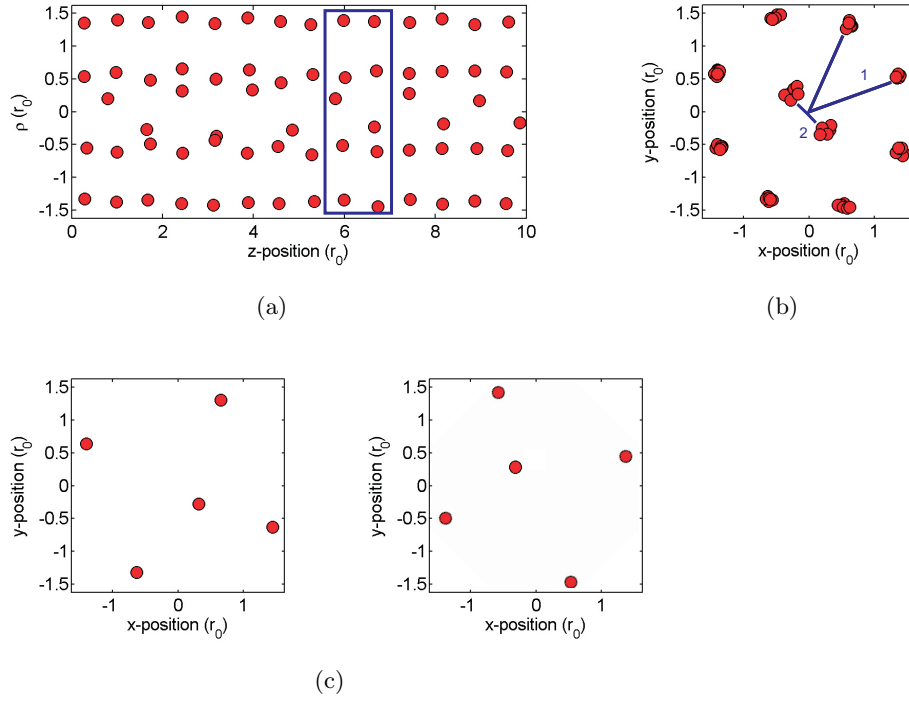


Figure 4.14.: Ground state configuration $[(2, 8)]$ with a rotation angle $[(0^\circ, 0^\circ)]$. The example for this configuration is chosen for a length density of $\rho_L = 6.8$ and a screening parameter of $\kappa = 0.5$. The view from the side (a) shows that each layer consists of 5 particles, while the integrated view from top (b) shows 8 positions of particles on the outer shell and 2 positions on the inner shell. Therefore, the unit cell, seen in (c), of 4 particles on the outer shell and 1 particle on the inner shell (not in the center) is rotated by 45° for the outer shell and 180° for the inner shell. Normally the notation for this ground state would be $[(1, 4)], [(180^\circ, 45^\circ)]$, but in order to fit in the series of ground states two layers were combined to one, so that the unit cell consists of one layer (with 2 sublayers) with 8 particles on the outer shell and 2 particles on the inner shell.

is different when looking at the view from top 4.15(b). Not only are the two particles on the inner shell rotated by 90° between the unit cells to fill the 4 positions seen, but also the shape of the outer shell is not a perfect circle. The structure of the inner shell, a square, is also showing on the outer shell. The view from top 4.14(b) shows 18 positions with particles on the outer shell and the structure is in the transition between a circle and a square. Also, in this example there are quite a few defects with layers with only 2 particles (on the inner shell).

4.2. Structural properties

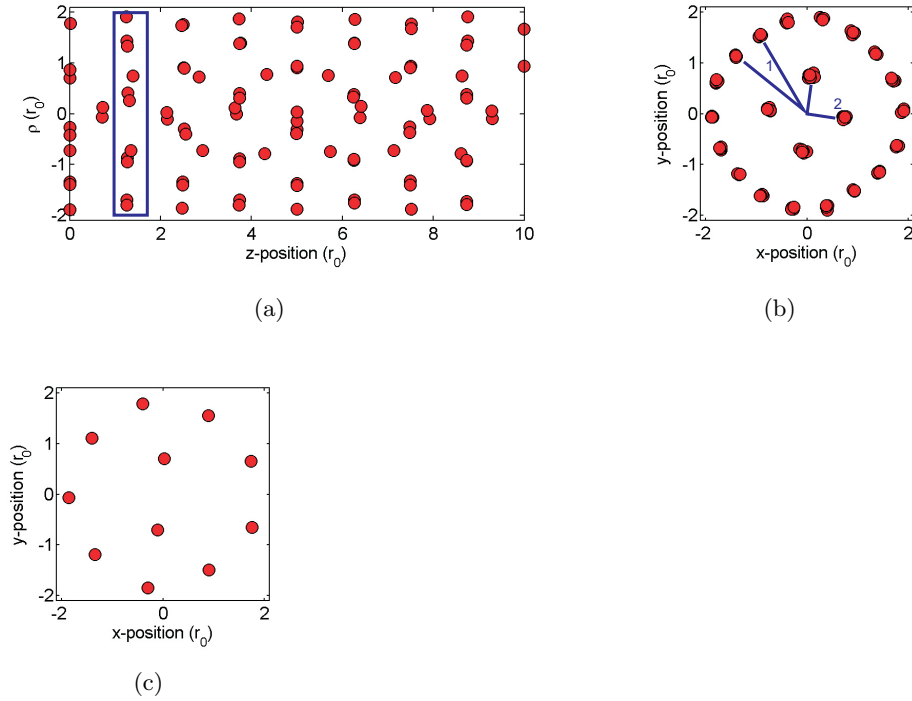


Figure 4.15.: Ground state configuration $[(2,9)]$ with a rotation angle $[(90^\circ, 20^\circ)]$. The example for this configuration is chosen for a length density of $\rho_L = 10.0$ and a screening parameter of $\kappa = 0.5$. The view from the side (a) shows that each layer consists of 11 particles, while the integrated view from top (b) shows 18 positions of particles on the outer shell and 4 positions on the inner shell. Therefore, the unit cell, seen in (c), of 9 particles on the outer shell and 2 particles on the inner shell is rotated by 20° for the outer shell and 90° for the inner shell.

Figure 4.16 combines two different structures in its ground state configuration of $[(2); (2,8)]$. The view from the side shows 17 layers with alternating 2 and 10 particles each. Since the length density of $\rho_L = 9.0$ is realized with $N = 90$ particles at $L_z = 10.0r_0$ there are some defects in this example, namely layers with 2 particles on the inner shell. The result is given in the view from top 4.16(b) where 16 positions filled with particles are seen for the outer shell but not clearly distinct positions for the inner shell are observed. The inner shell here is a helix like structure again, where the two particles on the inner shell are rotated by some smaller angle. In other examples of this ground state configuration the inner structure is made of 4 positions though. The given unit cell 4.16(c) also shows that in general the angle between the particles on the

4. Yukawa tubes

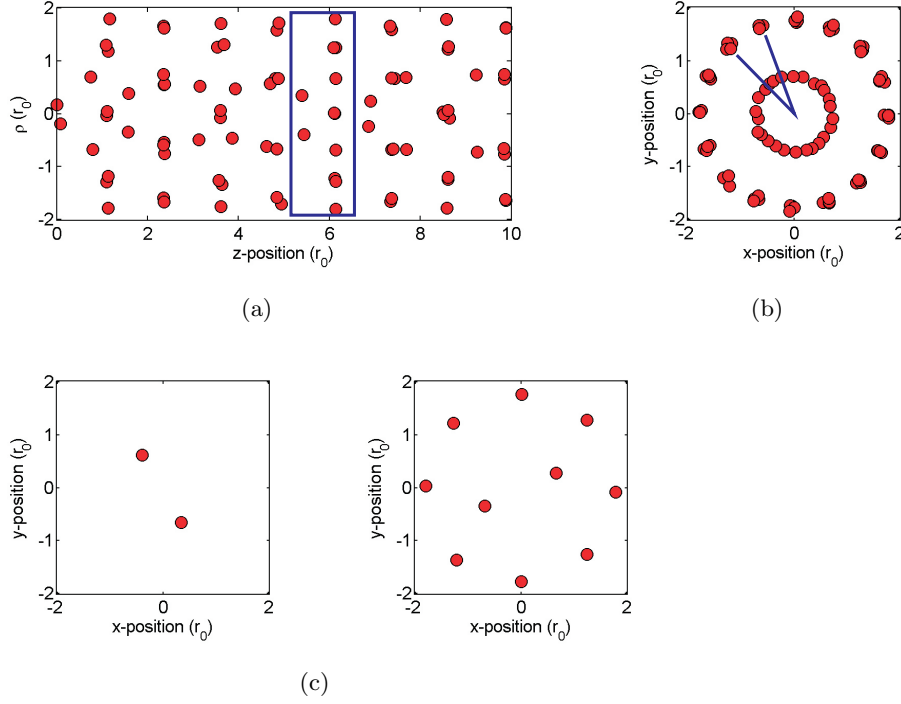


Figure 4.16.: Ground state configuration $[(2); (2, 8)]$ with a rotation angle $[(0^\circ); (0^\circ, 22.5^\circ)]$. The example for this configuration is chosen for a length density of $\rho_L = 9.0$ and a screening parameter of $\kappa = 0.5$. The view from the side (a) shows that the layers consist of alternating 2 and 10 particles, while the integrated view from top (b) shows 16 positions of particles on the outer shell. The number of positions on the inner shell cannot be clearly determined in this view (b), since there exist other layers with different inner shell population. Nevertheless, the unit cell, seen in (c), of 8 particles on the outer shell of the second layer and 2 particles on the inner shell of both layers is rotated by 22.5° for the outer shell. The 2 particles of each layer are rotated by 90° against each other, so that there is no rotation angle between the unit cells for the inner shell. In this example the inner structure is not a square since the 2 particles have a slightly smaller rotation angle which results in a helix-like structure.

inner shell is 90° . Therefore, after the 100 MC runs to find the ground state configuration, it is unclear if this configuration is the correct ground state for this length density and screening. An even more dubious example is given in figure 4.17. The ground state configuration as determined by the algorithm to find distinct layers is $[(2, 3); (1, 5)]$ for $\rho_L = 8.3$ and $\kappa = 0.5$. From the unit cell 4.17(c) it is arguable that the correct definition would be $[(3, 8)]$ which is

4.2. Structural properties

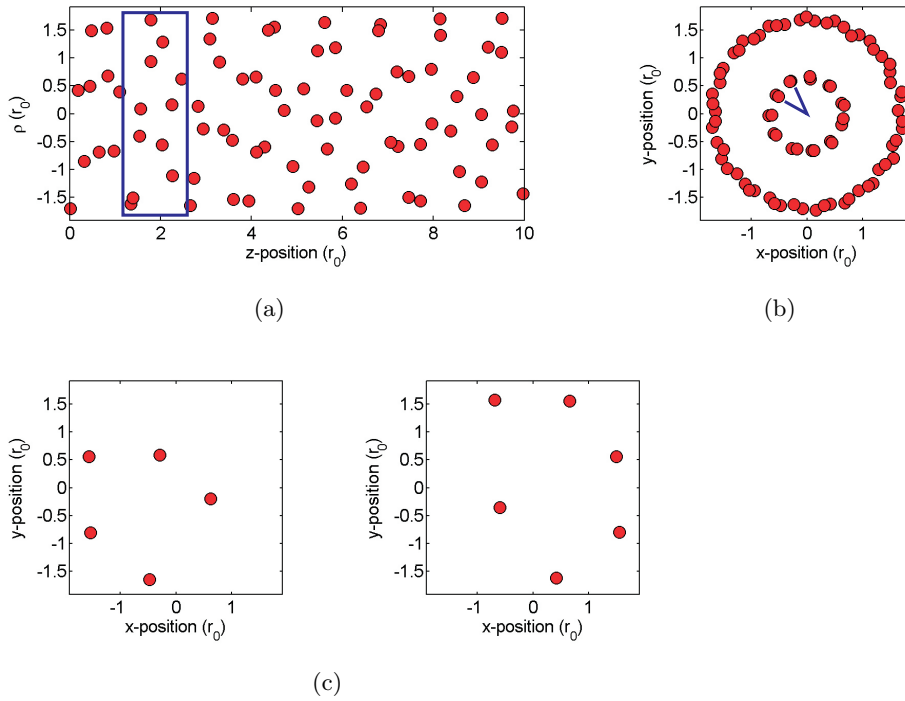


Figure 4.17.: Ground state configuration $[(2, 3); (1, 5)]$ with a rotation angle that cannot be determined due to other configurations in other layers of the system. The example for this configuration is chosen for a length density of $\rho_L = 8.3$ and a screening parameter of $\kappa = 0.5$. The view from the side (a) shows no clear layers structure and also the integrated view from top (b) shows no clear positions for the outer shell. For the inner shell 11 positions are observed. Therefore both rotation angles could not be determined (cf. appendix C.1).

splitted into two subshells with the above configurations. Here, the inner shell in the integrated view from top 4.17(b) displays 11 positions with particles. The outer shell is also a helix like structure. Although the number of MC runs to find the ground state configuration has been increased to 500 for this length density and screening no state with a smaller energy could be found although from the look at this example it is reasonable to say there is a configuration with a lower energy. Nevertheless, it shows how complicated it is to find the correct ground state in these systems. Figure 4.18 shows a similar structure of subshells. The ground state configuration $[(1, 5); (2, 5)]$ is given for $\rho_L = 9.6$ and $\kappa = 1.0$. From the view from the side 4.18(a) no clearly distinct layers can be seen, while the view from top 4.18(b) at least for the outer shell show 20 distinct positions with particles. This results in a rotation angle of 9° for the

4. Yukawa tubes

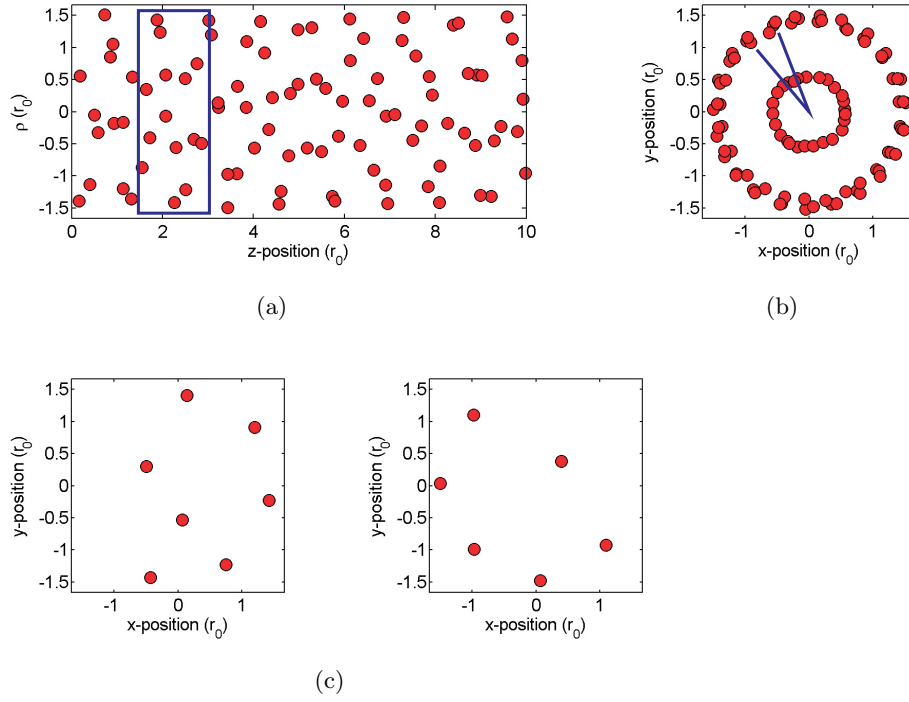
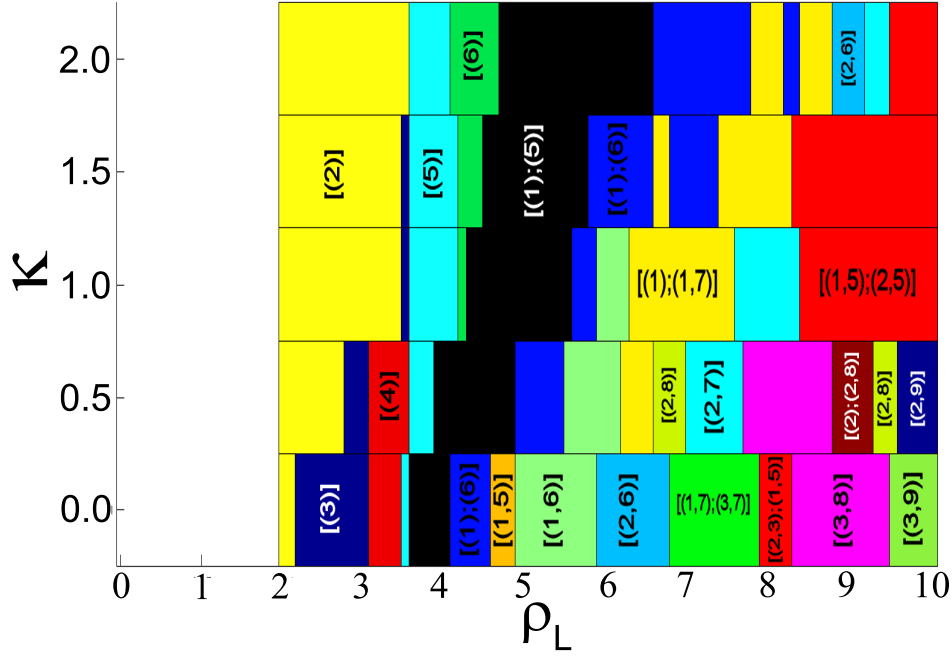


Figure 4.18.: Ground state configuration $[(1, 5); (2, 5)]$ with a rotation angle $[(x^\circ, 9^\circ); (x^\circ, 9^\circ)]$. The example for this configuration is chosen for a length density of $\rho_L = 9.6$ and a screening parameter of $\kappa = 1.0$. The view from the side (a) shows no clear layer structure, while the integrated view from top (b) shows 20 positions of particles on the outer shell. The number of positions on the inner shell cannot be clearly determined in this view (b). Nevertheless, the unit cell, seen in (c), of 5 particles on the outer shell of both layers and 1 and 2 particles on the inner shell of the layers is rotated by 9° for both outer shells. The 5 particles of each layer are rotated by 18° against each other, so that in total 20 positions can be reached by the 5 particles on the outer shell.

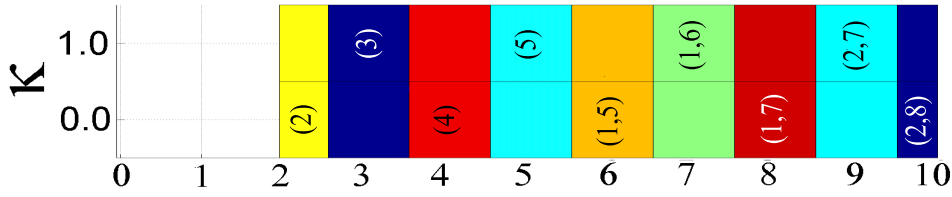
outer shells of the sublayers.

General trends

Figure 4.19 summarizes the results of the ground state configurations obtained with these Monte Carlo simulations. Contrary to the Yukawa balls the increase of screening leads first to an increase of the number of layers (for a fixed length) instead of an increase of the inner shell population. Here, the highest inner shell population has the Coulomb configuration. This means, that the same configuration as in the Coulomb case will be found at higher length densities with



(a)



(b)

Figure 4.19.: (a) Ground state configurations of Yukawa tubes as a function of length density ρ_L and screening κ . Different configurations are given in color. For comparison the ground state configurations for 2d dust systems [22, 159] are shown in (b).

higher screenings. With the general trends of the Yukawa balls in mind this is at first counterintuitive, but here the density increases first in the z -dimension before it is increased in the radial direction. Another general trend here is, that at first the layers are alternating, e.g. $[(1); (6)]$ at $(\rho_L = 5.2, \kappa r_0 = 0.5)$, before they merge into one layer with a bigger spacing between the layers, e.g. $[(1, 6)]$ at $(\rho_L = 5.8, \kappa r_0 = 0.5)$. Exceptions to this trend are also found. With increased screening at a fixed length density of $\rho_L = 4.1$ the ground state configuration changes from $[(5)]$ at $\kappa r_0 = 1.5$ to $[(6)]$ at $\kappa r_0 = 2.0$, while $[(6)]$ is the ground

4. Yukawa tubes

state configuration at $\kappa r_0 = 1.5$ only for length densities of $\rho_L \geq 4.15$. A clearer case of this exception can be found at a length density of $7.65 \leq \rho_L \leq 8.25$ and screenings of $\kappa r_0 = 0.0$ to 0.5 .

It should also be mentioned that at the borders of the structural transitions the configurations are not easily determined. The number of layers for a unit cell often increases due to a alternating layer configuration, for example in the transition region from $[(1); (6)]$ to $[(1, 6)]$ the configuration with the lowest energy as calculated by the simulations is something like $[(1); (6); (1); (1, 6); (1); (1, 6); (1); (6)]$ or a similar combination of layers. Here, grandcanonical simulations are needed to determine the ground state configuration with higher accuracy.

Examples of the ground state configurations of figure 4.19 are given in the figures 4.4, 4.5 and 4.6-4.18. The first image of each subfigure shows the lateral view of the configuration, the second the integrated view from the top and the third image shows the top view of each layer of the unit cell of this configuration. The actual ground state configuration may slightly differ from the given example since the rotation angle between the unit cells can vary and close to the transition points the configurations are not as clear as these examples.

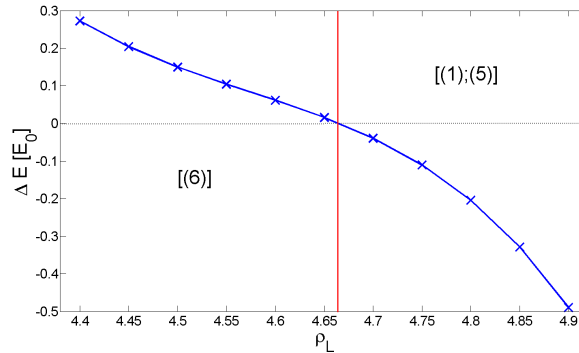


Figure 4.20.: Energy difference between the states $[(6)]$ and $[(1); (5)]$ at a screening value of $\kappa = 2.0$ calculated by MD simulation by variation of the length density only. The critical length density for the structural transition between the states is calculated as $\rho_L \approx 4.65$.

For the table in appendix C.1 the critical length densities of structural transitions of the ground state configuration have been computed. As mentioned before, in the transition region between two ground state configurations for fixed screening and varying length density the layer configurations are alternating between the two configurations arbitrarily due to the limitations of the simulation method used. In order to determine the critical transition point

nevertheless, molecular dynamics simulations have been performed in the following way. Both ground state configurations have been used and the length density was varied only by changing the layer distance d_l (cf. figure 4.3). For those length densities the energies have been calculated and compared to the other configuration in question. Figure 4.20 shows the energy difference and the determination of the critical length density. This critical length density was used in order to find the ranges of length densities in figure 4.19 in which the configurations exists as ground state configurations.

4.3. Other anisotropic systems

An intermediate system between Yukawa balls and Yukawa tubes is a system where the particles are not isotropically confined,

$$H(\mathbf{r}_1 \dots \mathbf{r}_N, \mathbf{p}_1 \dots \mathbf{p}_N) = \sum_{i=1}^N \frac{\mathbf{p}_i^2}{2m} + \sum_{i=1}^N \frac{\alpha}{2} (x_i^2 + y_i^2 + \gamma z_i^2) + \frac{1}{2} \sum_{i \neq j}^N \frac{q^2}{4\pi\epsilon r_{ij}} \cdot e^{-\kappa r_{ij}}. \quad (4.9)$$

When the trap frequencies are equal, $\gamma \rightarrow 1$, it is again the Hamiltonian (3.1) for the Yukawa balls and if $\gamma \rightarrow 0$ the Hamiltonian (4.1) is obtained. This system has been studied in detail for Coulomb interaction [90, 162, 163] as a function of γ . For smaller particle numbers a line of particles in the center is seen, as were found in section 4.2.2 for $3.55 \leq \rho_L \leq 5.85$. Reference [90] also found that the anisotropy parameter γ can drive the system to undergo first and second order structural phase transitions. For small anisotropies multiple ring structures, which in this work were named layers for the Yukawa tubes, and also a complicated fine structure were observed.

The melting processes have not yet been studied, although from the normal mode analysis of [90] it was assumed that the multiple ring structures, or layers, must be of relevance to the melting process. Indeed, from the study of the structures of the Yukawa tubes it can be assumed that the melting process again, as in the Yukawa ball case, will heavily depend on the configuration and the melting will be much different radially than along the z -direction. For some specific combinations of κ and ρ_L the inner particles can even be moved without additional thermal energy along the z -direction.

The system (4.9) can also be studied experimentally when slightly alternating the power of the rf-electrode. In this case, not spherically symmetric Yukawa balls are formed by the dust particles but instead oblate and elongated struc-

4. Yukawa tubes

tures are observed. In principle it should be possible to enhance this setup to study Yukawa tubes. An open elongated glass box instead of the cube like glass box in the experiment [32] can possibly change the trap so that Yukawa tubes alike dust crystals can be investigated. This can also be of interest for the understanding and manipulation of carbon nanotubes [164, 165] or similar structures, like TiO_2 nanotubes [166].

5. Discussion

5.1. Summary

The aim of this thesis was to study structural and thermodynamic properties of Wigner crystals composed of dust particles in a plasma. The properties are strongly influenced by finite size effects, i.e. the number of particles, and the interaction potential. In order to understand the complexity of the structural and dynamical properties of those systems extensive computer simulations were performed.

The structural properties were first investigated by analyzing the ground state configurations and their dependence on the screening and number of particles in the system. Very detailed molecular dynamics and Monte Carlo simulations were compared against the experimentally observed Yukawa balls. Deviations in the shell population of the experimentally observed clusters to clusters in the simulations with unscreened interaction potential made it inevitable to assume a screened interaction to be present in the experiment. Other effects, namely charge fluctuations and finite temperature effects in the vicinity of the experimental conditions could not explain the differences.

Investigations of the ground state configurations showed a general trend, that the inner shell population is increased with the increase of the screening. The clusters undergo structural transitions with the variation of the screening. Finite size effects were studied on the ground state configurations of mesoscopic Yukawa balls $N = 11, \dots, 60$. Here, the ground state configurations showed several anomalies to the general trend, for specific combinations of (N, κ) , correlated transitions of two particles instead of just one, the reduction of the inner shell population with the increase of the total particle number and reentrant configurations were observed. The reason are mechanically highly stable magic clusters, which form platonic bodies with perfect symmetry. These configurations are for mesoscopic systems often part of the ground state configurations and highly influence the stability.

The analysis of the radial potential energy barriers showed the expected result, that the potential energy barrier between the ground and metastable state with

5. Discussion

different shell population is lowered energetically in the vicinity of a structural transition. This can be a good first estimate to radial melting, since the particles have to overcome this barrier for a radial transition.

In experiments melting in the sense of radial transitions between shells is not seen frequently for mesoscopic Yukawa balls with $N < 40$. Although there are experiments observing such transitions they do not occur often. It is known that the temperature for a phase transition between a solid-like and a liquid-like state is decreased for smaller systems with an increased fraction of particles on the outer shell. For small systems it is observed that this trend is violated. Instead the very small systems analyzed here, $N = 11, \dots, 40$, showed the reverse trend, that the clusters with smaller total particle number are melting at a higher temperature.

To determine the different melting processes it is essential to choose sensitive parameters to this transition. A huge amount of works on melting of mesoscopic clusters are based on distance fluctuations between particles. Here it was shown that one has to be very careful with such melting parameters, because they can depend on the simulation time. A reasonable parameter for radial transitions can be the frequency of occurrence of the ground state configuration that showed similar behavior than the potential energy barrier heights. Nevertheless, there are more melting processes possible in the Yukawa balls. Intershell or radial melting is normally the process occurring at the highest temperature. The intrashell melting processes are in general observed at temperatures an order of magnitude lower than for the radial processes. Here the energy difference between metastable states is also much lower, the ground and metastable states only differ in the setup of particles on the same shell. A reasonable parameter to detect these melting processes is given by the variance of the block averaged relative distance fluctuations, although this parameter needs to be calibrated. Very extensive Monte Carlo simulations were performed to calculate the melting temperatures for mesoscopic Yukawa balls $N = 11, \dots, 40$. Again the melting of mesoscopic clusters is dominated by the effects of magic clusters.

The comparison of the ground state configurations from the simulations with the observed shell populations of Yukawa balls in the experiment made it possible to determine the expected range for the screening in the experiment, $\kappa = 0.87 \pm 0.32$. The calculated potential energy barriers in the simulation and the observed particle trajectories made it possible to estimate a temperature in the experiment, $T = 0.00185 \pm 0.00065$.

The Yukawa tubes can become an object of research interest due to their similarity to carbon nanotubes. Detailed Monte Carlo simulations were performed in order to determine the ground state configurations for systems with length densities $2.0 \leq \rho_L \leq 10.0$ and screenings $\kappa = 0.0, 0.5, \dots, 2.0$. The complexity of the configurations is enormous and a small change in the length density or the screening can change the structure much. The ground state configurations in general were layers of $2d$ dust crystals, but the huge amount of metastable states ranged from twisted helica to bulk like structures.

5.2. Outlook

It is necessary to continue the investigation of ground state configurations as well as the thermodynamic properties of Yukawa balls to get more insight into the melting processes. For the studied range of particle numbers it was shown that finite size effects, i.e. magic clusters, dominate the dynamical processes. It will be interesting to analyze the melting in the intermediate region of particle numbers, supposedly $50 \leq N \leq 150$, where the small size effects slowly vanish and the trend of increasing melting temperatures with increased particle numbers starts.

It is also useful to extend the simulations in order to compare the results with experimental observations. Already, from the estimated values for the screening and the temperature in the experiment, together with the computed ground state configurations as well as the melting temperatures, it is possible to specify additional clusters, where radial transitions might be observed. Such clusters are $N = 25, 27, 32$, with very small radial melting temperatures and $N = 26, 33, 34, 35, 40$ for melting temperatures in the same range as the cluster with $N = 31$ particles. This is interesting to study in order to determine the temperature of the dust particles in the experiment. It should also help to understand the strength of the damping in the experiment, which is a main factor for the configuration seen in the experiment.

For the determination of melting temperatures of mesoscopic systems it will be useful to find a parameter that lacks the drawbacks of the specific heat, where a huge number of independent samples are needed, or the variance of the block averaged relative distance fluctuations, which need to be calibrated with another parameter. For radial melting such a parameter can be the frequency

5. Discussion

of occurrence of the ground state configuration in comparison to the occurrence of other configurations but in general this should be a quantity that does not require knowledge about the ground state and metastable configurations. This can be autocorrelation times but further research is needed to confirm this.

For future research on Yukawa tubes it can be of interest to establish an experimental setup to observe these structures. It should be possible to modify the structure and therefore the dynamical properties in such an experiment easily by changing the length density or by laser excitation. With the help of a complete investigation of the ground state configurations in dependence on the length density it might even be possible to think of new nanomaterials that have similar behavior. At the current point of research the understanding of nanotubes is much better than of the Yukawa tubes but from a perspective point of view the Yukawa tubes are more interesting because of the easily changeable interaction by variation of the screening parameter.

A. Ground states of Yukawa balls

A.1. Structural transition points and anomalies of the first kind

Table A.1.: Table of structural transition points κ_{cr} , cf. figure 3.12). Bold values mark anomalies of the 1st kind, where the inner shell changes by two particles with increased screening (N fixed). The screening values displayed are the critical values (± 0.05) up to which the configuration given in the 3rd column remains the ground state. From reference [87].

N	κ_{cr}	GS	N	κ_{cr}	GS	N	κ_{cr}	GS
11	1.9	(11, 0)	34	0.2	(30,4)	48	0.4	(39, 9)
	> 5.0	(10, 1)		> 5.0	(28, 6)		1.4	(38,10)
12	4.1	(12, 0)	35	0.3	(30, 5)		1.6	(36, 12)
	> 5.0	(11, 1)		3.2	(29, 6)	> 5.0	(35, 12, 1)	
13	> 5.0	(12, 1)		> 5.0	(28, 7)	49	0.2	(40, 9)
14	> 5.0	(13, 1)	36	3.6	(30,6)		1.1	(39,10)
15	> 5.0	(14, 1)		> 5.0	(28, 8)		1.4	(37, 12)
16	> 5.0	(15, 1)	37	1.7	(31, 6)	50	> 5.0	(36, 12, 1)
17	> 5.0	(16, 1)		4.2	(30, 7)		0.1	(41, 9)
18	> 5.0	(17, 1)		> 5.0	(29, 8)		0.7	(40,10)
19	4.6	(18, 1)	38	2.0	(32,6)		1.6	(38, 12)
	> 5.0	(17, 2)		> 5.0	(30, 8)		> 5.0	(37, 12, 1)
20	1.1	(19, 1)	39	0.2	(33, 6)	51	0.5	(41,10)
	> 5.0	(18, 2)		2.4	(32, 7)		1.1	(39, 12)
21	1.2	(20, 1)		3.6	(31, 8)		> 5.0	(38, 12, 1)
	> 5.0	(19, 2)		> 5.0	(30, 9)	52	0.3	(42,10)
22	0.3	(21, 1)	40	0.4	(34,6)		0.9	(40, 12)
	> 5.0	(20, 2)		> 5.0	(32, 8)	> 5.0	(39, 12, 1)	
23	1.4	(21, 2)	41	0.1	(35, 6)	53	0.2	(43,10)
	> 5.0	(20, 3)		0.6	(34, 7)		0.7	(41, 12)
24	1.0	(22, 2)		0.8	(33, 8)		2.9	(40, 12, 1)

Table A.1.: Table of structural transition points (contd.).

N	κ_{cr}	GS	N	κ_{cr}	GS	N	κ_{cr}	GS
	2.6	(21, 3)		> 5.0	(32, 9)		> 5.0	(39, 13, 1)
	> 5.0	(20, 4)	42	0.2	(35, 7)	54	0.0	(44,10)
25	0.3	(23, 2)		1.1	(34, 8)		0.6	(42, 12)
	2.2	(22, 3)		1.8	(33, 9)		1.7	(41, 12, 1)
	> 5.0	(21, 4)		> 5.0	(32, 10)		> 5.0	(40, 13, 1)
26	0.5	(24, 2)	43	0.7	(35, 8)	55	0.5	(43, 12)
	0.7	(23, 3)		3.6	(34, 9)		1.5	(42, 12, 1)
	> 5.0	(22, 4)		> 5.0	(33, 10)		1.6	(41, 13, 1)
27	1.0	(24, 3)	44	0.7	(36, 8)		56	> 5.0
	> 5.0	(23, 4)		1.5	(35, 9)	0.5		(44, 12)
28	0.1	(25, 3)	45	> 5.0	(34, 10)	57	1.0	(43, 12, 1)
	> 5.0	(24, 4)		0.5	(37, 8)		1.2	(42, 13, 1)
29	1.6	(25, 4)		1.2	(36, 9)		> 5.0	(41, 14, 1)
	> 5.0	(24, 5)	4.2	(35,10)	0.1		(45, 12)	
30	1.5	(26,4)	46	> 5.0	(32, 12, 1)	58	1.0	(43,12,1)
	> 5.0	(24, 6)		0.2	(38, 8)		> 5.0	(41, 14, 1)
31	1.56	(27, 4)		0.9	(37, 9)	59	1.0	(45,12,1)
	1.61	(26, 5)	3.3	(36,10)	> 5.0		(43, 14, 1)	
	> 5.0	(25, 6)	3.4	(34, 12)	0.5		(46, 12, 1)	
32	0.6	(28, 4)	47	> 5.0	(33, 12, 1)	60	0.9	(45, 13, 1)
	1.5	(27, 5)		0.5	(38, 9)		> 5.0	(44, 14, 1)
	> 5.0	(26, 6)		1.8	(37,10)	0.1	(48, 12)	
33	0.2	(29, 4)		2.1	(35, 12)		0.2	(47,12,1)
	0.6	(28, 5)		> 5.0	(34, 12, 1)		0.8	(45, 14, 1)
	> 5.0	(27, 6)					2.9	(44, 15, 1)
							> 5.0	(43, 16, 1)

A.2. Anomalies of the second kind

Table A.2.: Table of anomalies of the 2nd kind. Left column shows the change of the total particle number by one and column two the associated configuration change. The third and fourth column give the range of screening parameters where this transition occurs. From reference [87].

$N_1 \rightarrow N_2$	configuration	κ_{min}	κ_{max}
11 \rightarrow 12	(10, 1) \rightarrow (12)	1.9038	4.0567
20 \rightarrow 21	(18, 2) \rightarrow (20, 1)	1.0762	1.1906
25 \rightarrow 26	(22, 3) \rightarrow (24, 2)	0.2544	0.5049
26 \rightarrow 27	(22, 4) \rightarrow (24, 3)	0.7287	1.0412
30 \rightarrow 31	(24, 6) \rightarrow (27, 4)	1.4866	1.5623
30 \rightarrow 31	(24, 6) \rightarrow (26, 5)	1.5623	1.6142
33 \rightarrow 34	(28, 5) \rightarrow (30, 4)	0.2012	0.2450
34 \rightarrow 35	(28, 6) \rightarrow (30, 5)	0.2450	0.3034
35 \rightarrow 36	(28, 7) \rightarrow (30, 6)	3.1665	3.6133
36 \rightarrow 37	(28, 8) \rightarrow (30, 7)	3.6133	4.1646
37 \rightarrow 38	(30, 7) \rightarrow (32, 6)	1.6679	2.0283
38 \rightarrow 39	(30, 8) \rightarrow (32, 7)	2.0283	2.4396
39 \rightarrow 40	(32, 7) \rightarrow (34, 6)	0.2223	0.4179
39 \rightarrow 40	(31, 9) \rightarrow (32, 8)	3.6120	> 5.0000
40 \rightarrow 41	(32, 8) \rightarrow (34, 7)	0.4179	0.5521
41 \rightarrow 42	(32, 9) \rightarrow (34, 8)	0.8329	1.1372
42 \rightarrow 43	(32, 10) \rightarrow (34, 9)	1.8473	3.6391
49 \rightarrow 50	(36, 12, 1) \rightarrow (38, 12)	1.3753	1.5634
55 \rightarrow 56	(42, 12, 1) \rightarrow (44, 12)	0.4964	0.5150
59 \rightarrow 60	(47, 12, 1) \rightarrow (48, 12)	0.0000	0.1024

A.3. Anomalies of the third kind

Table A.3.: Table of anomalies of the 3rd kind. The 1st configuration is the ground state configuration up to the critical screening κ_{cr1} , then the ground state configuration changes in the standard way by adding a particle on a inner shell. This configuration then is the ground state up to the critical screening κ_{cr2} , at which the cluster changes its ground state configuration back to the one it had a lower screening (*anomaly of the 3rd kind*). From reference [87].

N	configuration 1	κ_{cr1}	configuration 2	κ_{cr2}	configuration 3
35	(29, 6)	3.2	(28, 7)	6.84	(29, 6)
36	(30, 6)	3.6	(29, 7)	8.76	(30, 6)
37	(30, 7)	4.2	(29, 8)	6.91	(30, 7)
39	(31, 8)	3.6	(30, 9)	13.40	(31, 8)
54	(41, 12, 1)	1.68	(40, 13, 1)	5.04	(41, 12, 1)
		5.04	(39, 14, 1)	15.02	

B. Phase transition points of Yukawa balls

B.1. Melting temperatures I

Table B.1.: Melting temperatures T_m^{crit} as determined by the frequency of occurrence P_{conf} , specific heat C_V (3.30) and the variance of the block averaged relative distance fluctuations $\sigma_{u_{rel}}$ (3.35) for $N = 31$ particles and screenings $\kappa = 0.0, \dots, 5.0$. Additionally the potential energy barrier heights are given for comparison.

κ	ΔE_{bar}	$T_m(P_{conf})$	$T_m(C_V)$	$T_m(\sigma_{u_{rel}})$
0.0	0.003274	0.003318	0.000168	0.000159
0.1	0.003153	0.003029	0.000139	0.000150
0.2	0.003050	0.002748	0.000150	0.000121
0.3	0.002895	0.003782	0.000118	0.000114
0.4	0.002707	0.002453	0.000139	0.000107
0.5	0.002500	0.003583	0.000107	0.000108
0.6	0.002284	0.002759	0.000112	0.000100
0.7	0.002068	0.002162	0.000087	0.000080
0.8	0.001859	0.001870	0.000079	0.000086
0.9	0.001659	0.001718	0.000079	0.000083
1.0	0.001471	0.001259	0.000066	0.000069
1.1	0.001389	0.001958	0.000061	0.000057
1.2	0.001134	0.001113	0.000045	0.000051
1.3	0.000980	0.001015	0.000045	0.000050
1.4	0.001163	0.001214	0.000046	0.000054
1.5	0.001036	0.001325	0.000053	0.000051
1.6	0.000916	0.001349	0.000039	0.000036
1.7	0.001727	0.001554	0.000081	0.000067
1.8	0.001672	0.002403	0.000067	0.000076
1.9	0.001623	0.001450	0.000069	0.000079

Table B.1.: Melting temperatures for $N = 31$ particles (contd.).

κ	ΔE_{bar}	$T_m(P_{conf})$	$T_m(C_v)$	$T_m(\sigma_{u_{rel}})$
2.0	0.001576	0.002068	0.000080	0.000068
2.1	0.001524	0.002436	0.000075	0.000065
2.2	0.001491	0.002084	0.000059	0.000060
2.3	0.001449	0.002013	0.000069	0.000058
2.4	0.001408	0.001783	0.000071	0.000063
2.5	0.001374	0.002118	0.000058	0.000054
2.6	0.001342	0.002000	0.000061	0.000069
2.7	0.001311	0.001370	0.000058	0.000063
2.8	0.001327	0.001576	0.000061	0.000064
2.9	0.001331	0.001788	0.000064	0.000059
3.0	0.001226	0.001473	0.000053	0.000052
3.1	0.001191	0.001523	0.000050	0.000058
3.2	0.001174	0.000993	0.000055	0.000050
3.3	0.001203	0.001096	0.000048	0.000050
3.4	0.001211	0.001582	0.000056	0.000046
3.5	0.001159	0.001833	0.000054	0.000047
3.6	0.001151	0.000969	0.000054	0.000050
3.7	0.001054	0.001525	0.000047	0.000046
3.8	0.001038	0.001632	0.000040	0.000044
3.9	0.001104	0.001534	0.000053	0.000056
4.0	0.000961	0.001082	0.000049	0.000038
4.1	0.000953	0.001110	0.000044	0.000036
4.2	0.000947	0.000882	0.000037	0.000046
4.3	0.000924	0.001344	0.000040	0.000035
4.4	0.000871	0.001339	0.000044	0.000036
4.5	0.000893	0.001018	0.000041	0.000045
4.6	0.000852	0.000896	0.000034	0.000036
4.7	0.000811	0.000792	0.000031	0.000032
4.8	0.000807	0.000902	0.000034	0.000038
4.9	0.000794	0.001197	0.000038	0.000030
5.0	0.000779	0.001062	0.000037	0.000030

B.2. Melting temperatures II

Table B.2.: Melting temperatures T_m^{crit} as determined by the frequency of occurrence P_{conf} , specific heat C_V (3.30) and the variance of the block averaged relative distance fluctuations $\sigma_{u_{rel}}$ (3.35) for $N = 11, \dots, 40$ and a set of screenings, $\kappa = 0.0, 1.0, 1.5, 4.0$. Additionally the potential energy barrier heights are given for comparison.

κ	N	ΔE_{bar}	$T_m(P_{conf})$	$T_m(C_V)$	$T_m(\sigma_{u_{rel}})$
0.0	11	0.013583	0.008658	0.002972	0.003174
	12	0.017071	0.011479	0.003141	0.003572
	13	0.012772	0.008372	0.002524	0.002008
	14	0.011797	0.008260	0.002104	0.001929
	15	0.013430	0.009367	0.002011	0.001841
	16	0.012753	0.008456	0.001795	0.001758
	17	0.014024	0.008953	0.001496	0.001549
	18	0.010736	0.007319	0.001083	0.001022
	19	0.008618	0.008956	0.001375	0.001360
	20	0.005047	0.005313	0.000657	0.000585
	21	0.005436	0.005223	0.000603	0.000708
	22	0.003034	0.003035	0.000348	0.000333
	23	0.004687	0.004751	0.000455	0.000480
	24	0.003921	0.004015	0.000396	0.000340
	25	0.002480	0.002548	0.000174	0.000205
	26	0.002649	0.002703	0.000191	0.000219
	27	0.003374	0.003469	0.000218	0.000245
	28	0.001757	0.001744	0.000108	0.000092
	29	0.003635	0.003684	0.000222	0.000219
	30	0.003699	0.003576	0.000173	0.000190
	31	0.003153	0.003029	0.000139	0.000159
	32	0.002211	0.002329	0.000098	0.000092
	33	0.001304	0.001282	0.000043	0.000046
	34	0.001427	0.001448	0.000054	0.000052
	35	0.001315	0.001383	0.000034	0.000043
	36	0.002722	0.002650	0.000079	0.000073
	37	0.002818	0.002746	0.000068	0.000063
	38	0.002644	0.002616	0.000057	0.000059
	39	0.001213	0.001272	0.000026	0.000026
	40	0.001041	0.000879	0.000022	0.000022

Table B.2.: Melting temperatures for $N = 11, \dots, 40$, $\kappa = 0.0, 1.0, 1.5, 4.0$ (contd.).

κ	N	ΔE_{bar}	$T_m(P_{conf})$	$T_m(C_v)$	$T_m(\sigma_{u_{rel}})$
1.0	11	0.010242	0.005808	0.002008	0.002106
	12	0.012982	0.007570	0.002289	0.002426
	13	0.013193	0.007182	0.002396	0.002163
	14	0.012165	0.006522	0.001875	0.001821
	15	0.013161	0.007459	0.002007	0.001825
	16	0.011813	0.006843	0.001369	0.001568
	17	0.011387	0.006406	0.001507	0.001392
	18	0.007815	0.004522	0.000920	0.000914
	19	0.005340	0.004320	0.000840	0.000852
	20	0.002873	0.002459	0.000358	0.000341
	21	0.002958	0.002431	0.000380	0.000396
	22	0.002038	0.001687	0.000250	0.000257
	23	0.002412	0.001944	0.000256	0.000269
	24	0.001872	0.001612	0.000180	0.000157
	25	0.009583	0.000809	0.000090	0.000079
	26	0.001847	0.001578	0.000156	0.000125
	27	0.000392	0.000337	0.000029	0.000025
	28	0.001951	0.001558	0.000113	0.000127
	29	0.001920	0.001674	0.000104	0.000096
	30	0.001660	0.001385	0.000075	0.000082
	31	0.001471	0.001259	0.000066	0.000069
	32	0.000346	0.000295	0.000014	0.000014
	33	0.001703	0.001468	0.000062	0.000056
	34	0.001433	0.001155	0.000052	0.000054
	35	0.001856	0.001542	0.000048	0.000063
	36	0.002153	0.001818	0.000054	0.000060
	37	0.001690	0.001471	0.000044	0.000041
	38	0.001675	0.001444	0.000040	0.000038
	39	0.001705	0.001479	0.000030	0.000038
	40	0.001350	0.001124	0.000024	0.000023
1.5	11	0.008832	0.007760	0.002026	0.001718
	12	0.010323	0.008458	0.002128	0.001822
	13	0.013100	0.011533	0.002257	0.002687
	14	0.011852	0.010455	0.002157	0.001712

Table B.2.: Melting temperatures for $N = 11, \dots, 40$, $\kappa = 0.0, 1.0, 1.5, 4.0$ (contd.).

κ	N	ΔE_{bar}	$T_m(P_{conf})$	$T_m(C_v)$	$T_m(\sigma_{u_{rel}})$
	15	0.012846	0.010798	0.002070	0.001954
	16	0.010975	0.009297	0.001662	0.001408
	17	0.009772	0.008396	0.001173	0.001228
	18	0.006263	0.005449	0.000780	0.000622
	19	0.003959	0.005188	0.000610	0.000531
	20	0.001859	0.002440	0.000245	0.000277
	21	0.001959	0.002478	0.000272	0.000275
	22	0.001465	0.001861	0.000154	0.000142
	23	0.001327	0.001775	0.000147	0.000133
	24	0.001008	0.001299	0.000080	0.000083
	25	0.000873	0.001156	0.000061	0.000079
	26	0.002001	0.002503	0.000152	0.000134
	27	0.001023	0.001324	0.000066	0.000066
	28	0.001686	0.002176	0.000102	0.000109
	29	0.001240	0.001660	0.000073	0.000065
	30	0.001085	0.000273	0.000050	0.000052
	31	0.001036	0.001325	0.000053	0.000051
	32	0.000773	0.000991	0.000030	0.000027
	33	0.001572	0.001929	0.000060	0.000057
	34	0.001961	0.002610	0.000072	0.000071
	35	0.001435	0.001906	0.000040	0.000041
	36	0.001728	0.002197	0.000051	0.000044
	37	0.001044	0.001373	0.000029	0.000023
	38	0.000968	0.001195	0.000023	0.000023
39	0.001078	0.001395	0.000020	0.000020	
40	0.001222	0.001526	0.000019	0.000021	
4.0	11	0.006676	0.005145	0.001518	0.001281
	12	0.000112	0.000084	0.000022	0.000023
	13	0.009452	0.007113	0.001959	0.001623
	14	0.011175	0.008965	0.001803	0.002059
	15	0.010820	0.008592	0.001824	0.001475
	16	0.007797	0.006071	0.001028	0.001193
	17	0.005573	0.004469	0.000767	0.000625
	18	0.003178	0.002470	0.000337	0.000316

Table B.2.: Melting temperatures for $N = 11, \dots, 40$, $\kappa = 0.0, 1.0, 1.5, 4.0$ (contd.).

κ	N	ΔE_{bar}	$T_m(P_{conf})$	$T_m(C_v)$	$T_m(\sigma_{u_{rel}})$
	19	0.001447	0.001694	0.000200	0.000217
	20	0.001202	0.001359	0.000175	0.000179
	21	0.001372	0.001611	0.000161	0.000187
	22	0.001138	0.001278	0.000118	0.000144
	23	0.002392	0.002661	0.000214	0.000228
	24	0.001450	0.001719	0.000142	0.000148
	25	0.002054	0.002418	0.000172	0.000169
	26	0.001546	0.001750	0.000100	0.000104
	27	0.000763	0.000880	0.000053	0.000052
	28	0.001160	0.001368	0.000074	0.000076
	29	0.001143	0.001338	0.000067	0.000060
	30	0.001427	0.001600	0.000067	0.000077
	31	0.000961	0.001082	0.000049	0.000038
	32	0.001362	0.001507	0.000060	0.000061
	33	0.001936	0.002236	0.000080	0.000075
	34	0.000933	0.001085	0.000032	0.000028
	35	0.000712	0.000801	0.000018	0.000020
	36	0.000918	0.000108	0.000023	0.000026
	37	0.000364	0.000403	0.000009	0.000007
	38	0.000301	0.000337	0.000007	0.000007
	39	0.000379	0.000461	0.000006	0.000006
	40	0.000491	0.000599	0.000008	0.000008

C. Ground states of Yukawa tubes

C.1. Structural transitions

Table C.1.: Critical length densities $\rho_{L,crit.}$ for structural transitions of the ground state configuration for a fixed screening parameter. The given configuration is the ground state up to the given critical length density. The x° in the rotation angle denotes an angle that could not be determined exactly. These configurations often are in the transition between two more symmetrical configurations, $[(2, 3); (1, 5)]$ in the transition between $[(1, 7); (3, 7)]$ and $[(3, 8)]$. In the other case its a transition on the inner shell from $[(1, 5); (2, 5)]$ to $[(3, 10)]$ and the inner shell does not form a regular hexagon yet.

κ	configuration	rot. angles	$\rho_{L,crit.}$
0.0	[(2)]	[(90°)]	2.15
	[(3)]	[(60°)]	3.05
	[(4)]	[(45°)]	3.45
	[(5)]	[(0°)]	3.55
	[(1); (5)]	[(0°); (36°)]	4.05
	[(1); (6)]	[(0°); (30°)]	4.55
	[(1, 5)]	[(0°; 36°)]	4.85
	[(1, 6)]	[(0°; 30°)]	5.85
	[(2, 6)]	[(0°; 30°)]	6.75
	[(1, 7); (3, 7)]	[(0°; 0°); (0°; 0°)]	6.85
	[(2, 3); (1, 5)]	[(x° ; x°); (x° ; x°)]	8.25
	[(3, 8)]	[(60°; 22 : 5°)]	9.45
	[(3, 9)]	[(60°; 20°)]	> 10.00
0.5	[(2)]	[(90°)]	2.75
	[(3)]	[(60°)]	3.05
	[(4)]	[(45°)]	3.55
	[(5)]	[(0°)]	3.85
	[(1); (5)]	[(0°); (36°)]	4.85
	[(1); (6)]	[(0°); (30°)]	5.45
	[(1, 6)]	[(0°; 30°)]	6.15

Table C.1.: Critical length densities of Yukawa tubes (contd.).

κ	configuration	rot. angles	$\rho_{L,crit.}$
	[(1); (1, 7)]	[(0°); (0°; 26°)]	6.55
	[(2, 8)]	[(0°; 0°)]	6.95
	[(2, 7)]	[(0°; 26°)]	7.65
	[(3, 8)]	[(60°; 22 : 5°)]	8.75
	[(2); (2, 8)]	[(0°); (0°; 22 : 5°)]	9.25
	[(2, 8)]	[(0°; 0°)]	9.55
	[(2, 9)]	[(90°; 20°)]	> 10.00
1.0	[(2)]	[(90°)]	3.45
	[(3)]	[(60°)]	3.55
	[(5)]	[(45°)]	4.15
	[(6)]	[(30°)]	4.25
	[(1); (5)]	[(0°); (36°)]	5.55
	[(1); (6)]	[(0°); (30°)]	5.85
	[(1, 6)]	[(0°; 30°)]	6.25
	[(1); (1, 7)]	[(0°); (0°; 26°)]	7.55
	[(2, 7)]	[(0°; 26°)]	8.35
	[(1, 5); (2, 5)]	[(x° ; 9°); (x° ; 9°)]	> 10.00
1.5	[(2)]	[(90°)]	3.45
	[(3)]	[(60°)]	3.55
	[(5)]	[(45°)]	4.15
	[(6)]	[(30°)]	4.45
	[(1); (5)]	[(0°); (36°)]	5.75
	[(1); (6)]	[(0°); (30°)]	6.55
	[(1); (1, 7)]	[(0°); (0°; 26°)]	6.75
	[(1); (6)]	[(0°); (30°)]	7.35
	[(1); (1, 7)]	[(0°); (0°; 26°)]	8.25
	[(1, 5); (2, 5)]	[(x° ; 9°); (x° ; 9°)]	> 10.00
2.0	[(2)]	[(90°)]	3.55
	[(5)]	[(60°)]	4.05
	[(6)]	[(30°)]	4.65
	[(1); (5)]	[(0°); (36°)]	6.55
	[(1); (6)]	[(0°); (30°)]	7.75
	[(1); (1, 7)]	[(0°); (0°; 26°)]	8.15
	[(1); (6)]	[(0°; 30°)]	8.35
	[(1); (1, 7)]	[(0°); (0°; 26°)]	8.75

Table C.1.: Critical length densities of Yukawa tubes (contd.).

κ	configuration	rot. angles	$\rho_{L,crit.}$
	[(2, 6)]	[(90°; 30°)]	9.15
	[(2, 7)]	[(0°; 26°)]	9.45
	[(1, 5); (2, 5)]	[(x° ; 9°); (x° ; 9°)]	> 10.00

Contributions

Reviewed papers

1. H Baumgartner, D Block and M. Bonitz, 2009, “Structure and Phase Transitions of Yukawa Balls”, accepted for publication in *Contrib. Plasma Phys.*
2. D Block, S Käding, A Melzer, A Piel, H Baumgartner and M Bonitz, 2008, “Experiments on metastable states of three-dimensional trapped particle clusters”, *Physics of Plasmas* **15**, 040701
3. M Bonitz, P Ludwig, H Baumgartner, C Henning, A Filinov, D Block, O Arp, A Piel, S Käding, Y Ivanov, A Melzer, H Fehske and V Filinov, 2008, “Classical and quantum Coulomb crystals”, *Physics of Plasmas* **15**, 055704
4. J Böning, A Filinov, P Ludwig, H Baumgartner, M Bonitz and Yu E Lozovik, 2008, “Melting of trapped few particle systems”, *Physical Review Letters* **100**, 113401
5. H Kählert, P Ludwig, H Baumgartner, M Bonitz, D Block, S Käding, A Melzer and A Piel, 2008, “Probability of metastable configurations in spherical three-dimensional Yukawa crystals”, *Phys. Rev. E* **78**, 036408
6. H Baumgartner, D Asmus, V Golubnychiy, P Ludwig, H Kählert and M Bonitz, 2008, “Structural transitions of finite spherical Yukawa crystals”, *New Journal of Physics* **10**, 093019
7. A Piel, O Arp, D Block, I Pilch, T Trottenberg, S Käding, A Melzer, H Baumgartner, C Henning and M Bonitz, 2008, “Complex plasmas: Forces and dynamical behaviour”, *Plasma Phys. Control. Fusion* **50**, 124003
8. D Block, M Kroll, O Arp, A Piel, S Käding, Y Ivanov, A Melzer, C Henning, H Baumgartner and M Bonitz, 2008, “Structure and dynamics of finite dust clouds”, *AIP Conference Proceedings* **1041**, 69-72

9. H Baumgartner, H Kählert, V Golubnychiy, C Henning, S Käding, A Melzer and M Bonitz, 2007, “Shell structure of Yukawa balls”, *Contrib. Plasma Phys.* **47**, 281-290
10. D Block, M Kroll, O Arp, A Piel, S Käding, Y Ivanov, A Melzer, C Henning, H Baumgartner, P Ludwig and M Bonitz, 2007, “Structural and dynamical properties of Yukawa balls”, *Plasma Physics and Controlled Fusion* **49**, B109-B116
11. M Bonitz, D Block, O Arp, V Golubnychiy, H Baumgartner, P Ludwig, A Piel and A Filinov, 2006, “Structural properties of screened Coulomb balls”, *Physical Review Letters* **96**, 075001
12. V Golubnychiy, H Baumgartner, M Bonitz, A Filinov and H Fehske, 2006, “Screened Coulomb balls - structural properties and melting behavior”, *J. Phys. A: Math. Gen.* **39**, 4527
13. C Henning, H Baumgartner, A Piel, P Ludwig, V Golubnychiy, M Bonitz and D Block, 2006, “Ground state of a confined Yukawa plasma”, *Phys. Rev. E* **74**, 056403

Books

1. M Bonitz, V S Filinov, A Filinov, V Golubnychiy, P Ludwig, H Baumgartner, P Levashov, V E Fortov and H Fehske, 2006, “Structure Formation in Strongly Correlated Coulomb Systems”, in: “Irreversible Prozesse und Selbstorganisation”, T Pöschel, H Malchow, L Schimansky-Geier (eds.), Logos-Verlag Berlin, pp. 143-158

Selected conference contributions

1. H Baumgartner, “Monte Carlo Simulation of Yukawa balls”, Lecture at Summer Institute “Complex Plasmas”, Hoboken, NJ, July 30-August 8 2008
2. H Baumgartner, V Golubnychiy, A Melzer, S Käding and M Bonitz, “Phase transitions in mesoscopic dust clusters”, Talk at DPG spring meeting, Düsseldorf, March 19-23 2007, *Verhandl. DPG*, P15.3
3. H Baumgartner, A Filinov, V Golubnychiy and M Bonitz, “Theory of screened Coulomb balls”, Talk at DPG Spring meeting, Augsburg, March 27-30 2006, *Verhandl. DPG*, P22.4

4. H Baumgartner, A Filinov and M Bonitz, “Thermodynamic properties of screened Coulomb balls”, Poster at DPG Spring meeting, Augsburg, March 27-30 2006, Verhandl. DPG, P28.21
Poster won the DPG award for the best theory poster
5. H Baumgartner, A Filinov and M Bonitz, “Thermodynamic properties of screened Coulomb balls”, Talk at Workshop “Diagnostics and Simulation of Dusty Plasmas”, Kiel, September 13-15 2006, 4.4
6. H Baumgartner, S Kosse, V Golubnychiy, P Ludwig, H Baumgartner, W D Kraeft, M Bonitz and H Fehske, “Theoretical analysis of spherical 3D Coulomb and Yukawa crystals”, Talk at DPG Spring meeting, Berlin, March 4-9 2005, P 17.2

Bibliography

- [1] O Havnes, T Aslaksen, and A Brattli, 2001, *Physica Scripta* **T89**, 133 3
- [2] F H Shu, F C Adams, and S Lizano, 1987, *Ann. Rev. Astron. and Astrophys.* **25**, 23 3
- [3] Y C Pei, 1992, *Astrophysical Journal* **395**, 130 3
- [4] J P Bradley, 1994, *Science* **265**, 925 3
- [5] C K Goertz, 1989, *Rev. Geophys.* **27**, 271 4
- [6] T G Northrop, 1992, *Physica Scripta* **45**, 475 4
- [7] G S Selwyn, J Singh, and R S Bennett, 1989, *J. Vac. Sci. Technol. A* **7**, 275827 4
- [8] G S Selwyn, J S McKillop, K Haller, and J Wu, 1990, *J. Vac. Sci. Technol. A* **8**, 1726 4
- [9] A Bouchoule, A Plain, L Boufendi, J P Blondeau, and C Laure, 1991, *J. Appl. Phys.* **70**, 1991 4
- [10] P Belenguer, J P Blondeau, L Boufendi, M Toogood, A Plain, A Bouchoule, C Laure, and J P Boeuf, 1992, *Phys. Rev. A* **46**, 7923
- [11] G Compagnini, 1994, *Applied Optics* **33**, 7377
- [12] C Hollenstein, 2000, *Plasma Phys. Control. Fusion* **42**, R93 4
- [13] P Bliokh, V Sinitsin, and V Yaroshenko, 1995, “Dusty and Self-Gravitational Plasma in Space”, Kluwer, Dordrecht 4
- [14] A Bouchoule, 1999, “Dusty Plasmas: Physics, Chemistry, and Technological Impacts in Plasma Processing”, Wiley, New York 4
- [15] F Verheest, 2000, “Waves in Dusty Space Plasmas”, Kluwer, Dordrecht 4
- [16] G E Morfill, B M Annaratone, P Bryant, A V Ivlev, H M Thomas, M Zuzic, and V E Fortov, 2002, *Plasma Phys. Control. Fusion* **44**, B263 4

- [17] E P Wigner, 1934, Phys. Rev. **46**, 1002 4
- [18] C C Grimes, and G Adams, 1979, Phys. Rev. Lett. **42**, 795 5
- [19] E Rousseau, D Ponarin, L Hristakos, O Avenel, E Varoquaux, and Y Mukharsky, 2009, Phys. Rev. B **79**, 045406 5
- [20] E Y Andrei, G Deville, D C Glattli, F I B Williams, E Paris, and B Etienne, 1988, Phys. Rev. Lett. **60**, 2765 5
- [21] A Filinov, M Bonitz and Yu E Lozovik, 2001, Phys. Rev. Lett. **86**, 3851 5
- [22] J H Chu and Lin I, 1994, Phys. Rev. Lett. **72**, 4009 5, 75, 76, 81, 97
- [23] M Bonitz, V S Filinov, V E Fortov, P R Levashov, and H Fehske, 2005, Phys. Rev. Lett. **95**, 235006 5
- [24] D J Wineland et al, 1987, Phys. Rev. Lett. **59**, 2935 5, 8
- [25] M Drewsen et al, 1998, Phys. Rev. Lett. **81**, 2878 8
- [26] M Drewsen, A Mortensen, J Lindballe, K Mølhave, N Kjærgaard, 2004, Nuclear Instruments and Methods in Physics Research A **532**, 237 5
- [27] H Ikezi, 1986, Phys. Fluids **29**, 1764–1766 5
- [28] J H Chu, J B Du, and I Li, 1994, J. Phys. D: Appl. Phys. **27**, 296–300 5
- [29] H Thomas, G E Morfill, V Demmel, J Goree, B Feuerbacher, and D Möhlmann, 1994, Phys. Rev. Lett. **73**, 652 75, 76
- [30] Y Hayashi, and K Tachibana, 1994, Jpn. J. Appl. Phys. **33**, L804–L806 5
- [31] A Piel and A Melzer, 2002, Plasma Phys. Control. Fusion **44** 5
- [32] O Arp, D Block, A Piel and A Melzer, 2004, Phys. Rev. Lett. **93**, 165004 5, 7, 8, 10, 11, 24, 25, 27, 100
- [33] J B Pieper, J Goree, and R A Quinn, 1996, Phys. Rev. E **54**, 5636
- [34] M Zuzic, A V Ivlev, J Goree, G E Morfill, H M Thomas, H Rothermel, U Konopka, R Sütterlin, and D D Goldbeck, 2000, Phys. Rev. Lett. **85**, 4064
- [35] Y Hayashi, 1999, Phys. Rev. Lett. **83**, 4764 24
- [36] T Pohl, T Pattard, and J M Rost, 2004, Phys. Rev. Lett. **92**, 155003 5
- [37] T Killian, 2004, Nature **429**, 815 5

- [38] B M Annaratone, T Antonova, D D Goldbeck, H M Thomas, and G E Morfill, 2004, *Plasma Phys. Controlled Fusion* **46**, B495 7
- [39] E Thomas, J D Williams, and J Silver, 2004, *Phys. Plasmas* **11**, 37 7
- [40] S Käding, and A Melzer, 2006, *Phys. Plasmas* **13**, 090701 7
- [41] M Kroll, S Harms, D Block, and A Piel, 2008, *Phys. Plasmas* **15**, 063703 7, 49
- [42] D Block and A Melzer, 2009, “Imaging diagnostics in dusty plasmas” in “Introduction to Complex Plasmas”, ed. by M Bonitz, N Horing, J Meichsner, and P Ludwig, Springer, Berlin, Heidelberg 2009. 7
- [43] A P Nefedov, G E Morfill, V E Fortov, H M Thomas, H Rothermel, T Hagl, A V Ivlev, M Zuzic, B A Klumov, A M Lipaev, V I Molotkov, O F Petrov, Y P Gidzenko, S K Krikalev, W Shepherd, A I Ivanov, M Roth, H Binnenbruck, J A Goree, and Y P Semenov, 2003, *New J. Phys.* **5**, 33 7
- [44] B M Annaratone, M Glier, T Stuffer, M Raif, H M Thomas, and G E Morfill, 2003, *New J. Phys.* **5**, 92 7
- [45] P Bryant, 2004, *New J. Phys.* **6**, 1 7
- [46] A V Ivlev, H M Thomas, G E Morfill, V Molotkov, A M Lipaev, V E Fortov, T Hagl, H Rothermel, and S Krikalev, 2006, *New J. Phys.* **8**, 25 7
- [47] V E Fortov, O S Vaulina, O F Petrov, V I Molotkov, A M Lipaev, G E Morfill, H Thomas, S A Khrapak, Y P Semenov, and A I Ivanov, 2004, *Plasma Phys. Control. Fusion* **46**, 359 7
- [48] V E Fortov, O S Vaulina, O F Petrov, V I Molotkov, A M Lipaev, V M Torchinsky, H M Thomas, G E Morfill, S A Khrapak, Y P Semenov, A I Ivanov, S K Krikalev, A Y Kalery, S V Zaletin, and Y P Gidzenko, 2003, *Phys. Rev. Lett.* **90**, 245005 7
- [49] S A Khrapak, D Samsonov, G E Morfill, H Thomas, V Yaroshenko, H Rothermel, V Fortov, A Nefedov, V Molotkov, O Petrov, A Lipaev, A Ivanov, and Yu M Baturin, 2003, *Phys. Plasmas* **10**, 1 7
- [50] A Piel, M Klindworth, O Arp, A Melzer, and M Wolter, 2006, *Phys. Rev. Lett.* **97**, 205009.
- [51] D Samsonov, G E Morfill, H Thomas, T Hagl, and H Rothermel, 2003, *Phys. Rev. E* **67**, 036404.

- [52] V V Yaroshenko, B M Annaratone, S A Khrapak, H M Thomas, G E Morfill, V E Fortov, A M Lipaev, V I Molotkov, O F Petrov, A I Ivanov, and M V Turin, 2004, *Phys. Rev. E* **69**, 066401. 7
- [53] G E Morfill, H M Thomas, U Konopka, H Rothermel, M Zuzic, A Ivlev, and J Goree, 1999, *Phys. Rev. Lett.* **83**, 1598 7
- [54] H Rothermel, T Hagl, G E Morfill, M H Thoma, and H M Thomas, 2002, *Phys. Rev. Lett.* **89**, 175001 8, 10
- [55] P S Epstein, 1924, *Phys. Rev.* **23**, 710 9, 10
- [56] B Liu, J Goree, V Nosenko, and L Boufendi, 2003, *Phys. Plasmas* **10**, 9 10
- [57] O Arp, D Block, M Klindworth and A Piel, 2005, *Phys. of Plasmas* **12**, 122102 9, 10, 11, 21, 46
- [58] J P Boeuf and L C Pitchford, 1995, *Phys. Rev. E* **51**, 1376 10
- [59] J P Boeuf, Ph Belenguer, and T Hbid, 1994, *Plasma Sources Sci. Technol.* **3**, 407 10
- [60] J E Allen, 1992, *Physica Scripta* **45**, 497 10
- [61] O Havnes, G E Morfill, and C K Goertz, 1984, *J. Geophys. Res.* **89**, 10999 10
- [62] S A Khrapak, A V Ivlev, G E Morfill, and H M Thomas, 2002, *Phys. Rev. E* **66**, 046414 10
- [63] H Totsuji, T Ogawa, C Totsuji, and K Tsuruta, 2005, *Phys. Rev. E* **72**, 036406 11, 33, 48, 49
- [64] H Totsuji, C Totsuji, T Ogawa, and K Tsuruta, 2005, *Phys. Rev. E* **71**, 045401 11
- [65] W Paul, 1990, *Rev. Mod. Phys.* **62**, 531 11
- [66] A Melzer, S Käding, D Block, and A Piel, 2008, *Photonik International* **2**, 56 11
- [67] J A Barker, R A Fisher, R O Watts, 1971, *Molecular Physics* **21**, 657 13
- [68] P A Lebowitz, G Lasher, 1972, *Phys. Rev. A* **6**, 426 13
- [69] M Falcioni, and M W Deem, 1999, *J. Chem. Phys.* **110**, 1754 13

- [70] N Metropolis, and S Ulam, 1949, *Journal of the American Statistical Association* **44**, 335–13
- [71] D Hubbard, 2007, “How to Measure Anything: Finding the Value of Intangibles in Business”, pg. 46, John Wiley & Sons 13
- [72] A V Filinov, and M. Bonitz, 2006, “Classical and Quantum Monte Carlo”, Chapter in “Introduction to Computational Methods in Many-Body Physics”, Rinton Press, Princeton 14, 15, 17
- [73] K Binder, and D W Heermann, 2002, “Monte Carlo simulation in statistical physics: an introduction”, Springer 17
- [74] W R Gilks, and D J Spiegelhalter, 1996, “Markov chain Monte Carlo in practice”, CRC Press 14, 15
- [75] W Feller, 1953, “An Introduction to Probability Theory and its Applications”, pg. 324, Wiley, New York 15
- [76] N Metropolis, A W Rosenbluth, M N Rosenbluth, A H Teller, and E Teller, 1953, *J. Chem. Phys.* **21**, 1087–15, 79
- [77] M Matsumoto, and T Nishimura, 1998, *ACM Trans. on Modeling and Computer Simulations* **8**, 3–17
- [78] V Golubnychiy, H Baumgartner, M Bonitz, A Filinov and H Fehske, 2006, *J. Phys. A: Math. Gen.* **39**, 4527–21, 59
- [79] O Arp, D Block, M Bonitz, H Fehske, V Golubnychiy, S Kosse, P Ludwig, A Melzer and A Piel, 2005, *Journal of Physics: Conference Series* **11**, 234–247
- [80] M Bonitz, D Block, O Arp, V Golubnychiy, H Baumgartner, P Ludwig, A Piel and A Filinov, 2006, *Phys. Rev. Lett.* **96**, 075001–23, 25, 27, 30, 31, 55, 56
- [81] R W Hasse and V V Avilov, 1991, *Phys. Rev. A* **44**, 4506–25, 26, 47
- [82] P Ludwig, S Kosse and M Bonitz, 2005, *Phys. Rev. E* **71**, 046403–26, 37, 59
- [83] H Baumgartner, H Kählert, V Golubnychiy, C Henning, S Käding, A Melzer and M Bonitz, 2007, *Contrib. Plasma Phys.* **47**, 281–27, 28, 29, 35, 42, 48

- [84] H Kählert, P Ludwig, H Baumgartner, M Bonitz, D Block, S Käding, A Melzer, and A Piel, 2008, Phys. Rev. E **78**, 036408 27, 59, 72, 73
- [85] H Baumgartner, 2006, Diplomarbeit “Monte Carlo Simulation von Coulomb balls”, Christian Albrechts Universität zu Kiel 23, 29, 56
- [86] S Hamaguchi, R T Farouki and D H E Dubin, 1997, Phys. Rev. E **56**, 4671 33, 55, 67
- [87] H Baumgartner, D Asmus, V Golubnychiy, P Ludwig, H Kählert, and M Bonitz, 2008, New J. Phys. **10**, 093019 34, 36, 38, 39, 40, 43, 44, I, III, IV
- [88] J Cioslowski and M Buchowiecki, 2008, Chem. Phys. Lett. **456**, 146-149 33, 47
- [89] T Kamimura, Y Suga and O Ishihara, 2007, Physics of Plasmas **14**, 123706 37
- [90] S W S Apolinario, 2008, PhD thesis “Structural and dynamical properties of finite size two- and three dimensional Wigner crystals”, University Antwerp 42, 99
- [91] F Aurenhammer, and R Klein, 2000, “Voronoi Diagrams” in “Handbook of Computational Geometry”, Amsterdam, Netherlands, pp. 201-290 44, 59, 64
- [92] S G Psakhie, K P Zolnikov, L F Skorentsev, D S Kryzhevich, and A V Abdrashitov, 2008, Phys. Plasmas **15**, 053701 46
- [93] K Matyash, H Baumgartner, G Schubert, R Schneider, A Filinov, A Melzer, H Fehske, M Bonitz, 2007, Poster P5.043 at EPS Conference Warsaw, http://epsppd.epfl.ch/Warsaw/pdf/P5_043.pdf 46
- [94] M Lampe, G Joyce, G Ganguli and V Gavrishchaka, 2000, Phys. Plasmas **7**, 10 46
- [95] P Ludwig, G Joyce, M Lampe, and M Bonitz, 2009, Poster P 11.11 at DPG spring meeting, Greifswald 46
- [96] T Antonova, B M Annaratone, D D Goldbeck, V Yaroshenko, H M Thomas, and G E Morfill, 2006, Phys. Rev. Lett. **96**, 115001 47
- [97] K Tsuruta, and S Ichimaru, 1993, Phys. Rev. A **48**, 1339 48
- [98] W D Kraeft and M Bonitz, 2006, J. Phys.: Conf. Ser. **35**, 94

- [99] W D Kraeft and M Bonitz, 2006, J. Phys.: Conf. Ser. **35**, 78 48
- [100] C Henning, H Baumgartner, A Piel, P Ludwig, V Golubnychiy, M Bonitz and D Block, 2006, Phys. Rev. E **74**, 056403 48, 49
- [101] J Cioslowski, 2008, Phys. Rev. E **78**, 026416 48
- [102] J Cioslowski, 2008, J. Chem. Phys. **128**, 164713 48
- [103] C Henning, P Ludwig, A Filinov, A Piel and M Bonitz, 2007, Phys. Rev. E **76**, 036404 48, 49
- [104] H Totsuji, C Totsuji and K Tsuruta, 2001, Phys. Rev. E **64**, 066402 49
- [105] J Wrighton, J W Dufty, C Henning, and M Bonitz, 2009, J. Phys. A **42**, 214052 49
- [106] C Henning, 2009, Dissertation “Ground State and Excitation Properties of Yukawa Balls”, Christian Albrechts Universität zu Kiel 49
- [107] C Henning, and M Bonitz, 2009, “Theory of strongly correlated dusty plasmas” in “Introduction to Complex Plasmas”, , Springer, Berlin 49
- [108] D H E Dubin, and T M O’Neill, 1999, Rev. Mod. Phys. **71**, 87 55
- [109] D H E Dubin, 1990, Phys. Rev. A **42**, 4972 55
- [110] R T Farouki, S Hamaguchi, 1993, Phys. Rev. E **47**, 1063 55
- [111] M Bonitz, P Ludwig, H Baumgartner, C Henning, A Filinov, D Block, O Arp, A Piel, S Käding, Y Ivanov, A Melzer, H Fehske and V Filinov, 2008, Physics of Plasmas **15**, 055704 55
- [112] O Vaulina, S Khrapak, and G Morfill, 2002, Phys. Rev. E **66**, 016404 55, 63, 67
- [113] J P Schiffer, 2002, Phys. Rev. Lett. **88**, 205003 55, 67, 69
- [114] D D Frantz, 2001, Journal of Chem. Phys. **115**, 13 56, 64
- [115] H Ohta, and S Hamaguchi, 2000, Phys. of Plasma **7**, 4506 57
- [116] H Löwen, 1994, Phys. Rep. **237**, 249 57
- [117] T A Weber, and F H Stillinger, 1985, Phys. Rev. B **31**, 1954 57
- [118] P R Couchman, and W A Jesser, 1977, Nature **269**, 481 57

- [119] S Krishnamurty, S Chacko, D G Kanhere, G A Breaux, C M Neal, and M F Jarrold, 2006, Phys. Rev. B **73**, 45406
- [120] K Joshi, S Krishnamurty, and D G Kanhere, 2006, Phys. Rev. Lett. **96**, 135703 57
- [121] F A Lindemann, 1910, Phys. Zeitschrift **11**, 909 57
- [122] T Ogawa, H Totsuji, C Totsuji, and K Tsuruta, 2006, Journal of the Physical Society of Japan **75**, 123501 58, 67
- [123] S W S Apolinario, B Partoens and F M Peeters, 2007, New Journal of Phys. **9**, 283 58
- [124] O S Vaulina, I E Drangevski, X G Adamovich, O F Petrov, and V E Fortov, 2006, Phys. Rev. Lett. **97**, 195001 58
- [125] K Qiao, M Benesh, T W Hyde, 2009, <http://arxiv.org/abs/astro-ph/0612286> 59
- [126] J J Gilvarry, 1956, Phys. Rev. **102**, 308 63
- [127] R D Etters, and J Kaelberer, 1975, Phys. Rev. A **11**, 1068 63
- [128] R D Etters, and J Kaelberer, 1977, The Journal of Chemical Physics **66**, 5112
- [129] J B Kaelberer and R D Etters, 1977, The Journal of Chemical Physics **66**, 3233 63
- [130] R S Berry, T L Beck, H L Davis, and J Jellinek, 1988, “Evolution of Size Effects in Chemical Dynamics, Part 2”, Advances in Chemical Physics **70**, Wiley, 75 64
- [131] S W S Apolinario, and F M Peeters, 2007, Phys. Rev. E **76**, 031107 63, 64, 67
- [132] V M Bedanov, F M Peeters, 1994, Phys Rev B **49**, 2667 64
- [133] H L Davis, J Jellinek, and R S Berry, 1987, J. Chem. Phys. **86**, 6456 64
- [134] D D Frantz, 1995, J. Chem. Phys. **102**, 3747
- [135] F Calvo, and F Spiegelmann, 2000, J. Chem. Phys. **112**, 2888 64
- [136] J Böning, A Filinov, P Ludwig, H Baumgartner, M Bonitz and Yu E Lozovik, 2008, Phys. Rev. Lett. **100**, 113401 65

- [137] D Block, S Käding, A Melzer, A Piel, H Baumgartner and M Bonitz, 2008, *Physics of Plasmas* **15**, 040701 70, 71, 72
- [138] S Käding, D Block, A Melzer, A Piel, H Kählert, P Ludwig, and M Bonitz, 2008, *Phys. Plasmas* **15**, 073710 70, 71, 72
- [139] F Baletto, and R Ferrando, 2005, *Rev. Mod. Phys.* **77**, 371 73
- [140] A Melzer, V A Schweigert, I V Schweigert, A Homann, S Peters, and A Piel, 1996, *Phys. Rev. E* **54**, R46 75, 76
- [141] D E Parry, 1975, *Surface Science* **49**, 433 75
- [142] E Madelung, 1918, *Phys. Z.* **19**, 524 75
- [143] D J Adams, and I R McDonald, 1976, *Mol. Phys.* **32**, 931
- [144] S W de Leeuw, J W Perram, and E R Smith, 1980, *Proc. R. Soc. A* **373**, 27 79
- [145] M P Allen, and D J Tildesley, 1989, “Computer Simulation of Liquids”, Oxford University Press, Oxford 75
- [146] P Ewald, 1921, *Ann. Phys., Lpz.* **64**, 253 76
- [147] C Kittel, 1986, “Introduction to Solid State Physics”, Wiley 76
- [148] T Schlick, 2002, “Molecular Modeling and Simulation - An Interdisciplinary Guide”, Springer, New York
- [149] J M Thijssen, “Computational physics”, Cambridge University Press, Cambridge 76
- [150] A Grzybowski, E Gwóźdź, and A Bródka, 2000, *Phys. Rev. B* **61**, 6706 77, 79
- [151] M Mazars, 2007, *J. Chem. Phys.* **126**, 056101 77, 79
- [152] M Porto, 2000, *J. Phys. A: Math. Gen.* **33**, 6211-6218 77
- [153] A Shukla, M Dolg, and H Stoll, 1998, *Chem. Phys. Lett.* **294**, 126 77
- [154] P Minary, J A Morrone, D A Yarne, M E Tuckerman, and G J Martyna, 2004, *J. Chem. Phys.* **121**, 11949
- [155] L Shulenburger, M Casula, G Senatore, R M Martin, 2008, *Phys. Rev. B* **78**, 165303 77

- [156] I N Bronstein, K A Semendjajew, G Musiol, and H Mühlig, 1999, “Taschenbuch der Mathematik”, Verlag Harri Deutsch 79
- [157] Y Rosenfeld, 1996, *Mol. Phys.* **88**, 1357-79
- [158] G Salin, and J-M Caillol, 2000, *J. Chem. Phys.* **113**, 10459-79
- [159] V A Schweigert, I V Schweigert, A Melzer, A Homann, and A Piel, 1996, *Phys. Rev. E* **54**, 4155-81, 97
- [160] D H E Dubin, 1993, *Phys. Rev. Lett.* **71**, 2753-2756 85
- [161] Y Snir, and R Kamien, 2005, *Science* **307**, 1067-87
- [162] S W S Apolinario, B Partoens, and F M Peeters, 2008, *Phys. Rev. B* **77**, 035321-99
- [163] S W S Apolinario, and F M Peeters, 2008, *Phys. Rev. B* **78**, 024202-99
- [164] A J Tans, M H Devoret, H Dai, A Thess, R E Smalley, L J Geerligs, and C Dekker, 1997, *Nature* **386**, 474-100
- [165] M S Dresselhaus, G Dresselhaus, and P C Eklund, 1996, “Science of Fullerenes and Carbon Nanotubes”, Elsevier 100
- [166] B D Yao, Y F Chan, X Y Zhang, W F Zhang, Z Y Yang, and N Wang, 2003, *Appl. Phys. Lett.* **82**, 281-100

Acknowledgment

An dieser Stelle möchte ich allen danken, die mich bei der Erstellung dieser Arbeit unterstützt haben. Mein erster und ganz besonderer Dank geht an Prof. Dr. Michael Bonitz, der mir die Anfertigung dieser Dissertation in seiner Arbeitsgruppe ermöglichte und es exzellent betreute. Entscheidend für die Qualität der Arbeit waren seine konstruktive Kritik und die wertvollen Hinweise in jeder Phase der Arbeit.

Für die gute und effektive Zusammenarbeit danke ich im Besonderen meinen Arbeitskollegen, Dr. Alexei Filinov, Dr. Patrick Ludwig, Dr. Volodymyr Golubnychiy, Christian Henning und Hanno Kählert, die mir mit sachkundigen Anregungen beistanden. Nicht zuletzt möchte ich mich auch bei Jens Böning für den Beistand im akademischen Alltag bedanken. Für die Anregungen aus dem Bereich der Experimentalphysik, sowohl aus Kiel als auch aus Greifswald, und den Kooperationswillen bin ich Prof. Dr. Alexander Piel, Prof. Dr. Andre Melzer, Dr. Dietmar Block, Dr. Oliver Arp, Dr. Sebastian Käding und Mattes Kroll dankbar.

Der Deutschen Forschungsgemeinschaft schulde ich meinen Dank für die finanzielle Unterstützung im Rahmen des Sonderforschungsbereichs Transregio 24.

Die angenehme Arbeitsatmosphäre in der gesamten Arbeitsgruppe hat wesentlich zum Gelingen dieser Arbeit beigetragen. Sowohl gemeinsame Freizeitunternehmungen als auch wissenschaftliche Aktivitäten wie Konferenzen und Summer Schools haben die Motivation stets hoch gehalten.

Mein Dank geht auch an die hier nicht erwähnten Mitarbeiter und Kollegen am Institut und an der Fakultät.

An Imke Goertz geht mein herzlichster Dank für ihren liebevollen Beistand, die vielfachen Unterstützungsleistungen, insbesondere im Endspurt, wertvollen Ratschläge und ihr Korrekturlesen dieser Arbeit. Auch sei all meinen Freunden, die mich verständnisvoll in der Zeit der Anfertigung dieser Arbeit begleitet und abgelenkt haben, gedankt. Und natürlich gilt mein besonderer Dank meinen Eltern, Ilse und Rüdiger Baumgartner, die mir durch Ihre finanzielle Unterstützung erst das Studium der Physik ermöglichten.

Affidavit

Diese Dissertationsschrift wurde von mir in Form und Inhalt unter Anleitung von Prof. Dr. M. Bonitz und nur unter Zuhilfenahme der angegebenen Hilfsmittel angefertigt. Diese Arbeit hat weder in gleicher, noch in ähnlicher Form an anderer Stelle im Rahmen eines Prüfungsverfahrens vorgelegen.

Kiel, den _____

(Henning Baumgartner)

Curriculum Vitae

Personal information

Name: Henning Baumgartner
Address: Knorrstrasse 15, 24106 Kiel
Born: 03.10.1975 in Schleswig
Citizenship: German
Family status: Single



Education

2006-2009 Christian-Albrechts-University of Kiel, Institute of Theoretical Physics and Astrophysics, PhD student
1998-2006 Christian-Albrechts-University of Kiel, Physics, graduated with the Diploma in March 2006
1996-1998 Hamburger Sparkasse, Training as a qualified bank clerk (IHK)
1995-1996 Basic military service, Nato-headquarters LANDCENT in Heidelberg
1988-1995 Ratsgymnasium in Rotenburg(Wümme), graduated with the Allgemeine Deutsche Hochschulreife in 1995
1986-1988 Auguste-Victoria-Schule in Flensburg
1982-1986 Elementary School in Flensburg

Employment

2006-2009 Scientific coworker in the SFB TR24 “Fundamentals of Complex Plasmas”, Institute of Theoretical Physics and Astrophysics, Christian-Albrechts-University of Kiel
2002 Scientific assistant for the organization of the Astrophysics laboratory course, Institute of Theoretical Physics and Astrophysics, Christian-Albrechts-University of Kiel
2000-2001 Scientific assistant for the organization of the Physics Olympics,

Leibniz Institute for Science Education IPN, Christian-Albrechts-University of Kiel

- 2000 Coworker in the project management for the introduction of direct banking, Hamburger Sparkasse
- 1999 Coworker in the project management for the year 2000 conversion of computer programs, Hamburger Sparkasse
- 1998 Qualified bank clerk (IHK), Hamburger Sparkasse

Skills

- Programming: Fortran 77/90, Modula-2, Pascal, Basic, C, Matlab, Lab-View
- Applications: OpenOffice, MS Office, LaTeX
- Languages: German, English, French (basic), Italian (basic), Latin
- Hobbies: Skiing, Soccer, Table tennis, Politics, Reading, Physics

Kiel, June 26, 2009